

國立臺灣大學電機資訊學院電信工程學研究所



碩士論文

Graduate Institute of Communication Engineering  
College of Electrical Engineering and Computer Science

National Taiwan University

Master Thesis

基於剪切模態體聲波激發之多鐵電性天線  
之寬頻極化控制

Broadband Polarization Control of  
Bulk Acoustic Wave-Mediated Multiferroic Antenna  
Based on Thickness Shear Modes

許瑞福

Rui-Fu Xu

指導教授：陳士元 博士

Advisor: Shih-Yuan Chen, Ph.D.

中華民國 108 年 7 月

July, 2019



# 國立臺灣大學 (碩) 博士學位論文 口試委員會審定書

基於剪切模態體聲波激發之多鐵電性天線寬頻極化控制  
Broadband Polarization Control of Bulk Acoustic  
Wave-Mediated Multiferroic Antenna Based on Thickness  
Shear Modes

本論文係許瑞福君 (R05942005) 在國立臺灣大學電信工程學研究所完成之碩 (博) 士學位論文，於民國 108 年 7 月 19 日承下列考試委員審查通過及口試及格，特此證明

口試委員：

陳士元 (簽名)  
(指導教授)

許博 歐陽良是

陳念偉

所 長 謝容明 (簽名)

## 誌謝



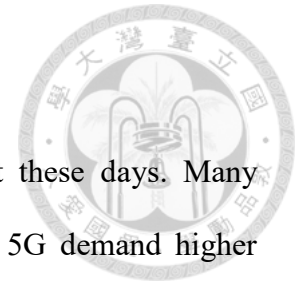
能完成這篇論文，真的非常不容易。首先我要特別感謝我的指導教授陳士元老師，以及遠在 UCLA 的 Rob Candler 老師。在偶然的機會之下，兩位教授引領我進入學術的殿堂，非常有耐心地討論並給予意見，才能讓我有機會研究最前沿的知識及題目，挑戰重大的科技問題。陳士元老師總是能給予有用且正向的回饋，激盪腦力讓我的研究得以不斷地前進，是我學術上最好的典範及學習的對象。而 Rob Candler 教授在台灣訪問的約一年間，總是不吝嗇地分享想法及提供建議，讓我有機會探索知識的邊界。我也要感謝 UCLA 的博士生 Sidhant Tiwari，在這三年間不間斷地透過電子郵件討論並交換學術意見。雖然這個題目因為非常前沿，加上橫跨許多領域，因此時常討論並無確切結論，但他還是盡力協助回答，並花了一整年的時間將我的晶片實作出來。天線實驗室的廖修平學長、Robin 學長、聖偉學長、登胤學長，也給予我在量測及模擬上許多的意見與協助，若沒有他們的協助很難完成地這麼順利。也很感謝實驗室的同學們紫瑤、奕霖、金隆，大家時常提供給我不同的想法及刺激，若這麼新的題目缺乏討論，實在是很在進行下去。也謝謝我研究所期間兩年的陸生室友王達，讓我在苦悶的論文撰寫期間多了不少樂趣。也要感謝我的父母，他們從小到大無條件愛我並讓我成長，才讓我有機會追求學術的夢想。最後我希望感謝鄭明析牧師，他透過聖經的教導讓我深刻了解基督信仰，在對信仰的追求及努力之下，也讓我決心走上追求挑戰及創新的學術之路，更有力量能堅持下去不放棄。這個題目做得人很少也很新，與此同時研究所這三年我卻同時擔任了行政院青年諮詢委員、台大研究生協會會長，每週開大大小小的會議，辦了數十場研究生的活動，也到了英特爾實習，若沒有信仰的力量我無法做到這麼多事情，擁有這麼精采的研究所生活。真心期盼未來能將學術的果實貢獻於台灣社會全體，幫助改善人類的生活，充實台灣的國家實力能更加獨立且茁壯。

## 中文摘要



近年來在 5G、物聯網、生醫電子、穿戴式裝置等應用的發展之下，天線微小化已逐漸成為越來越重要的題材。天線微小化在過往有許多的嘗試，例如：使用高磁導率或是介電係數的基材、不同的天線設計等等。但不論在低頻或高頻頻段，只要天線相對於共振波長尺寸遠小於一時，輻射效率就會變得很差而不堪使用。2015 年首次提出了利用機械聲波，採用多鐵電性材料來實現天線微小化的可能性，基本原理是機械聲波在相同的共振頻率下，波長相較電磁波小了千倍到萬倍左右，因此若能在合適的共振頻段減少耗損，將有可能實現天線微小化並逼近理論極限。然而在過往提出的設計概念中，主要是使用縱向波的共振來實現，在本研究中主要針對了這類型新的天線，首次提出了藉由平面電極來激發剪切模態的概念。因為剪切模態可以有對稱且相互垂直的兩個模態，因此若施加特定相位差將可進行極化控制。除了極化控制之外，剪切模態可激發橫向的磁流，因此若放置於金屬平面上，可期待得到更強而非相消的輻射。此類極化控制的設計概念，使用了 COMSOL 數值模擬及 MATLAB 的後處理計算來驗證。根據模擬結果在理想的九十度相位差饋入之下，此類圓極化模態擁有極寬頻的特性。相關設計由 UCLA 的 Rob Candler 教授之研究團隊製作晶片並在台大完成了量測，本論文亦將針對量測結果進行初步的探討與分析。

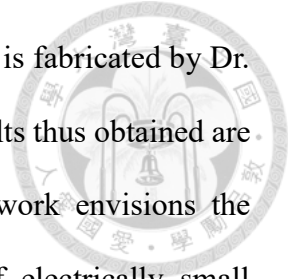
# ABSTRACT



Antenna miniaturization has been more and more important these days. Many applications like IOT, biomedical devices, wearable devices, and 5G demand higher performance with smaller feature size. Many works on antenna miniaturization have been done before, such as using substrate with high permittivity or permeability, diverse structure antenna design, etc. However, no matter in UHF or VLF band, as long as the electrical size of an antenna is much smaller than one, the radiation efficiency will be extremely low, making the antenna infeasible. In 2015, theoretical groundwork of using multiferroic material to achieve antenna miniaturization was firstly propose, named “bulk acoustic wave-mediated multiferroic antenna”. The core concept is that the wavelength of mechanical wave is five orders of magnitude smaller than electromagnetic wave under the same resonant frequency. As long as the loss can be further reduced, it owns great potential to approach Chu’s limit for electrically small antennas.

In the above mentioned works, the radiation is mainly generated based on longitudinal acoustic wave. In this thesis, thickness shear mode is used instead of longitudinal one. By using the shear mode, two sets of symmetrical but orthogonal resonant modes can be manipulate by applying  $90^\circ$  phase difference to generate circularly polarized (CP) wave. In addition, the shear wave can excite in-plane magnetic current, which will double the radiation instead of cancelling out each other when the device is placed above a metallic ground plane according to the image theory. Such concept can also be used for tunable polarization control. The design concept is preliminarily investigated through FEM-based multi-physics solver, COMSOL, and post processing by an in-house MATLAB code. It is shown that under the ideal input RF signal pair of equal magnitude and with  $90^\circ$  phase difference, the proposed design can achieve very

broadband CP with satisfactorily low in-band axial ratio. The design is fabricated by Dr. Sidhant Tiwari from UCLA. The test pieces were tested, and the results thus obtained are presented and discussed through a couple of comparisons. This work envisions the possibility of broadband polarization control and/or tunability of electrically small antennas.

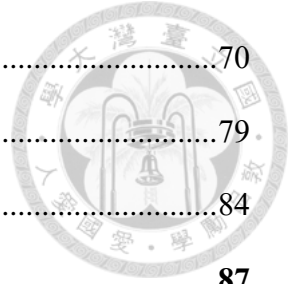


# CONTENTS



口試委員審定書 .....	ii
誌謝 .....	iii
中文摘要 .....	iv
ABSTRACT .....	v
CONTENTS .....	vii
LIST OF FIGURES .....	ix
LIST OF TABLES .....	xvi
<b>Chapter 1 Introduction.....</b>	<b>1</b>
1.1 Evolution of Mobile Standards from 1G to 5G .....	1
1.2 RF MEMS as a Potential Boosting Technology to RF System Improvement .....	8
1.3 Brief Review on Antenna Miniaturization Theory .....	14
1.4 Applications for Miniaturized Antenna .....	20
<b>Chapter 2 Background and theory .....</b>	<b>28</b>
2.1 Piezoelectric and Magnetic Material for Microwave Application.....	28
2.2 Dynamic Magnetization as a Radiation Source.....	37
2.3 Sources of Dynamic Magnetization.....	40
2.4 Device Operation Principle.....	46
<b>Chapter 3 Circularly-polarized BAW Multiferroic Antenna.....</b>	<b>49</b>
3.1 Circular Polarization Control of Bulk-Acoustic Wave Mediated Antenna Using Lateral Field Excitation.....	49
3.2 Numerical modelling .....	53
3.3 Results and Analysis .....	57
<b>Chapter 4 Measurement results.....</b>	<b>70</b>

4.1	Device fabrication and design .....	70
4.2	Setup and measurements.....	79
4.3	Results and Discussions.....	84
<b>Chapter 5</b>	<b>Conclusions.....</b>	<b>87</b>
5.1	Summary.....	87
5.2	Future Works.....	88
References	.....	89





# LIST OF FIGURES



Fig. 1.1. First portable device for mobile radio communications [1] .....1

Fig. 1.2. Trend in size reduction of mobile handsets [3]. .....2

Fig. 1.3. Flywheel effect triggering more and more data demand from the end user side [7].....4

Fig. 1.4. Comparison of maximum data rate capacity, in terms of Mbps [6].....4

Fig. 1.5. Trend in the decrease of connection quality [8]. .....6

Fig. 1.6. Performance bowl for the most significant specifications and characteristics expected from RF passives for 5G applications [9].....6

Fig. 1.7. Plot of crossed-relationships among 5G challenges, facilitators and design trends [10].....7

Fig. 1.8. Prediction of number of components per chip. Historical data from 1959 to 1965 and Moore’s extrapolation after 1965 [11]. .....8

Fig. 1.9. Photos of some MEMS inertial sensors. (a)–(e): MEMS acceleration sensors, (a) first type of integrated acceleration sensor (1-axis); (b), (c) 2-axes; and (d), (e) 3-axes sensors. (f)–(h): MEMS gyros (f), (g): 1-axis, (h): 2-axes [16]...10

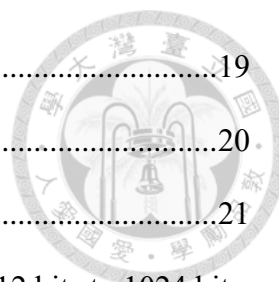
Fig. 1.10. Typical hype curve behavior elaborated by Gartner Inc. [20]. ..... 11

Fig. 1.11. Evolution of RF-MEMS market forecasts released in: (a) 2004; (b) 2006; (c) 2010; (d) 2012; (e) 2013 [21]. ..... 13

Fig. 1.12. Antenna within a sphere of radius  $r$ , and its equivalent circuit model [25]. ...14

Fig. 1.13. Measured product for 110 antenna designs published in the IEEE T-AP by the end of 2010 [26]..... 17

Fig. 1.14. ME FBAR antenna demonstrated in [36]. The longitudinal mode is excited and the radiation at 2.5GHz is detected with comparison of FeGaB to Al material.



.....19

Fig. 1.15. Technology roadmap of Internet of Things (IOT) [44].....20

Fig. 1.16. The components of a RFID system.....21

Fig. 1.17. Evolution of RFID tags compared in size to a penny from 12 bits to 1024 bits.  
The area of the circuitry of the tag has been reduced greatly except the area  
occupied by antenna [46].....22

Fig. 1.18. Implant with antenna and circuitry [47].....24

Fig. 1.19. Dual band antenna [47] .....24

Fig. 1.20. Photos of prototypes and nonwoven conductive fabrics (NWCFs) [53]. .....25

Fig. 1.21. Underground communications [34] .....26

Fig. 1.22. Underwater communications [34].....26

Fig. 1.23. Attenuation of EM wave passing through Sea Water [56] .....27

Fig. 1.24. US Navy’s VLF antenna in Cutler, Maine [34] .....27

Fig. 1.25. Spinning Magnet Array [34] .....27

Fig. 2.1. Concept illustration of a piezoelectric disk generating a voltage when deformed.  
.....28

Fig. 2.2. Comparison of a classical LC TV IF filter with an SAW TV IF filter [62] .....31

Fig. 2.3. Application space regarding frequency spectrum or RF filters [63].....32

Fig. 2.4. (a) FBAR and (b) SMR structures. [65].....33

Fig. 2.5. Example BAW filters used in iPhone 6(EPFL online course MEMSx).....33

Fig. 2.6. Photograph of a disassembled ferrite junction circulator, showing the stripline  
conductor, the ferrite disks, and the bias magnet. [69].....35

Fig. 2.7. BAW-resonance-based antenna [36]. .....36

Fig. 2.8. (a) Relationship between multiferroic and magnetoelectric materials.  
Illustrates the requirements to achieve both in a material. (b) Schematic

illustrating different types of coupling present in materials [71].	36
Fig. 2.9. Spin magnetic dipole moment and angular momentum vectors for a spinning Electron [69].	40
Fig. 2.10. Magnetic moment of a ferrimagnetic material versus bias field $H_0$ [69].	42
Fig. 2.11. Dynamic permeability in the vicinity of FMR (a) Magnitude of permeability. (b) Real and imaginary parts of the permeability [72].	44
Fig. 2.12. SAWs are generated in a piezoelectric substrate by applying an AC.	45
Fig. 2.13. (a) Plot of the absorption of SAW power by the magnetic element (in dB) as a function of applied x and y magnetic field at a SAW frequency of 1992 MHz (b) Line cut along the direction indicated by the black line in (a) at a number of different SAW frequencies (green, 857 MHz; red, 1424 MHz; and black, 1992 MHz). [74]	45
Fig. 2.14. FDTD modelling of proposed antenna structure by Zhi Yao et al. First column is the excited acoustic resonance mode. Middle column is the stress profile as a function of time. Last column is the radiated electric field [37].	46
Fig. 2.15. BAW resonance based antenna. (a) Structure and physical coupling mechanism. (b) Cross section of the antenna. Electric current excitation is applied to the electrodes to drive bottom piezoelectric layer, and the standing wave resonance further triggers the magnetostrictive layer as the equivalent magnetic current source of radiation [37].	48
Fig. 3.1. (a) Left-hand circular polarization. (b) Right-hand circular polarization. (c) Polarization ellipse [77].	51
Fig. 3.2. The sketch of the AlN-based solidly mounted resonator operated in thickness shear mode waves [79]	51
Fig. 3.3. Electric and magnetic sources and their images near electric (PEC) and	52

Fig. 3.4. The finite element simulation of the electric field generated by the simple .....	52
Fig. 3.5. Simulated structure of BAW-mediated multiferroic antenna. M represents magnetization inside magnetostrictive layer.....	53
Fig. 3.6. Two sets of lateral electrodes are placed at the bottom of BAW-mediated multiferroic antenna. Each set of electrode includes a terminal connected to ground and a terminal connected to voltage source. The spacing between two terminals of one set of electrodes is 10 ( $\mu\text{m}$ ). The thickness of electrodes is 0.1 ( $\mu\text{m}$ ). External voltage sources with 90-degree phase differences are applied upon each set of electrodes and thus creates circular polarized electric field at the bottom.....	54
Fig. 3.7. Flow chart of numerical modelling.....	57
Fig. 3.8. Snapshots of displacement animation operated at 250 MHz (length units in $\mu\text{m}$ ). (Left-top) $t = T/4$ ; (Right-top) $t = T/2$ ; (Left-bottom) $t = 3T/4$ ; (Right-bottom) $t = T$ . Counter-clockwise circular polarized (from top's view) displacement can be observed clearly.....	59
Fig. 3.9. Magnitude and phase distribution across z axis of stress tensor (a) Left: $T_{xz}$ and (b) Right: $T_{yz}$ insides the device.....	61
Fig. 3.10. (a) X-Z cut radiation pattern; (b) Y-Z cut radiation pattern. Radiation pattern of circular polarized BAW-mediated multiferroic antennas. This calculated radiation pattern is selected to be the frequency with lowest axial ratio within simulated frequency range.....	62
Fig. 3.11. Broadside axial ratio versus frequency between 100MHz and 500MHz.....	62
Fig. 3.12. Resonant mode 1 at 148MHz with axial ratio = 0.16. It is identified as weak fundamental thickness modes.....	63
Fig. 3.13. Resonant mode 1 at 148MHz with axial ratio = 0.16.....	63

Fig. 3.14. resonant mode 2 at 249MHz with axial ratio = 0.12.....	64
Fig. 3.15. Resonant mode 2 at 249MHz with axial ratio = 0.12. It is identified as main desired fundamental thickness shear modes. ....	64
Fig. 3.16. Resonant mode 3 at 387MHz with axial ratio = 8.9. ....	65
Fig. 3.17. Resonant mode 3 at 387MHz with axial ratio = 8.9. It is identified as the excitation of undesired mode.....	65
Fig. 3.18. Resonant mode 4 at 472MHz with axial ratio = 0.31. ....	66
Fig. 3.19. Resonant mode 4 at 472MHz with axial ratio = 0.31. It is identified as the second order of thickness shear mode. ....	66
Fig. 3.20. Resonant mode 5 at 476MHz with axial ratio = 10.6. ....	67
Fig. 3.21. Resonant mode 5 at 476MHz with axial ratio = 10.6. It is identified as the excitation of undesired mode.....	67
Fig. 3.22. The magnitude and phase distribution along z axis of radius of 1 $\mu\text{m}$ . The axial ratio of frequency responses is also shown.....	68
Fig. 3.23. Simulated structure of thickness of 1.1 $\mu\text{m}$ and radius of 1 $\mu\text{m}$ . ....	68
Fig. 3.24. The magnitude and phase distribution along z axis of radius of 10 $\mu\text{m}$ . The axial ratio of frequency responses is also shown.....	69
Fig. 3.25. Simulated structure of thickness of 1.1 $\mu\text{m}$ and radius of 10 $\mu\text{m}$ . ....	69
Fig. 4.1. Fabrication process of BAW antenna [72]. ....	70
Fig. 4.2. Layout of 200 $\mu\text{m}$ CP BAW antenna. The green pads represent electrodes. The blue lines represent electric trace to provide shear excitation. The red disk represents the fabricated BAW antenna. ....	72
Fig. 4.3. Layout of 500 $\mu\text{m}$ CP BAW antenna. The green pads represent electrodes. The blue lines represent electric trace to provide shear excitation. The red disk represents the fabricated BAW antenna. ....	73

Fig. 4.4. Layout of 1000 $\mu\text{m}$ CP BAW antenna. The green pads represent electrodes. The blue lines represent electric trace to provide shear excitation. The red disk represents the fabricated BAW antenna.....	73
Fig. 4.5. Four ports CPW-Slot-CPW wideband branch-line coupler .....	74
Fig. 4.6. Simulated S parameters of four ports CPW-Slot-CPW wideband branch-line coupler connected with SMA connectors. ....	75
Fig. 4.7. Photo of the finished four ports wideband CPW-Slot-CPW branch-line coupler.....	75
Fig. 4.8. Finished CP BAW antenna soldered onto branch-line coupler. ....	76
Fig. 4.9. Feeding BAW antenna and connecting with later electrodes with port 2 and 3	76
Fig. 4.10. Photo of the fabricated BAW antenna of 500 $\mu\text{m}$ . ....	77
Fig. 4.11. Photo of the fabricated BAW antenna of 1000 $\mu\text{m}$ one under optical microscope. The bond wires are used to connect with CPW signal and ground. The device is in the center of the chip.....	77
Fig. 4.12. Photo of the fabricated BAW antenna of 200 $\mu\text{m}$ . ....	78
Fig. 4.13. Block diagram of measurement setup .....	80
Fig. 4.14. Measurement setup. Network analyzer at the right position is connected to horn antenna. A tunable permanent magnet is place the bottom to provide external biased magnetic field to saturate the device. ....	80
Fig. 4.15. he adjustable permanent magnet is meant to provide necessary out-of-plane magnetic field to saturate the device. One tesla is measured near the surface of the chip using a DC magnetic meter MG-3003SD.....	81
Fig. 4.16. The photo of fabricated patch antenna. ....	81
Fig. 4.17. The measured S parameters of patch antenna. ....	82
Fig. 4.18. Microscope view of the output CPW terminated with SMD resistor 0201. ...	82

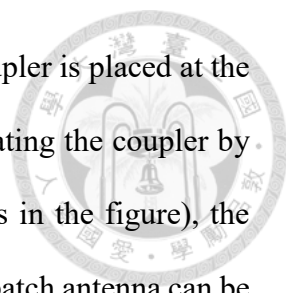


Fig. 4.19. Measuring radiation from four ports coupler itself. The coupler is placed at the same direction with the col-pol of patch antenna. By rotating the coupler by 90 degrees relative to the center of the magnet (red cross in the figure), the orthogonal component which is the same as cross-pol of patch antenna can be measured. ....83

Fig. 4.20. The measured S parameters of CP BAW antenna of Ni/NiFe with radius of 200 $\mu\text{m}$ . ....85

Fig. 4.21. The measured S parameters of patch antenna/branch-line coupler/coupler connected with load. ....85

Fig. 4.22. The measured S parameters of CP BAW antenna of Ni/NiFe with radius of 1000 $\mu\text{m}$ . ....86

Fig. 4.23. The measured S parameters of CP BAW antenna of Ni/NiFe with radius of 500 $\mu\text{m}$ . ....86

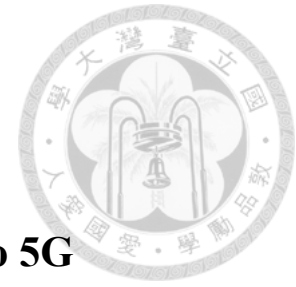
# LIST OF TABLES



Table 1. Summary of mechanical antenna transmitter experiments [33]. .....	18
Table 2. Piezoelectricity, innovation fields, and important applications [61] .....	30
Table 3. Basic parameters of COMSOL simulation .....	58
Table 4. Fabrication process of BAW antenna for each layer and action. ....	71



# Chapter 1 Introduction



## 1.1 Evolution of Mobile Standards from 1G to 5G

In 1885, the electromagnetic wave experiment conducted by German physicist Heinrich Hertz first unveiled the era of wireless communication. Since then, the demands on hardware capabilities of mobile systems have been gradually elevated. In Fig. 1.1, the first portable device for mobile radio communications (i.e., a radio signal strength testing system) in 1924 is shown. It was quite bulky and very different from the outlooks of modern handsets. It was not until 1979, the first commercial cellular network for voice transmission started, covering more than 20 million users of Tokyo. At then, so-called “mobile” handset seemed still not so “mobile”. Power consumption is extremely high. It’s even not an affordable option for a common household. In Fig. 1.2, the great advances



Fig. 1.1. First portable device for mobile radio communications [1]

of significant size reduction of mobile handset can be observed [1].

Right after the birth of wireless communication, the second mobile networks (2G) continued spreading the mobile services to larger numbers of people. Compared to 1G, 2G focused on dealing with digital signal processing. Bitrate can be reduced from 64 kb to 8 kb per second after encoding the voice signal. With the introduction of Global Systems for Mobile communications (GSM), the available channels are expanded greatly and the first non-voice data, by means of Short Message Service (SMS) and e-mail exchange was launched [2].

After many important breakthroughs accomplished, 2G was followed by 3G in 2000. After the introduction of 2G service, users are becoming more eager for broadband usage and wider coverage of mobile services. These factors drove huge increase of the demand of mobile Internet. The trends of growing needs for higher data rates is shown in Fig. 1.3. However, this means that not only RF systems and transmission data capabilities but also relative components integrated in device require a huge advancement, e.g., camera and

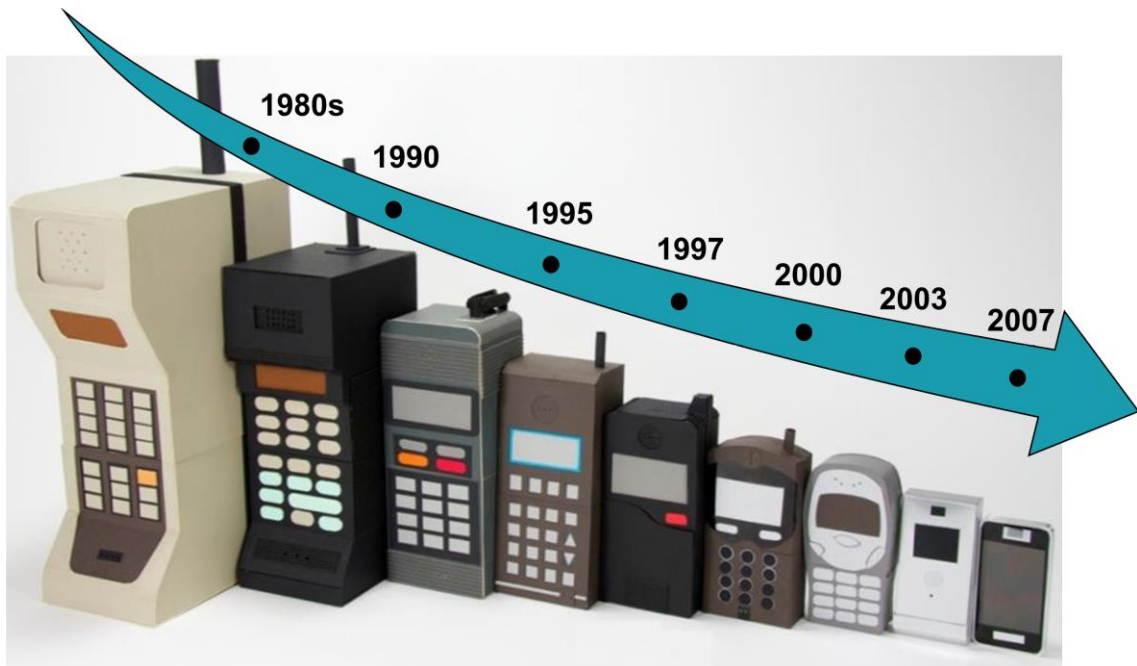


Fig. 1.2. Trend in size reduction of mobile handsets [3].

screens, etc.

4G Long Term Evolution (4G- LTE) is not an exception following the same trends of expanding system capacities **錯誤! 找不到參照來源。** . More and more services are integrated with the 4G standards, which all demand faster and more efficient data transfer. New techniques like Carrier Aggregation (CA) and Multiple Input Multiple Output (MIMO) were introduced for the sake of above-mentioned needs [4]. The relation between user demand and system performance is illustrated in Fig. 1.4.

From the above reviews, it's quite natural to think that the 5<sup>th</sup> generation (5G) aims to provide more advanced system capacities, such as higher data transfer capacity and wider coverage, etc. In addition to that, it's also expected to provide interconnected services for wireless connections. Hence the Internet of Things (IoT) paradigm is proposed, aiming to picture the futuristic digital world based on these concepts. The IoT is based on the following functionalities [5]:

- Self-awareness. Served as identification, localization and self-diagnosis of the object environment;

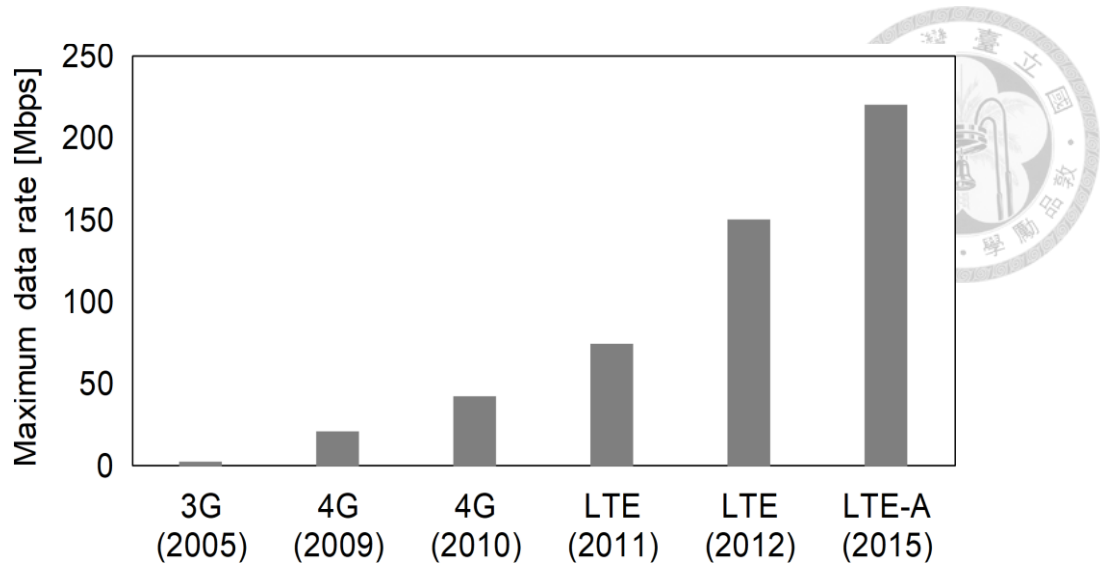


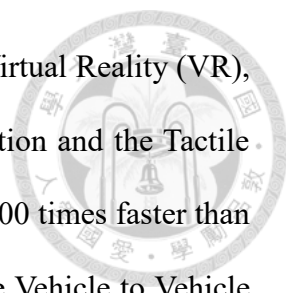
Fig. 1.4. Comparison of maximum data rate capacity, in terms of Mbps [6].



Fig. 1.3. Flywheel effect triggering more and more data demand from the end user side [7].

- Interaction with the surrounding environment. Emphasizing on data acquisition (sensing and metering) and actuation;
- Data elaboration. Interpreting or analyzing for both basic (primitive data aggregation) and advanced (statistics, forecasts).

There are several application areas mentioned frequently like Smart City/Environment, Smart Home, Smart Metering/Smart Grid, Smart Building, eHealth, Smart Logistics, Smart Factory, Smart Asset Management, Smart Agriculture, Smart Car, etc. They could also be generalized to the concept of the paradigm of the Internet of



Everything (IoE), which includes much more applications, such as Virtual Reality (VR), Augmented Reality (AR), Machine to Machine (M2M) communication and the Tactile Internet. Hence, the transmission capacity in 5G is expected to be 1000 times faster than 4G-LTE, equivalent to 10 Gbps to each user. Some applications like Vehicle to Vehicle (V2V) communications will require extra features, such as extremely low latency. These challenges are named as EMBB (Enhanced Mobile Broadband), URLLC (Ultra-Reliable Low-Latency Communications) and MMTC (Massive Machine-Type Communications) as discussed in [5].

One of the important approach is the mmWave usage. Sub-6 GHz or well above 6 GHz (up to 60–70 GHz) spectrum usage are extensively discussed, combining massive MIMO solutions and advanced beamforming capabilities. However, as mobile devices become smaller and thinner, it has been a tough and challenging task to improve overall performances simply by integrating circuitry. In [8], it is estimated that the theoretical ratio of signal quality versus actual RF signal quality was decreasing with a pace of about 1 dB per year for over a decade. This is an inevitable problems for all RF engineers since performances of RF system and the services quality provided will be greatly undermined (see Fig. 1.5). RF MEMS is anticipated to be one of the potential saviors for these imminent challenges. The commonly mentioned problems faced by 5G system implementation are listed in Fig. 1.6. Theses 5G challenges of RF systems are summarized in Fig. 1.7.

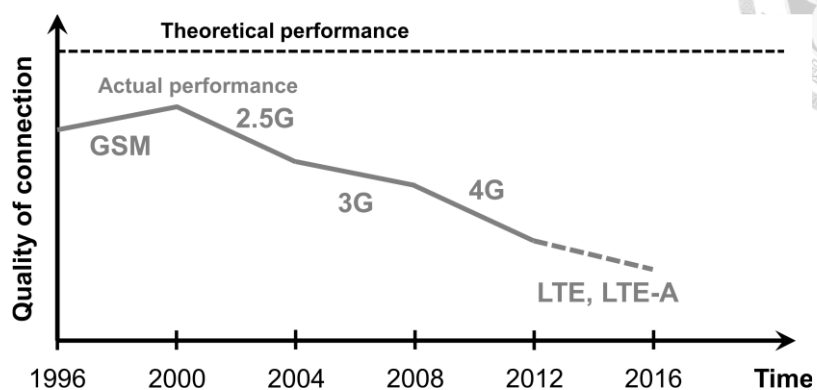


Fig. 1.5. Trend in the decrease of connection quality [8].

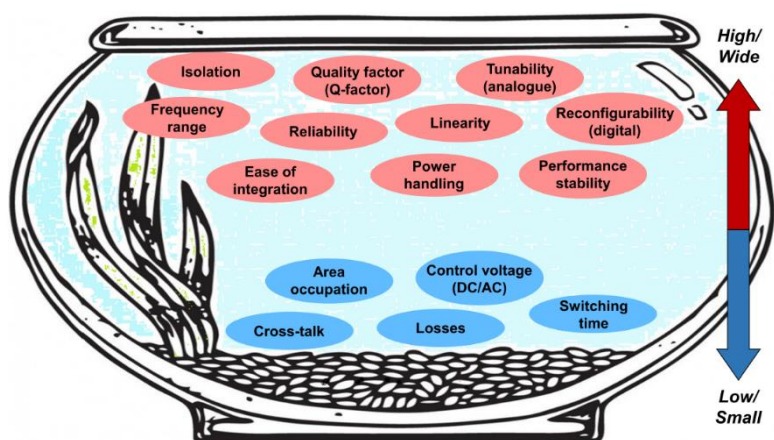


Fig. 1.6. Performance bowl for the most significant specifications and characteristics expected from RF passives for 5G applications [9].

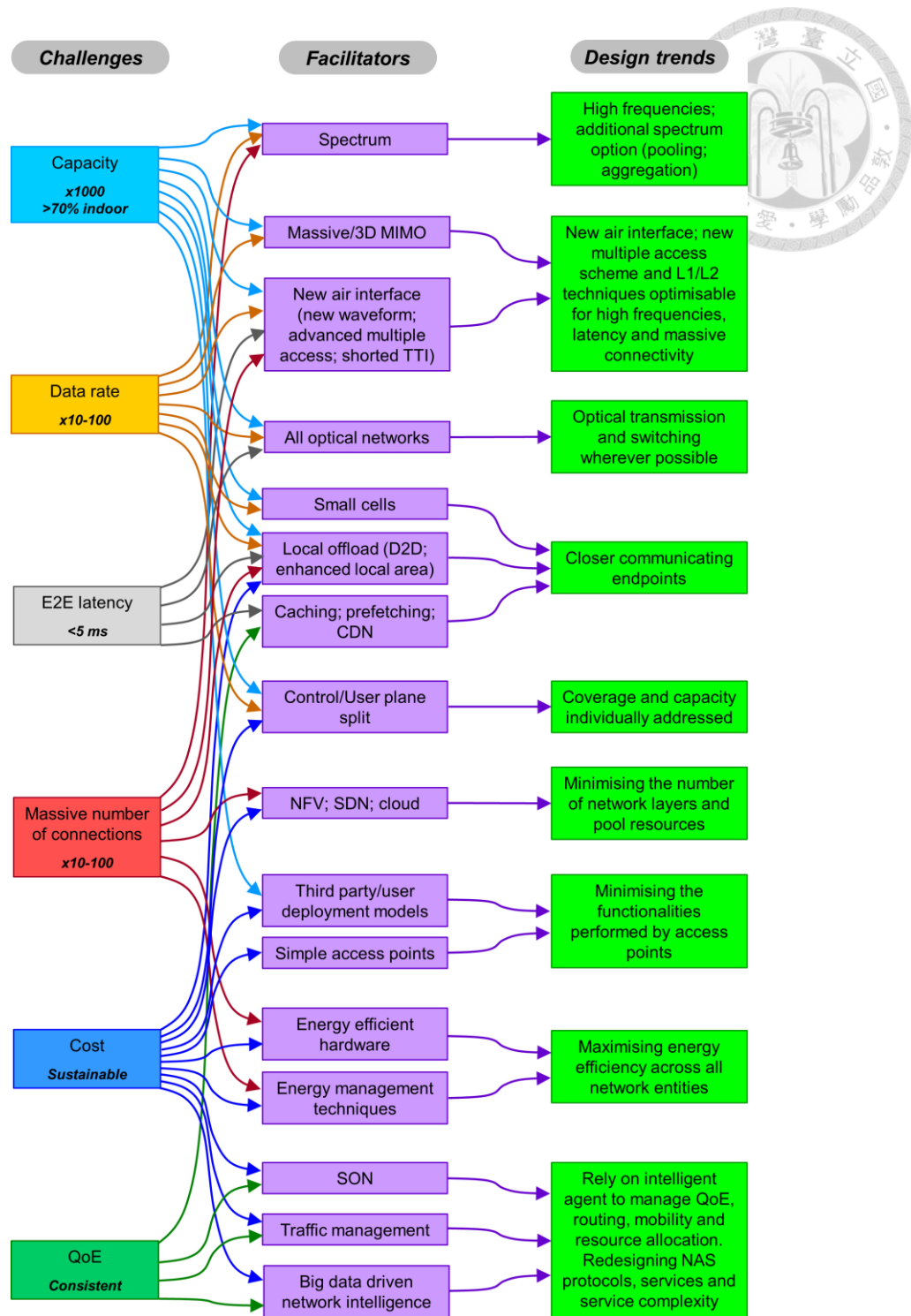
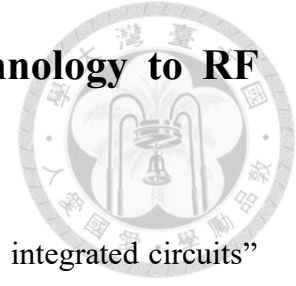


Fig. 1.7. Plot of crossed-relationships among 5G challenges, facilitators and design trends [10].

## 1.2 RF MEMS as a Potential Boosting Technology to RF System Improvement



In 1965, an article entitled “Cramming more components onto integrated circuits” marks an indelible moment in human history. It was this review that firstly investigate the progress in the semiconductor industry [11]. Moore observed that the number of components per chip was roughly doubling every year since the invention of the first commercial transistor in 1959. Based on this observation, he proposed a bold statement, predicting the exponential growth in circuit density. This trend of the growth of components per chip seems to be “a life without tradeoffs” with the benefits of continuous reduced cost per transistor [12]. With the tremendous efforts of countless engineers, these three factors of advancement completely revolutionized the whole integrated circuit (IC) industry and our daily life. For the past 40 years, the number of transistors on a semiconductor device has doubled approximately every 18–24 months. The cost reduced about 25-30% per year, giving birth to many complex, high performance, and low power products. If you spend \$1 to buy a transistor in 1965, you can almost buy 10 million

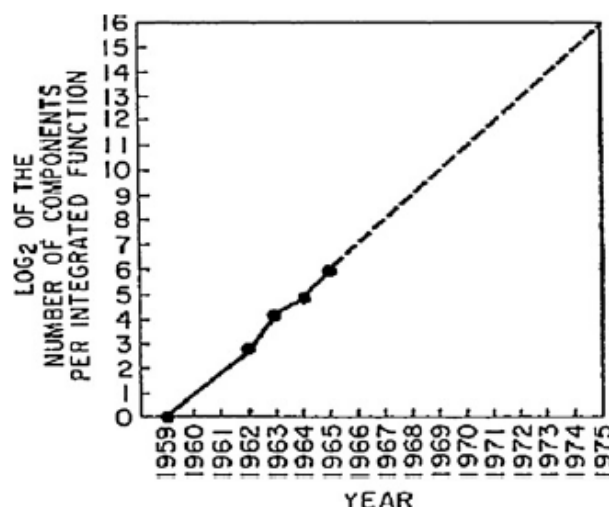


Fig. 1.8. Prediction of number of components per chip. Historical data from 1959 to 1965 and Moore’s extrapolation after 1965 [11].



transistors now [13].

With the prosperous success in IC industry, the manufacturing process continued to refine and become mature. In 1982, K. Peterson published a widely-cited paper, analyzing the potential of silicon as mechanical material [14]. There are four important traits of silicon to be used as electronic base material, which greatly facilitates commercial success: (1) low price/abundance; (2) processing based on thin deposited film amenable to miniaturization; (3) production using photographic techniques capable of high precision and amenable to miniaturization and; (4) able to be fabricated in batch [14]. As a result, silicon processing successfully finds new areas of applications and leads to various useful MEMS commercial products.

The concept of Micro-electromechanical system (MEMS) technology can be traced back to 1954 with the paper by Smith [15]. After the paper by Smith, MEMS technology has been successful used in many sensing devices, such as accelerometers, strain gauges, microphones, air mass flow sensors, pressure sensors, gyroscopes and yaw-rate sensors [15]. In Fig. 1.9, there're several typical MEMS inertial sensors listed.

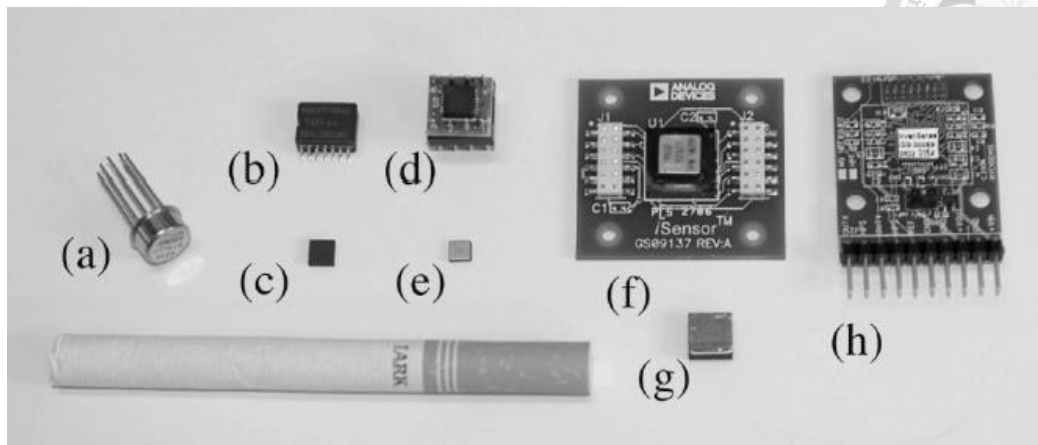


Fig. 1.9. Photos of some MEMS inertial sensors. (a)–(e): MEMS acceleration sensors, (a) first type of integrated acceleration sensor (1-axis); (b), (c) 2-axes; and (d), (e) 3-axes sensors. (f)–(h): MEMS gyros (f), (g): 1-axis, (h): 2-axes [16].

Compared to conventional MEMS products, RF passive component with MEMS technology is new. The first one came out in the early 1990 when MEMS accelerometers were valuable commercial products already. Coplanar waveguide (CPW) and microstrip implementations of transmission lines were studied first. Gradually there were more and more RF components added to the list of RF-MEMS applications. MEMS provides the potential to miniaturize RF passive components, such as switches, voltage-tunable capacitors, high-Q inductors, film bulk acoustic resonators (FBARs), dielectric resonators, transmission line resonators and filters, and mechanical resonators and filters, which mostly outperform traditional RF components if the cost is not considered [17]. Hence, it's likely for RF-MEMS to revolutionize the design of the transceiver systems and be expected to solve the serious challenges for the implementation of 5G systems.

There are quite a few components of RF-MEMS anticipated to empower the 5G potential application scenes, especially for the mmWave band listed in [18]: “(1) Very-wideband switches and switching units with low-loss (when ON), high-isolation (when

OFF) and very-low adjacent channels cross-talk, working from 2–3 GHz up to 60–70 GHz; (2) Reconfigurable filters with very good stopband rejection characteristics and extremely low attenuation of the passed band; (3) Very-wideband multi-state impedance tuners; (4) Programmable step attenuators with multiple configurations and very flat characteristics over 60–70 GHz frequency spans; (5) Very-wideband multi-state/analogue phase shifters; (6) Hybrid devices with mixed phase shifting and programmable attenuation; (7) Miniaturized antennas and arrays of antennas, integrated monolithically with one or more of the devices.”

The potential market growth is also discussed in [19]. According to the hype curve behavior proposed by Gartner Inc., the trends of new technologies, including RF-MEMS, are depicted in Fig. 1.10, and the market expectation for RF MEMS market from 2004-2013 is shown in Fig. 1.11. Despite several overestimations occurred before, RF-MEMS still finds its market position gradually. Qorvo made more than quadruple of its RF-MEMS sales from 145 \$M to 585 \$M from 2014 to 2017. Through integrating RF-MEMS switches within RF front ends to increase re-configurability over Wi-Fi, Bluetooth, and cellular bands belonging to 3G and 4G networks, tremendous commercial success is

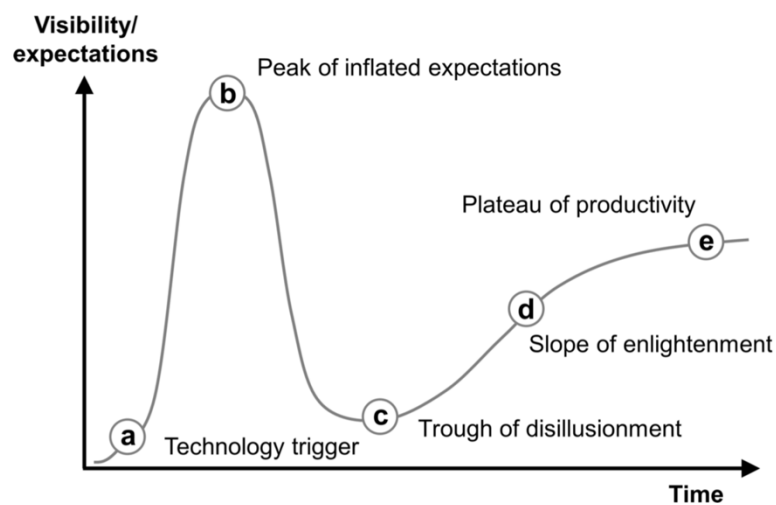
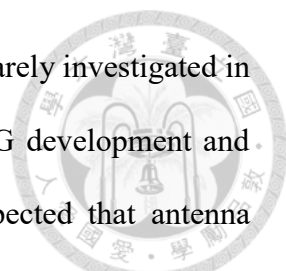


Fig. 1.10. Typical hype curve behavior elaborated by Gartner Inc. [20].

achieved. However, antenna is one of the key components which is rarely investigated in the field of RF-MEMS previously. Combined with the trends of 5G development and various applications, which will be discussed later, it can be expected that antenna miniaturization will play more and more important role. Before going into practical applications and design examples, antenna miniaturization theory will be briefly reviewed in the upcoming part.



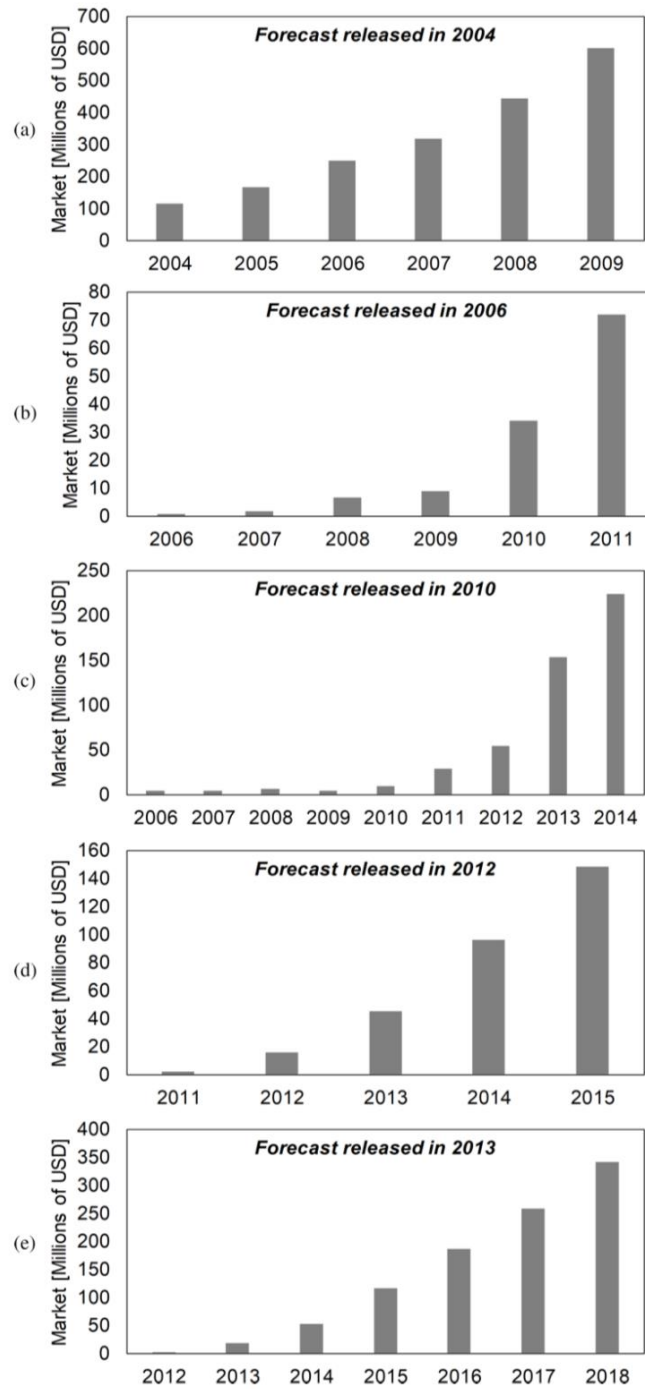
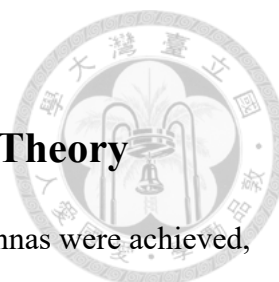


Fig. 1.11. Evolution of RF-MEMS market forecasts released in: (a) 2004; (b) 2006; (c) 2010; (d) 2012; (e) 2013 [21].



### 1.3 Brief Review on Antenna Miniaturization Theory

Regarding how the fundamental limits of electrically small antennas were achieved, many theoretical works have been done. The approach to analyze such an issue was firstly investigated in Chu's pioneer paper published in 1948 and quickly followed by Harrington and Wheeler in [22], [23] and [24]. The limits on electrically small antennas are studied firstly by assuming that the entire antenna structure within a sphere of radius  $r$  as shown in Fig. 1.12(a), sometimes known as "Chu sphere." Based on the concept of Chu sphere, electrically small antennas (or ESAs) are often defined as an antenna that satisfies the condition  $kr < 1$ , where  $k$  is the wave number  $\frac{2\pi}{\lambda}$ . The space outside the sphere was replaced by a number of independent equivalent circuits as shown in Fig.

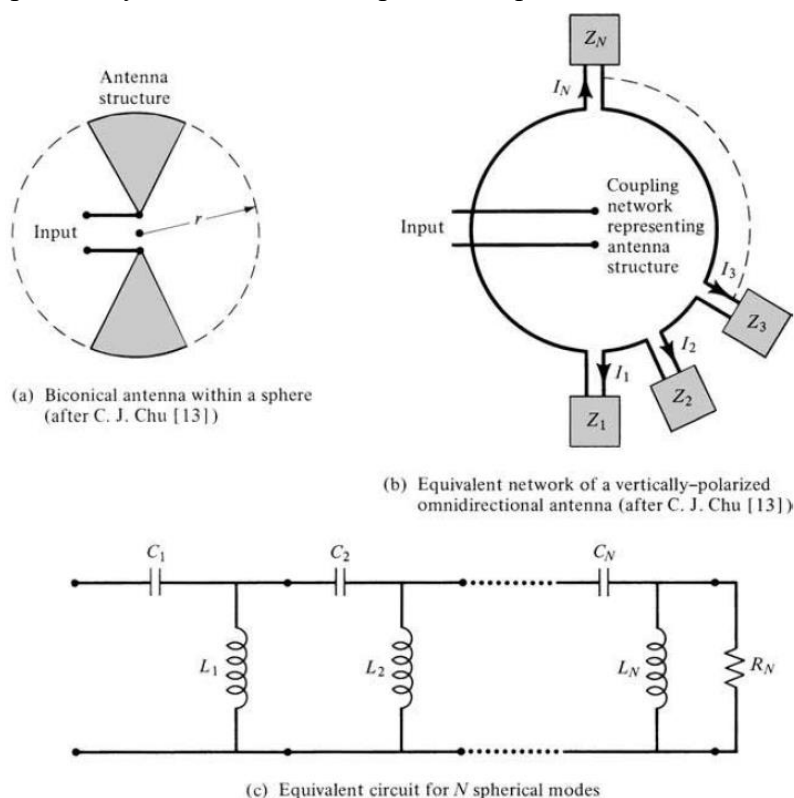


Fig. 1.12. Antenna within a sphere of radius  $r$ , and its equivalent circuit model [25].

1.12(b). For a lossless antenna, a single network section with a series  $C$  and a shunt  $L$  is identified as the equivalent circuit of each spherical mode [25]. Hence, the combined circuit can be seen as a ladder network of  $L - C$  sections (one for each mode) with a shunt resistive load, as shown in Fig. 1.12(c). The resistive load represents the normalized antenna radiation resistance, and the original antenna space problem can now be simplified as a circuit problem.

In addition to theoretical investigation, there are some works trying to examine the validity and existence of Chu limit. In the paper by Daniel F. Sievenpiper et al., the previous theoretical works are reviewed and measurement results are compared based on specific criteria [26]. To start,  $Q$  is defined as the ratio of stored energy  $W$  to radiated power  $P$  at a particular frequency  $\omega$  for an otherwise lossless antenna,

$$Q = \omega \frac{W}{P} \quad 1.3.1$$

where  $W$  is defined as

$$W = 2\text{Max}(W_m, W_e) \quad 1.3.2$$

$W_m$  and  $W_e$  are the time-average, non-propagating, stored magnetic and electric energy. Hansen [27] and later McLean [28] derived an expression for  $Q$  of the lowest order mode in terms of the electrical size of the antenna's

$$Q = \frac{1 + 2(ka)^2}{(ka)^3[1 + (ka)^2]} \cong \frac{1}{(ka)^3} \text{ with } ka \ll 1 \quad 1.3.3$$

Collin and Rothschild [29] calculated the energy associated with radiation from the total energy to find expressions for  $Q$  of each mode. The value for the lowest order spherical mode is given by

$$Q = \frac{1}{ka} + \frac{1}{(ka)^3} \quad 1.3.4$$

In Fante's work [30], he investigated gain and  $Q$  optimization including numerical results

for maximum  $G/Q$ . Yaghjian and Best [31] derived the relationship between  $B$  and  $Q$  through the maximum allowable voltage standing wave ratio VSWR, or  $s$

$$\text{Bandwith} \approx \frac{1}{Q} \left( \frac{s-1}{\sqrt{s}} \right) \quad 1.3.5$$

$$s = 2, Q = \frac{1}{\sqrt{2}B_{-10dB}} \quad 1.3.6$$

Since the radiation efficiency is always smaller than 1 and combined with 1.3.3, we can obtain the theoretical upper bound of the bandwidth-efficiency product

$$\eta \cdot \text{Bandwith}_{-10dB} < \frac{(ka^3)}{\sqrt{2}} \quad 1.3.7$$

The bandwidth efficiency products versus the electrical size for various published designs were shown in Fig. 1.13 [26]. The curves represents the theoretical limit that is derived by applying 1.3.5 to 1.3.4 using a VSWR of  $s = 2$  and including efficiency  $\eta$

$$B\eta = \frac{1}{\sqrt{2}} \left( \frac{1}{ka} + \frac{1}{n(ka)^3} \right)^{-1} \quad 1.3.8$$



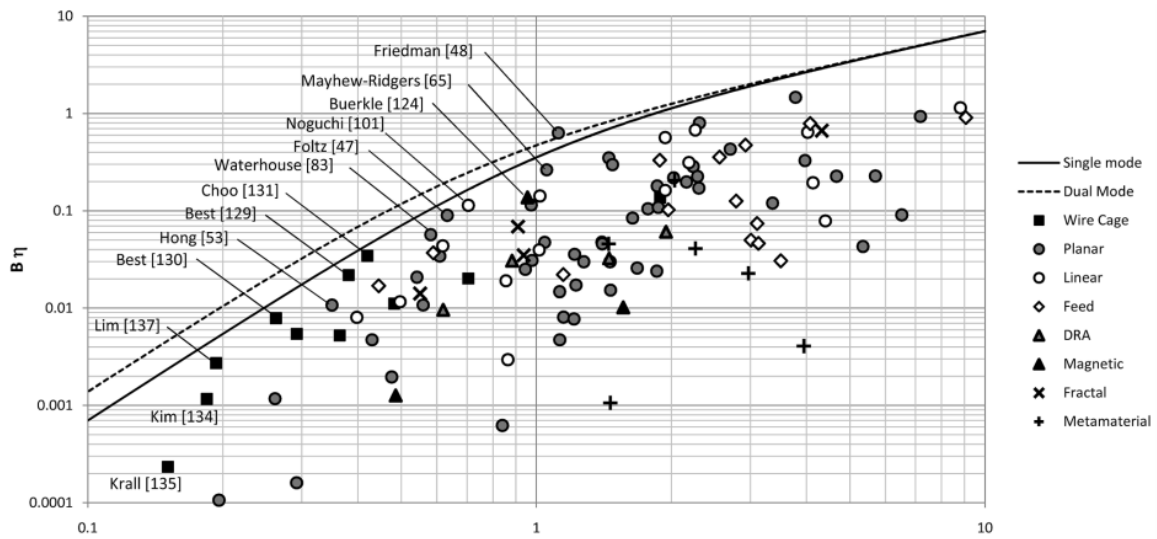



Fig. 1.13. Measured product for 110 antenna designs published in the IEEE T-AP by the end of 2010 [26].

where  $n = 1$  for linearly polarized or single-mode antennas, and  $n = 2$  for circularly polarized or dual-mode antennas. It was found that most of the works follow the Chu limit except the one done by Friedman in [32]. However, it was due to the extra matching circuit and the incomplete measurement data.

From the above discussion, we know that it's inevitable to face theoretical limit and need to tradeoff between bandwidth and efficiency while trying to miniaturize the antenna. What makes it worse is that traditional antennas adopted for miniaturized component, such as dipole, loop, or patch, struggle with image current effect as well as excessive storage of reactive energy between the radiating element and ground, not to mention ohmic losses. These effects will increase the radiation Q factor, make the antenna difficult to match and essentially kill the radiation efficiency. Hence, there are several works aiming at proposing innovative structure different from traditional one. They try to use mechanical resonance coupled with multiferroic material as the source of electromagnetic radiation. In 2019, the group of Draper Laboratory in Cambridge coined the name of "mechanical" and "antenna" as "mechenna" [33]. The basic concept is that mechanical



<b>Transmitter</b>	<b>Motion</b>	<b>Band</b>	<b>Ref</b>
Piezo-Electric / Surface Acoustic Wave Device	Body-Mode	UHF	Sinha [7-9]
Ferromagnetic/Piezoelectric Heterostructure	Body-Mode	VHF	Nan [10]
Polymer Electret Film	Rotation	SLF	Bickford [12]
Permanent Magnet	Rotation	ULF	Nagaraja [13]
Permanent Magnet	Rotation	ULF	Arnold [14]
Permanent Magnet	Rotation	ELF	Fawole [15]

Table 1. Summary of mechanical antenna transmitter experiments [33].

acoustic wave speed are typically several thousands (m/s). However, the speed of light in free space is in the order of  $3 \times 10^8$  (m/s). Assuming that they're both operating under the same resonant frequency, the mechanical resonant structure can be miniaturized by about the order of 5, which is fundamentally different from conventional one. Various kinds of "mechenna" are proposed based on different operational frequencies, integrating diverse antenna structures listed in Table 1. For example, an design for ULF band (300 Hz to 3000 Hz) was studied in [34] and that for UHF (300 MHz to 3 GHz) was discussed in [35], [36]. For UHF band, Zhi Yao proposed a theoretical framework based on FDTD Multiphysics numerical simulation and calculated theoretical lower bound of quality factor of such an antenna in 2015. It was found that this kind of antenna has the potential to approach the Chu limit even down to the size of  $ka \ll 1$  at the frequency of 1 GHz [35] – [43]. In [36], they firstly measure the RX/TX behavior based on nanoplate resonators (NPR) at around 60 MHz and circular resonating disk made of FeGaB at around 2.5 GHz with the device diameter of only 200  $\mu\text{m}$ , as shown in Fig. 1.14. They emphasized that strong radiation can be produced with zero biased magnetic field.

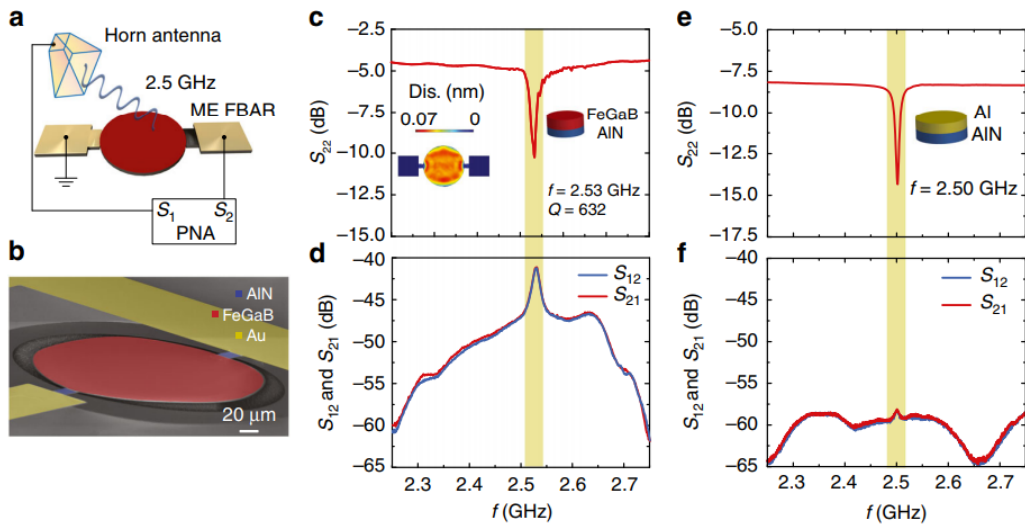
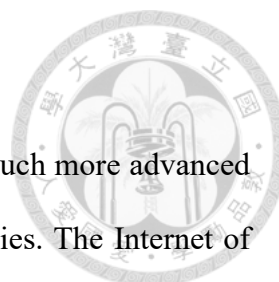


Fig. 1.14. ME FBAR antenna demonstrated in [36]. The longitudinal mode is excited and the radiation at 2.5GHz is detected with comparison of FeGaB to Al material.

However, in Zhi Yao's framework, ferromagnetic resonance is used to explain magnetoelectric coupling, which indeed requires an external biased magnetic field. Related research is still relatively new and in need of further study. In [36], it lacks explicit theoretical framework despite of evidences of experiments. Hence, I will still mainly follow the theoretical framework by Zhi Yao in the next sub chapter. This thesis is essentially based on Zhi Yao's structure and firstly tries to achieve polarization control with an innovative structure [41]. Before illustrating the operating principle of such devices, let's look at several potential applications for such an antenna.



## 1.4 Applications for Miniaturized Antenna

As mentioned above, 5G services will continuously facilitate much more advanced interconnection based on upgraded communication system capabilities. The Internet of Things (IOT) paradigm was presented for the futuristic digital world based on various concepts combined (see Fig. 1.15). One of the key enabling technology for IOT is the Radio frequency identification system (RFID) [44]. Typically, the IOT system architecture is generally divided into three layers: the perception layer, the network layer, and the service layer (or application layer). Perception layer is where the information is collected. It is also the core layer of IOT, such as sensors, wireless sensors network (WSN), tag and reader-writers, RFID system, camera, global position system (GPS), intelligent terminals, electronic data interface (EDI), objects, and so like. Network layer is called transport layer, including access network and core network, provides transparent data transmission capability. Service layer or application layer includes data management sub-layer and application service sub-layer [44]. When implementing IOT technology, RFID

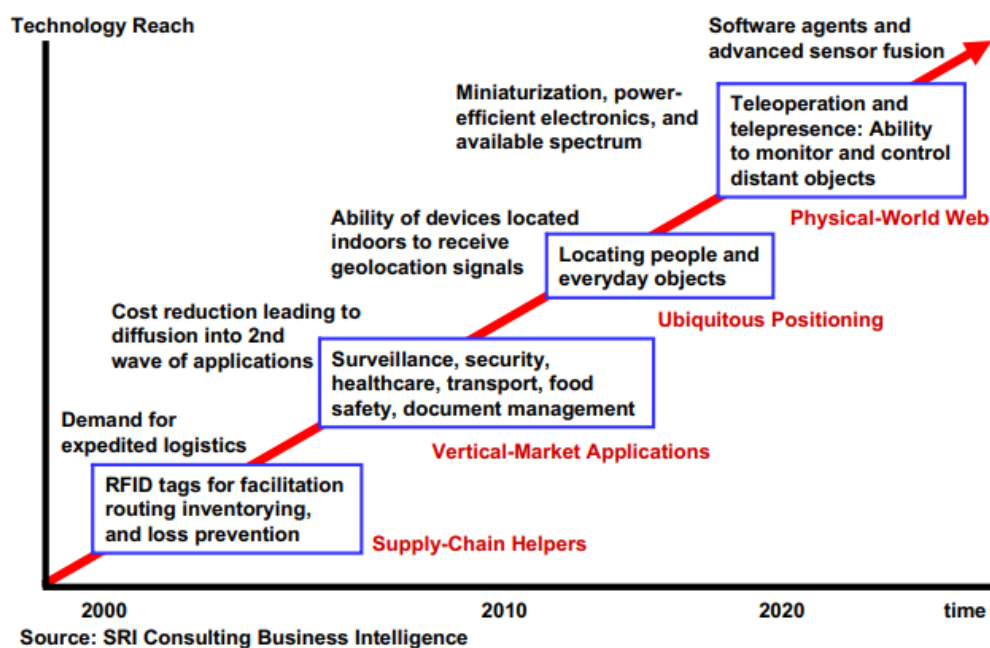


Fig. 1.15. Technology roadmap of Internet of Things (IOT) [44]

is often mentioned. The reason is that when the RFID reader communicates with the RFID tag using radio waves, the readers can be used to identify, track and monitor the objects attached with tags globally, automatically, and in real time. As a result, RFID is often seen as a prerequisite for the IOT. If all objects of daily life were attached with radio tags, they could be traced by computers [45].

The RFID technology was first appeared in 1945, as an espionage tool for the Soviet Union, which retransmitted incident radio waves with audio information. The IFF (Identification Friend or Foe) transponder was also introduced in the United Kingdom, which used by the allies in World War II to identify aircraft as friend or foe [44]. A typical RFID system is consisted of tags (transmitters/ responders) and readers (transmitters/receivers) as shown in Fig. 1.16 [44]. The tag is a microchip connected with an antenna, which can be attached to an object as the identifier of the object. Radio frequencies typically range from 100 kHz to 10 GHz. The tags are made with many different shapes, sizes, and capabilities but all RFID tags essentially have the components in common: antenna, integrated circuit, printed circuit board (or substrate). The main responsibility of antenna of RFID tag is to transmit and receive radio waves for the purpose of communication. The antenna can also be utilized to collect energy to drive other components without a battery, which is called energy harvesting [44].

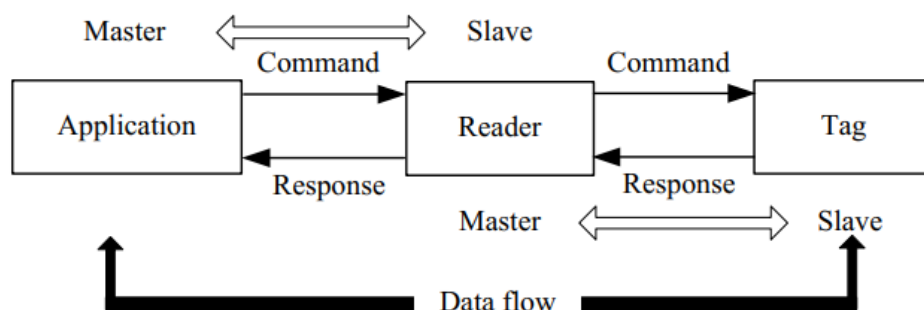


Fig. 1.16. The components of a RFID system

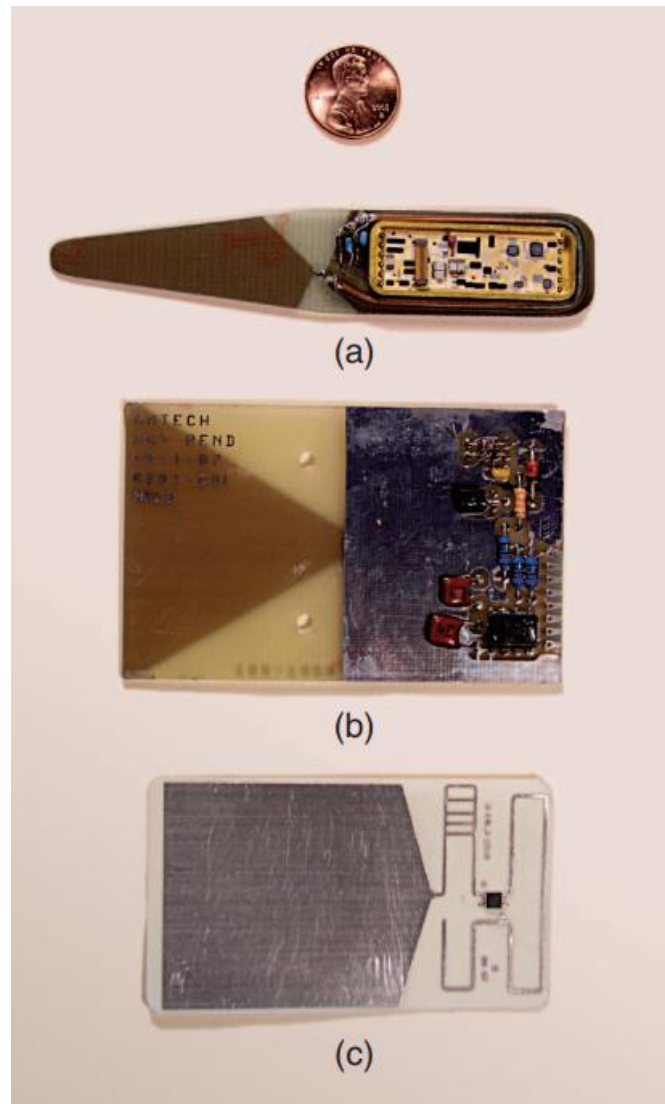
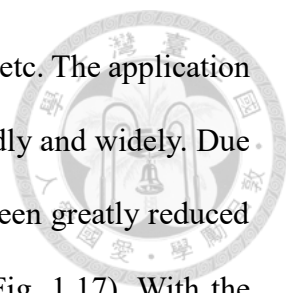


Fig. 1.17. Evolution of RFID tags compared in size to a penny from 12 bits to 1024 bits. The area of the circuitry of the tag has been reduced greatly except the area occupied by antenna [46].

As for the functions of RFID system generally include three aspects: monitoring, tracking, and supervising [44]. Most successful applications include supply chain management, production process control, and objects tracking management. Now RFID are gradually used in many fields like: Logistics, Supply Manufacturing, Agriculture Management, Health Care and Medicine, Marine Terminal Operation, Military and Defense, Payment Transactions, Environment Monitor and Disaster Warning,



Transportation and Retailing, Warehousing and Distribution Systems etc. The application of RFID in diverse areas will gradually expand the spread more rapidly and widely. Due to benefits of Moore's Law, the relative size of RFID circuitry has been greatly reduced with enhanced capabilities except one part—antenna(as shown in Fig. 1.17). With the growing needs of renewing RFID technology, the core technical challenge lies in antenna miniaturization [44]. The advancement regarding antenna miniaturization is especially needed to realize the IOT paradigm.

In addition to the application of RFID in IOT, there are also needs for miniaturized antenna in biomedical application like implantable and wearable antennas [47]. The purpose of using antennas in a Bio-Implant can be either for telecommunication or therapy. Telecommunication means that targeted information is sent into or out of the host body. Therapy is that the antennas are used to provide energy, as in hyperthermia for instance. The first use of antennas inside a living body is quite early about 60 years ago [48] and many designs have been proposed from then, focusing on sensing and therapy [49], [50], [51]. However, in telemetry applications the system should send data for a certain distance so radiation efficiency and bandwidth are important in order to maintain high data rate. In early days, most implantable communication relied on inductive coupling at low frequency with an external coil but the transmission range is too short. Later, ISM band at 2.45 GHz and the definition of the Medical Radio (or MedRadio) band which is defined between 401 and 406 MHz for medical telemetry are used [52].

Typically implants are required to be in the range of 1 to 10 mm in diameter for a length of 5 to 35 mm, while in the MedRadio band the free space wavelength is around 74 cm, and in the ISM band it is around 12 cm [47].  $\frac{\lambda_0}{30}$  and  $\frac{\lambda_0}{5}$  for the MedRadio and ISM bands, respectively will likely be used. Hence, ESAs are strongly needed for such

an application. The other issue for the implantable antenna is that it will be directly surrounded by lossy biological tissues. Hence oftentimes the design problem becomes the amount of power the antenna is able to transmit out of the host body. The design example is shown in Fig. 1.18 and Fig. 1.19.

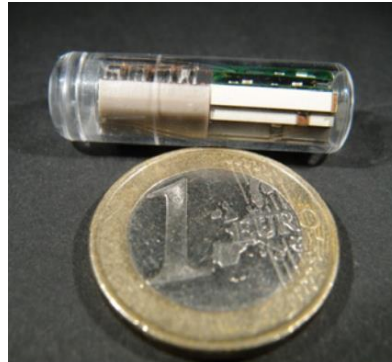
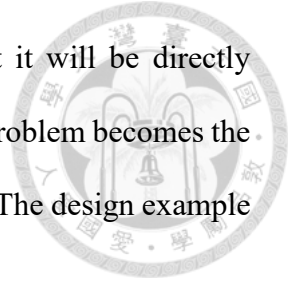


Fig. 1.18. Implant with antenna and circuitry [47]

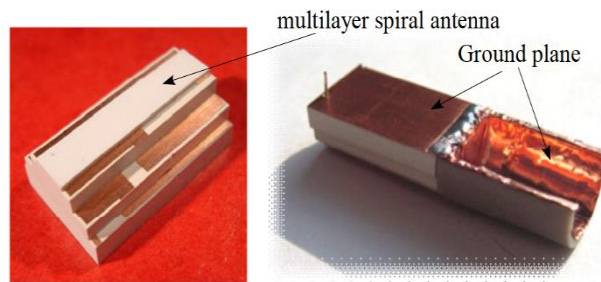


Fig. 1.19. Dual band antenna [47]



As for wearable antennas, it's often divided into textile and non-textile antennas. different textile versus non-textile designs were reviewed in detail in [53]. Sometimes they are also called smart clothes. Wearable antennas are expected to facilitate the realization of IOT paradigm. However, different from the implantable antennas, the major challenge of designing wearable antennas is to make the technology invisible to the user [53]. Also, the robustness of the antenna performance to the operating scenario such as mechanical solicitations and operations such as washing and ironing is important [54], [55]. The immunity of EM waves to the proximity of human body should also be achieved. As a result, a miniaturized antenna with acceptable performance under such a harsh EM environment is necessary [53].

In addition to higher frequency range, there are also needs in lower frequency range. VLF band is often used for submarine communication since the signals are able to propagate through the ocean(Fig. 1.22 and Fig. 1.21). Likewise, low frequency (LF) electromagnetic antennas are used for trans-continental communication without the help of satellite [34]. The frequencies lying between 300 Hz to 3 KHz have been designated as Ultra Low Frequency (ULF) with corresponding wavelengths from 1000 Km to 100 Km. The frequency within this range can penetrate soil and water, as shown in Fig. 1.23. However, construction of ULF communication systems is vastly expensive since the

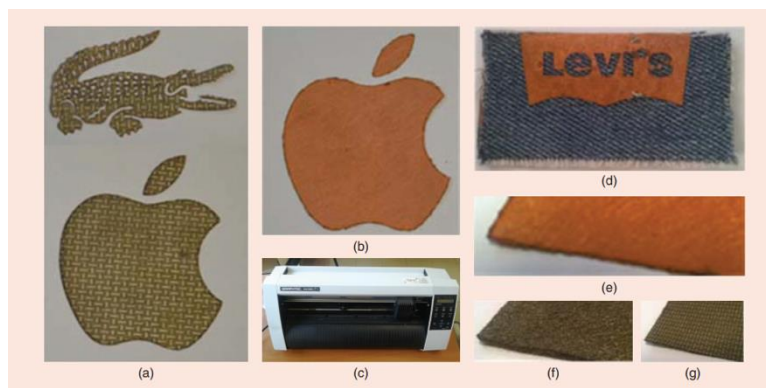


Fig. 1.20. Photos of prototypes and nonwoven conductive fabrics (NWCf) [53].

wavelength of operation at these frequencies are comparable to the distances between cities and states. For example, the navy's VLF antenna in Cutler, Maine occupies 2000 acres on a peninsula and consists of 26 towers 850 to 1000ft high (Fig. 1.24). It consumes 18 MW of power from a dedicated power plant [57]. Hence, an alternative with the concept of miniaturized radiating source using Directly Modulated Spinning Magnet Arrays was proposed in Fig. 1.25 [34].



Fig. 1.22. Underwater communications [34]



Fig. 1.21. Underground communications [34]

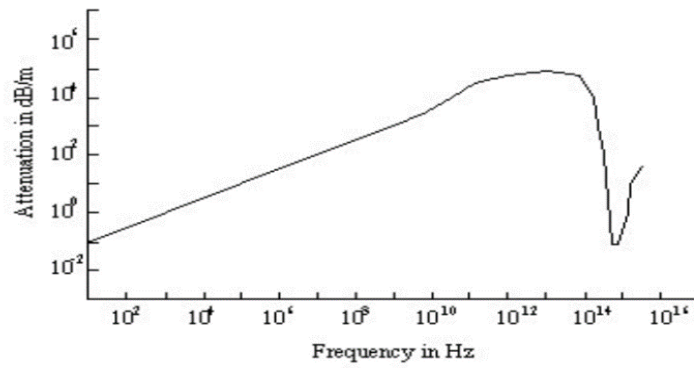


Fig. 1.23. Attenuation of EM wave passing through Sea Water [56]

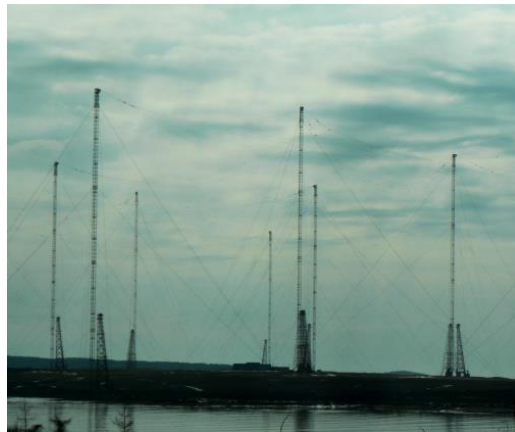


Fig. 1.24. US Navy's VLF antenna in Cutler, Maine [34]

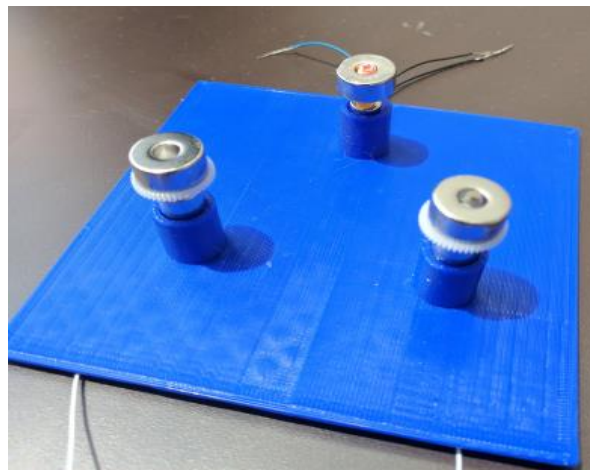


Fig. 1.25. Spinning Magnet Array [34]

## Chapter 2 Background and theory



### 2.1 Piezoelectric and Magnetic Material for Microwave Application

Direct piezoelectric effect was firstly reported by Pierre and Jacque Curie in 1880 and converse one by Lippmann in 1881. The word “piezoelectricity” itself means electricity resulting from pressure and latent heat [58]. However, not until the discovery of PZT and BaTiO<sub>3</sub> in the 1950s relative application began to emerge. In 1971, Jaffe et al. discovered piezoelectric ceramics and then use of piezoelectric materials in various applications. Nowadays there are estimated about 30% of the material available in the world exhibiting piezoelectricity [59]. Although a wide variety of materials show this property, only a few of them have found useful applications in science. The piezoelectric materials are classified in [60]: “ (1) Single crystals: Quartz, LiNbO<sub>3</sub>, Lithium Tantalate (LiTaO<sub>3</sub>) (2) Poly crystalline materials: BaTiO<sub>3</sub>, PbTiO<sub>3</sub>, Lead Zirconate(PbZrO<sub>3</sub>) (3) Relaxator Ferro electrics: Lead Magnesium Niobate-Lead Titanate (PMN-PT), Lead Zirconium Niobate-Lead Titanate (PZN-PT) (4) Polymers: PVDF, Poly (vinylidene

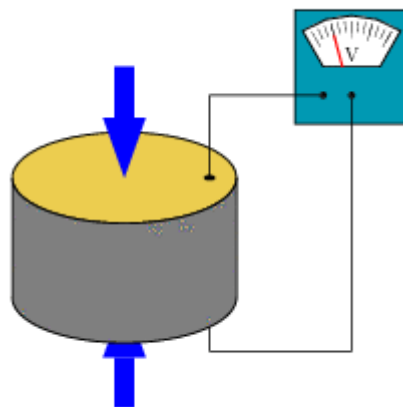
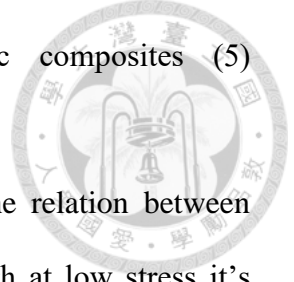


Fig. 2.1. Concept illustration of a piezoelectric disk generating a voltage when deformed.

difluoride- trifluoro ethylene) P(VDF-TrFE), Polymer-Ceramic composites (5)  
Piezoelectric Paper.”



Equations 1.5.1 and 1.5.2 are commonly used to describe the relation between electromechanical properties of the piezoelectric material. Although at low stress it's mainly linear, the produced stress will tend to be nonlinear as the “electrical stress” increases. However, most of the piezoelectric materials in sensing applications will confine the application in the linear zone [58]:

$$x_i = S_{ij}^{D_{const}} \sigma_j + d_{mj} E_m \quad 1.5.1$$

$$D_m = d_{mj}^{D_{const}} \sigma_i + \epsilon_{ik} E_k \quad 1.5.2$$

where  $i, j = 1, 2, \dots, 6$  and  $m, k = 1, 2, 3$  refer to different directions within the material coordinate system

where

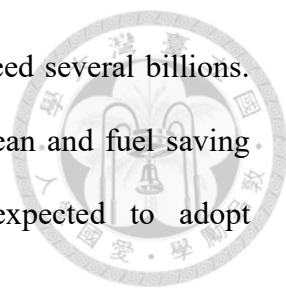
$\sigma$	is Stress Vector (N/m <sup>2</sup> ),
$x$	is Strain Vector (m/m),
$E$	is Applied Electrical field in (V/m),
$\epsilon$	is permittivity in (F/m),
$d$	is piezoelectric constant (m/V),
$S$	is Matrix of compliance coefficients (m <sup>2</sup> /N),
$D$	is Electrical displacement (C/m <sup>2</sup> ),

Since the discovery of piezoelectricity, there are many applications based on this fundamental phenomenon. An overall collection of existing applications of piezoelectricity is shown in Table 2 [61]. The bold characters indicate where the number



Category	Innovation field	Materials and shaping	Main application
Frequency control and signal processing	<b>Frequency-/time standards</b>	Quartz single crystal plates	Precise frequency control
	Mechanical frequency filters	Ceramic plates of specifically tailored PZT	Inexpensive frequency control and filtering
	<b>Surface acoustic wave (SAW) devices</b>	LiNbO <sub>3</sub> , LiTaO <sub>3</sub> , Quartz single crystal substrates	Passive signal processing for wireless communication, identification, sensing, etc.
Sound and ultrasound (US)	Bulk acoustic wave (BAW) devices	Ceramic plates of hard PZT AlN, ZnO thin films	
	<b>Buzzer</b>	Ceramic tapes of soft PZT	Sonic alerts
	Microphones and speakers	Ceramic tapes of soft PZT PZT thin films	Telephone, blood pressure
	<b>Ultrasonic (US) imaging</b>	Diced plates of soft PZT or of PZNT single crystals PZT thin films	Medical diagnostics
	Hydrophonics	Hard PZT of various shapes soft PZT composites	Sources and detectors for sound location
	<b>High power transducers and shock wave generation</b>	Ceramic discs of hard PZT	Machining, US cleaning, lithotripsy
Actuators and motors	Atomizer	Ceramic discs of soft PZT	Oil atomizers, humidifiers, aerosols
	Air ultrasound	Ceramic discs of soft PZT	Distance meter, intrusion alarm
	<b>Printers</b>	Bars, tubes, multilayer ceramics of soft PZT PZT thin films	Needle drives and ink jet
	Motors and transformers	Rings, plates of hard PZT soft PZT multilayer ceramics PZT thin films	Miniaturized, compact motors and transformers
	Bimorph actuators	PZT multilayer ceramics	Pneumatics, micropumps, braille for the blind
	Multilayer actuators	Multilayer stacks of soft PZT	Fine positioning and optics
	Injection systems	Multilayer stacks of soft PZT	Automotive fuel valves
Sensors	Acceleration sensors	Rings, plates of soft PZT	Automotive, automation, medical
	Pressure and shock-wave sensors	LiNbO <sub>3</sub> substrates PVDF foils	
	Flow sensors	Soft PZT discs	
	Mass sensitive sensors	Quartz discs, Quartz substrates ZnO, AlN thin films	
Ignition Adaptronics	<b>Ignition Adaptive devices</b>	Hard PZT cylinders Various shapes of soft PZT, multilayer stacks of soft PZT	Gas and fuel ignition Active noise and vibration cancellation, adaptive control, airtail filter control

Table 2. Piezoelectricity, innovation fields, and important applications [61]



of currently used piezoelectric samples have been estimated to exceed several billions. Piezoelectric sensors, valves, and injectors are key elements for clean and fuel saving motor management. Hence for automotive applications are expected to adopt piezoelectric materials more widely.

As shown in the Table 2, surface acoustic wave devices have been heavily and widely applied in many areas. [62] First applications of SAW devices were in military systems, but these applications never reached high volume. Around 1975, Philips, Plessey, and Siemens started the fabrication of TV intermediate frequency (IF) filters in low volume. In Fig. 2.2, the size reduction can be observed compared to TV IF conventional filter. Based on the industrial experiences by SAW devices, there are also more and more potential products developed on bulk acoustic wave or BAW devices. This is also one of the key part of the proposed new antenna structure in [37]. The operation principle will also be explained in more details later.

Generally speaking, the main market segmentation between SAW and BAW is the resonant frequency. SAW resonant frequency will be limited by the gap of interdigitated finger electrodes. However, BAW is typically more expensive and hard to fabricate. The

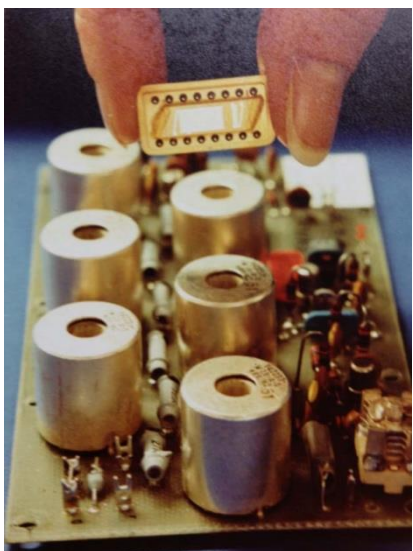


Fig. 2.2. Comparison of a classical LC TV IF filter with an SAW TV IF filter [62]

first BAW duplexers were employed in a cellular phone with a low shape factor around 2001 and were fabricated by Sanyo for the service provider Sprint. SAW filters are dominating the frequency range up to 1 GHz, and BAW and SAW filters are competing for their share in the frequency range above 1 GHz (Fig. 2.3). It is estimated that in 2015 the number of RF filter functions built into cellular phones exceeded 40 billion [63].

BAW filters mostly are fabricated in two types. These two technologies are the FBAR (also called free-standing membrane type) and SMR [64]. The one fundamental difference between SMRs and FBARs is the means by which the acoustic energy (or the BAW thickness mode) is trapped at the bottom electrode. For FBAR, an air cavity is formed between the bottom electrode and the carrier wafer in order to make sure that the main mode is trapped, as shown in Fig. 2.4(a). In the SMR, the Bragg reflector is placed underneath the bottom electrode to effectively trap this mode, as shown in Fig. 2.4(b). The acoustic reflector is constructed using a stack of roughly  $\lambda/4$  thin-film layers with alternating low and high acoustic impedance. Nowadays, BAW filter technologies are already widely used in smartphone components, such as duplexer and quadplexer. For example, in iPhone 6 there are already many band operation using BAW filter as shown

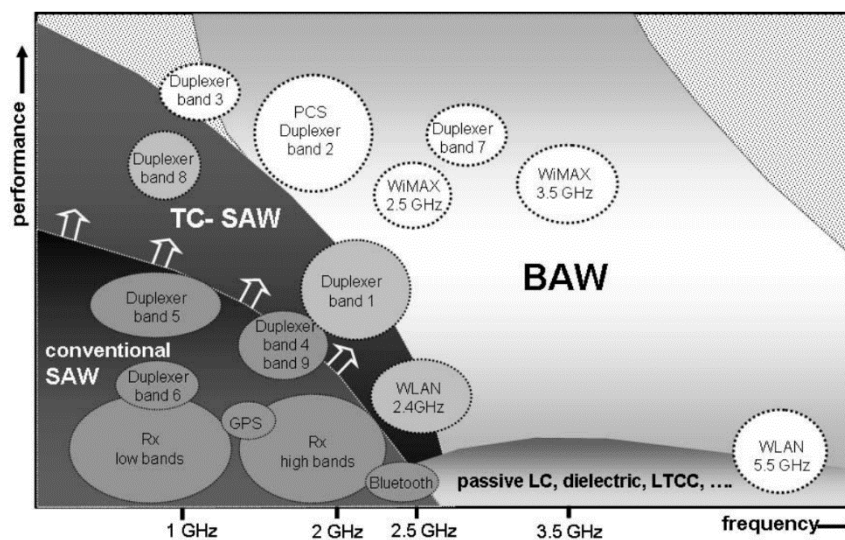
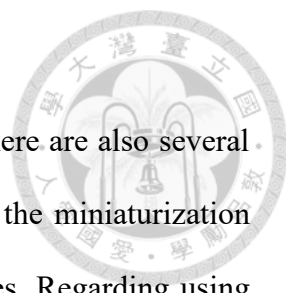


Fig. 2.3. Application space regarding frequency spectrum or RF filters [63]





in Fig. 2.5.

In addition to piezoelectric materials used in RF component, there are also several magnetic properties applied in the antenna miniaturization. One of the miniaturization techniques is modifying the substrate magnetic or electric properties. Regarding using modified material properties to achieve antenna miniaturization, the preliminary attempt is focusing on enhancing permittivity substrate. However, because of the strong

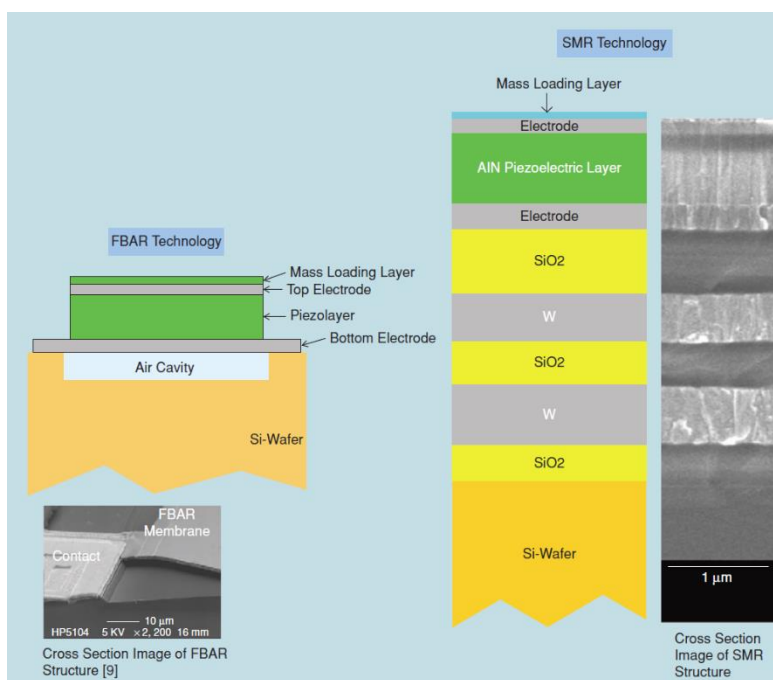


Fig. 2.4. (a) FBAR and (b) SMR structures. [65]



Fig. 2.5. Example BAW filters used in iPhone 6(EPFL online course MEMSx).

capacitive coupling between the antenna and the antenna's ground plane its performance is considerably degraded. To overcome this problem, instead of using a high dielectric material (only  $\epsilon$ ), one can use magneto-dielectric substrates (both  $\epsilon$  and  $\mu$ ) [66]. This way by choosing moderate values of  $\epsilon_r$  and  $\mu_r$  the same miniaturization factor ( $n = \sqrt{\epsilon_r \mu_r}$ ) can be achieved while keep the coupling between the antenna and ground plane low. In other words, the capacitive property of the resonant antenna is decreased and by addition of some inductance is introduced that can further counteract the capacitive behavior [67]. This will improve both the efficiency and bandwidth of the antenna. It has been shown by Hansen and Burke [68], that the 0<sup>th</sup> order bandwidth for an antenna over a magneto-dielectric substrate with thickness can be approximated by

$$BW = \frac{96 \sqrt{\frac{\mu}{\epsilon}} \frac{t}{\lambda_0}}{\sqrt{2}[4 + 17\sqrt{\mu\epsilon}]} \quad 1.5.3$$

, where  $t$  is the dielectric thickness. Thus, for a given miniaturization factor (constant  $\sqrt{\epsilon_r \mu_r}$ ) the antenna bandwidth can be enhanced by increasing  $\frac{\mu_r}{\epsilon_r}$  ( $\mu_r > \epsilon_r$ ). Other RF components also use lossy properties of magnetic materials, like isolator, circulator, phase shifters (Fig. 2.6) [69]. Piezoelectric and magnetic material are both used for RF component fabrication for a long time, especially in antenna miniaturization areas. In SAW or BAW filter, since the device relies on mechanical wave (BAW) resonance instead of the typical electromagnetic resonance, the characteristic length scale of the device is reduced by a factor of  $10^5$ . The similar concept can also be used for antenna design the source of EM radiation. In the following chapter, I will illustrate fundamental operation principle of so-called bulk acoustic wave-mediated multiferroic antenna or magneto-electric transducer (Fig. 2.7), which all refer to the device that are made of multiferroic

composite and can be used as radiation source. Before the closing of this chapter, let's examine some more basic definition of material properties. Actually, piezoelectric and magnetostrictive properties both belong to a more complex concept called "multiferroic" material, which was coined by Schmid in 1994 [70]. Right after that, there are much more of researches studying this fascinating properties, though it's not so common in the field of antenna study. Multiferroic materials are defined as the materials which show at least two, and sometimes all three, types of "ferroic" ordering in the same phase. The "ferroic" could be the orderings of ferroelectric, ferromagnetic and ferro-elastic. These relations are further described by the genres of applied field and the properties to exhibit a corresponding spontaneously polarized state. Fig. 2.8 summarizes the meaning of multiferroics [71].

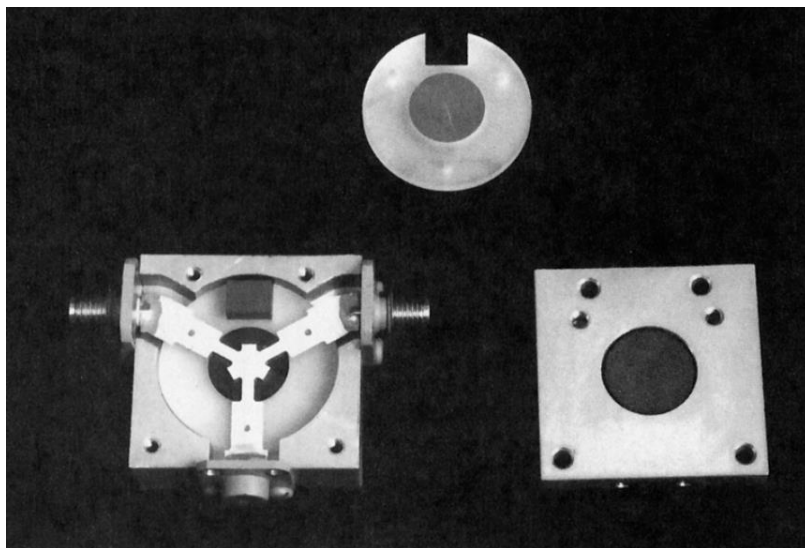


Fig. 2.6. Photograph of a disassembled ferrite junction circulator, showing the stripline conductor, the ferrite disks, and the bias magnet. [69]

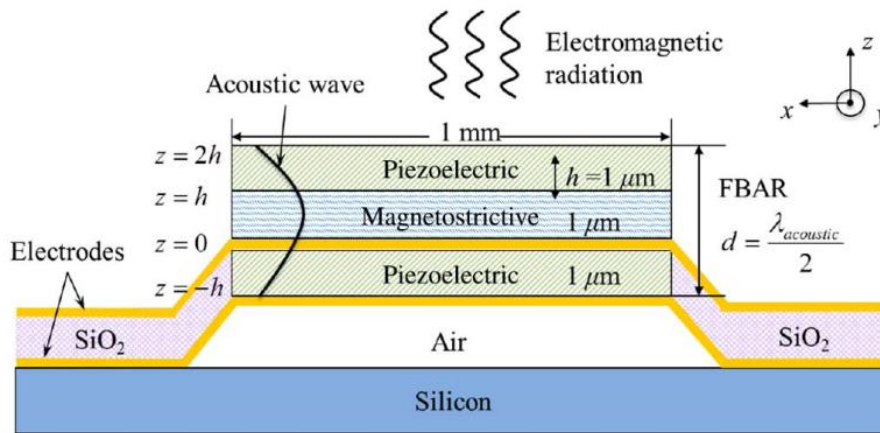


Fig. 2.7. BAW-resonance-based antenna [36].

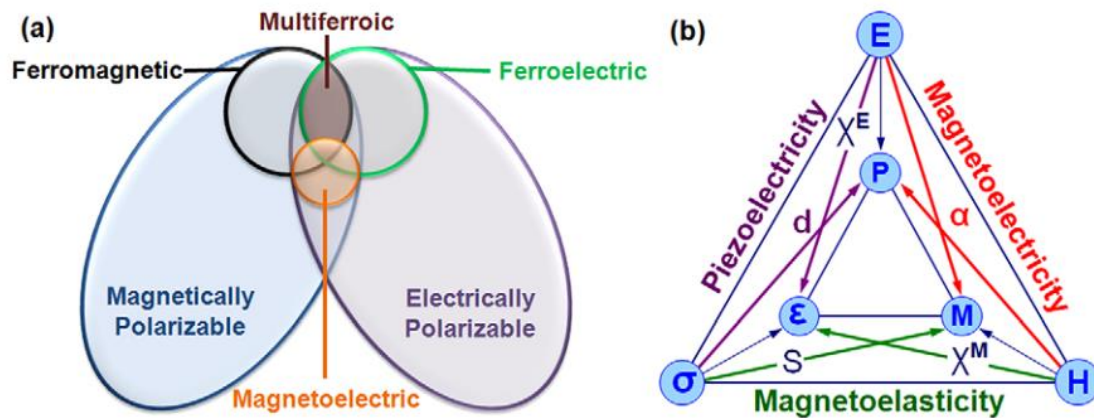


Fig. 2.8. (a) Relationship between multiferroic and magnetolectric materials.

Illustrates the requirements to achieve both in a material. (b) Schematic illustrating different types of coupling present in materials [71].



## 2.2 Dynamic Magnetization as a Radiation Source

As discussed in the previous chapter, traditional antennas are limited in their efficiency and performance due to the use of conductive currents as the radiation source. Quality factor is limited by the stored energy between ground and antenna. Also, radiation efficiency will be further decreased by image current. As a result, a new mechanism for the generation of the radiation is required to overcome these challenges. Although the work in Nat. Comm. by Nan et al. they propose the experimental evidences for the magneto-electric transducers [36], there's not much theoretical explanation for the mechanism in their work. Especially they emphasize on the merit of zero external magnetic bias field needed, which contradicts existing theory by Zhi Yao et al. [37] Hence for the theoretical description in this chapter, I mainly follow the theory by Zhi Yao and Sidhant's work [72]. To start, we know that Faraday's Law and Ampere's Law:

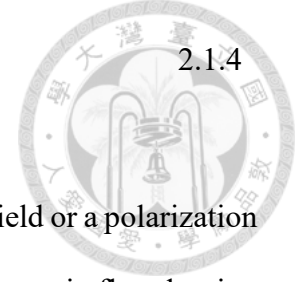
$$\vec{\nabla} \times \vec{E} = -\frac{\partial \vec{B}}{\partial t} \quad 2.1.1$$

$$\vec{\nabla} \times \vec{H} = \frac{\partial \vec{D}}{\partial t} + \sigma \vec{E} \quad 2.1.2$$

Here  $\vec{j} = \sigma \vec{E}$  is the extrinsic conduction current density. If we want to avoid the effect of conduction current, we need this term to be set to be 0. Hence, we can only control electrical or magnetic flux densities to generate radiation. The next question to is how to generates dynamic flux density. The constitutive laws for the electric and magnetic flux densities in a material are given below:

$$\vec{D} = \epsilon_0 \vec{E} + \vec{P} \quad 2.1.3$$

$$\vec{B} = \mu_0(\vec{H} + \vec{M})$$



To generate an electric flux density,  $\vec{D}$ , it either comes from electric field or a polarization (electric dipole moment per unit volume). Similarly to generate a magnetic flux density,  $\vec{B}$ , it either comes from a magnetic field or a magnetization (magnetic dipole moment per unit volume). However, for the operation of electric or magnetic field often require waveguides which are quite bulky. As a result, we need to control the polarization and the magnetization to generate the dynamic flux density.

Typically, we often illustrate antenna radiation mechanism from an infinitesimal dipole source. In the case of the dipole, the radiation is created by a periodical sinusoidal charge movement. Physically, this is identical to an electrical dipole moment which can be seen as the same operation concept for polarization control. From equivalence theorem [25] we know that the loop antenna acts as a magnetic dipole moment with a periodically varying amplitude. Hence, effective magnetic current density can be used to describe a dynamic magnetization:

$$\begin{aligned} \vec{\nabla} \times \vec{H} &= \frac{\partial \vec{D}}{\partial t} = \frac{\partial}{\partial t} (\epsilon_0 \vec{E} + \vec{P}) \\ &= \epsilon_0 \frac{\partial \vec{E}}{\partial t} + \frac{\partial \vec{P}}{\partial t} \\ &= \epsilon_0 \frac{\partial \vec{E}}{\partial t} + \vec{J}_{p,eff} \end{aligned} \quad 2.1.5$$

$$\begin{aligned}
\vec{\nabla} \times \vec{E} &= -\frac{\partial \vec{B}}{\partial t} = -\frac{\partial}{\partial t} (\mu_0 (\vec{H} + \vec{M})) \\
&= -\mu_0 \frac{\partial \vec{H}}{\partial t} - \mu_0 \frac{\partial \vec{M}}{\partial t} \\
&= -\mu_0 \frac{\partial \vec{H}}{\partial t} + \vec{J}_{M,eff}
\end{aligned}$$



$\vec{J}_{P,eff}$  is the effective electrical current density due to a dynamic polarization, while  $\vec{J}_{M,eff}$  is the effective magnetic current density due to a dynamic magnetization. Magnetic current density is a fictitious concept but useful for the analysis. Like the dynamic electric polarization, this fictitious magnetic current density can also act as a radiation source.

## 2.3 Sources of Dynamic Magnetization

A magnetic moment can be seen as a microscopic current loop. For example, an electron orbits about a nucleus or quantum mechanical spin (Fig. 2.9). The magnetization in a material is due to the sum of angular momenta of electrons from orbital motion about a nucleus and spin about their own center of mass, quite similar to the Earth spinning about its own axis while simultaneously orbiting the sun. To analyze the response of a magnetic moment to a torque, the analysis in Pozar is used here [69]. The relation between magnetic moment  $\vec{p}_m$  and electron of its angular momentum  $\vec{s}$  can be defined as

$$\vec{p}_m = -\gamma\vec{s} \quad 2.2.1$$

where  $\gamma = 1.759 \times 10^{11}$  (Coulomb/kg) is called the gyromagnetic ratio. For a

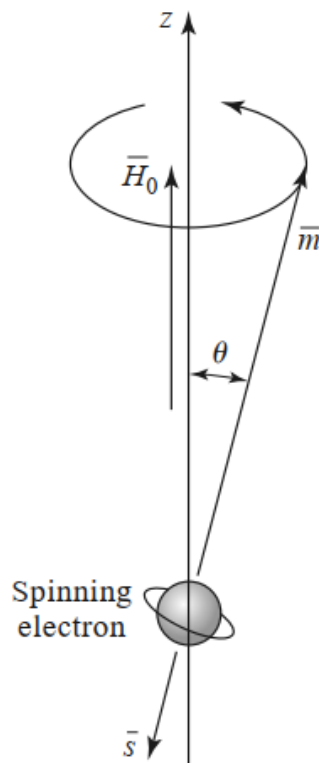


Fig. 2.9. Spin magnetic dipole moment and angular momentum vectors for a spinning Electron [69].



magnetic moment in free space, the torque on the moment due to the external field,  $\vec{B}_0$  is

$$\begin{aligned}\vec{T} &= \vec{p}_m \times \vec{B}_0 = \mu_0 \vec{p}_m \times \vec{H}_0 \\ &= -\mu_0 \gamma \vec{s} \times \vec{H}_0\end{aligned}\quad 2.2.2$$

Here  $\vec{T}$  is the net torque. Since torque is the time derivative of the angular momentum, with 2.2.1 and 2.2.2 together we have

$$\frac{d\vec{s}}{dt} = \frac{-1}{\gamma} \frac{d\vec{p}_m}{dt} = T = \mu_0 \vec{p}_m \times \vec{H}_0 \quad 2.2.3$$

$$\frac{d\vec{p}_m}{dt} = -\mu_0 \gamma \vec{p}_m \times \vec{H}_0 \quad 2.2.4$$

Neglecting domain wall motion, 2.2.4 can be used to describe the magnetization  $\vec{m}$  of the material.

$$\frac{d\vec{m}}{dt} = -\mu_0 \gamma \vec{m} \times \vec{H}_0 \quad 2.2.5$$

Ideally in the presence of a steady field, solutions of this equation show that the magnetization will keep precessing in a circular motion about the applied magnetic field (Fig. 2.9). Assuming that there are  $N$  unbalanced electron spins (magnetic dipoles) per unit volume, so that the total magnetization  $\vec{M} = N\vec{m}$ . Solve equation 2.2.5 by assuming there are only z component for  $\vec{H}_0$  we have

$$m_x = A \cos \omega_0 t \quad 2.2.6$$

$$m_y = A \sin \omega_0 t \quad 2.2.7$$

Where

$$\omega_0 = \mu_0 \gamma \vec{H}_0 \quad 2.2.8$$

is called the Larmor, or precession, frequency.

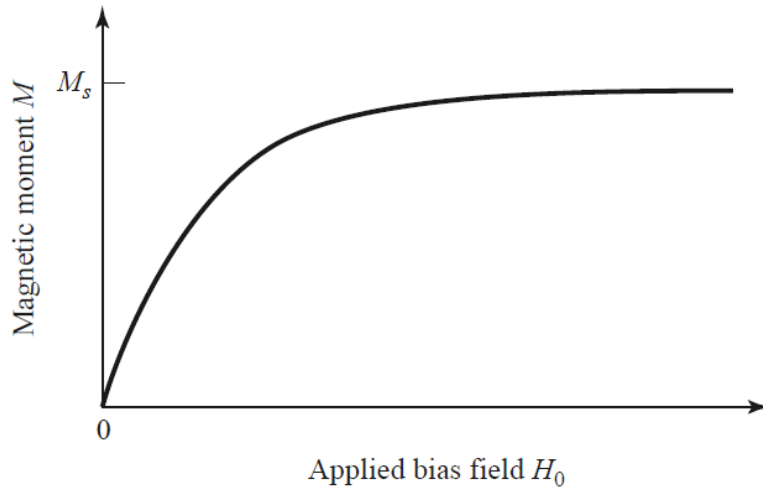


Fig. 2.10. Magnetic moment of a ferrimagnetic material versus bias field  $\vec{H}_0$  [69].

As the strength of the bias field  $\vec{H}_0$  is increased, more magnetic dipole moments will align with  $\vec{H}_0$  until all are aligned, and  $\vec{H}$  reaches an upper limit, as shown in Fig. 2.10. When magnetic moments stop to increase,  $\vec{M}_s$  is denoted as the saturation magnetization.  $\vec{M}_s$  is a physical property of the ferrite material, and it typically ranges from  $4\pi\vec{M}_s = 300\text{--}5000$  G [69]. Below saturation, ferrite materials can be very lossy so it typically operates at saturation state. Consider the interaction of a small AC (microwave) magnetic field with a magnetically saturated ferrite material. It will force the precession of the dipole moments around  $\vec{H}_{0,z}$ . If  $\vec{H}$  is the applied AC field, the total applied is

$$\vec{H}_t = H_0\hat{z} + \vec{H} \quad 2.2.8$$

where we assume that  $|\vec{H}| \ll H_0$ . This field produces a total magnetization in the ferrite material given by

$$\vec{M}_t = M_s\hat{z} + \vec{M} \quad 2.2.9$$

where  $M_s$  is the (DC) saturation magnetization and  $\vec{M}$  is the additional (AC) magnetization (in the xy plane) caused by  $\vec{H}$ . Substituting (2.2.9) and (2.2.8) into (2.2.5) gives the component equations of motion. Solve this equations of motion and we will

have

$$\frac{d^2 M_x}{dt^2} + \omega_0^2 M_x = \omega_m \frac{dH_y}{dt} + \omega_0 \omega_m H_x \quad 2.2.10$$

$$\frac{d^2 M_y}{dt^2} + \omega_0^2 M_y = -\omega_m \frac{dH_x}{dt} + \omega_0 \omega_m H_y \quad 2.2.11$$



where  $\omega_0 = \mu_0 \gamma H_0$  and  $\omega_m = \mu_0 \gamma M_S$ . If the AC  $\vec{H}$  field has an  $e^{j\omega t}$  time-harmonic dependence, the AC steady-state form of the equation 2.2.10 and 2.2.11 reduces to the following phasor equations:

$$(\omega_0^2 - \omega^2)M_x = \omega_0 \omega_m H_x + j\omega \omega_m H_y \quad 2.2.12$$

$$(\omega_0^2 - \omega^2)M_y = -j\omega \omega_m H_x + \omega_0 \omega_m H_y \quad 2.2.13$$

2.2.12 and 2.2.13 can be combined together and write in tensor susceptibility  $[\chi]$  to relate  $\vec{H}$  and  $\vec{M}$

$$\vec{M} = [\chi]\vec{H} = \begin{bmatrix} \chi_{xx} & \chi_{xy} & 0 \\ \chi_{yx} & \chi_{yy} & 0 \\ 0 & 0 & 0 \end{bmatrix} \vec{H} \quad 2.2.14$$

where elements of  $[\chi]$  are defined as

$$\chi_{xx} = \chi_{yy} = \frac{\omega_0 \omega_m}{\omega_0^2 - \omega^2} \quad 2.2.15$$

$$\chi_{xy} = -\chi_{yx} = \frac{j\omega \omega_m}{\omega_0^2 - \omega^2} \quad 2.2.16$$

Similarly, tensor permeability can be defined by the relation between  $\vec{B} = [\mu]\vec{H}$ .

In reality, it has been found that magnetization will always eventually fade out and gradually align with the applied magnetic field. The reason is that the precessional motion is with damping effect. As a result, another term should be added to Equation 2.2.5.

$$\frac{d\vec{M}}{dt} = -\mu_0 \gamma \vec{M} \times \vec{H}_0 + \frac{\alpha}{|\vec{M}|} \vec{M} \times \frac{d\vec{M}}{dt} \quad 2.2.17$$

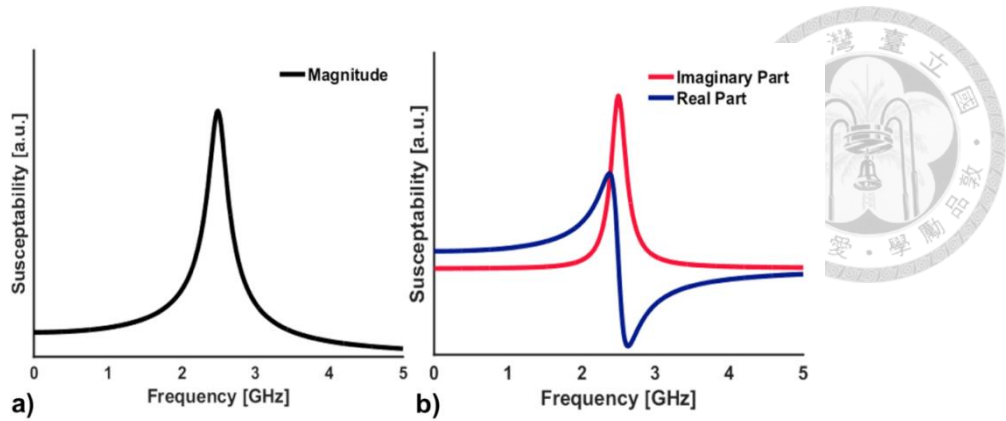


Fig. 2.11. Dynamic permeability in the vicinity of FMR (a) Magnitude of permeability. (b) Real and imaginary parts of the permeability [72].

and  $\omega_0$  is replaced by  $\omega_0 + j\alpha\omega$  to obtain susceptibility tensor. Here is  $\alpha$  the Gilbert damping coefficient. This is known as the Landau-Lifshitz-Gilbert (LLG) Equation and it completely describes the dynamics of a saturated magnetization in the presence of an external torque. At GHz frequencies, domain wall motion cannot follow fast enough to the applied torque [72]. As a result, the change in magnetization is mainly due to the external excitation. When the frequency of precession is close to the excitation frequency, the amplitude of the magnetization will greatly increase. This frequency is called the ferromagnetic resonance (FMR) frequency and is controlled by the external DC bias (Fig. 2.11).

For how to control magnetization through elasticity, there're more and more emerging works investigating magneto-elastic coupling and FMR absorption. For example, the experiment through SAW device to [73], [74] and [75] (Fig. 2.12) was conducted. It reveals that angle between the magnetization and the applied strain is a large factor in the magneto-elastic coupling, and shows that maximal coupling happens at an angle of  $40^\circ$  relative to the propagation direction (Fig. 2.13). In Fig. 2.13, it basically shows that there is indeed no coupling along the  $0^\circ$  and  $90^\circ$  directions. There has also been

some preliminary investigation on the magneto-elastic properties of bulk mode resonators [76]. Related research is still relatively new and in need of further study. Especially for elastodynamics, theoretical and experimental works are very recent compared to piezoelectric properties which are already commercialized successfully.

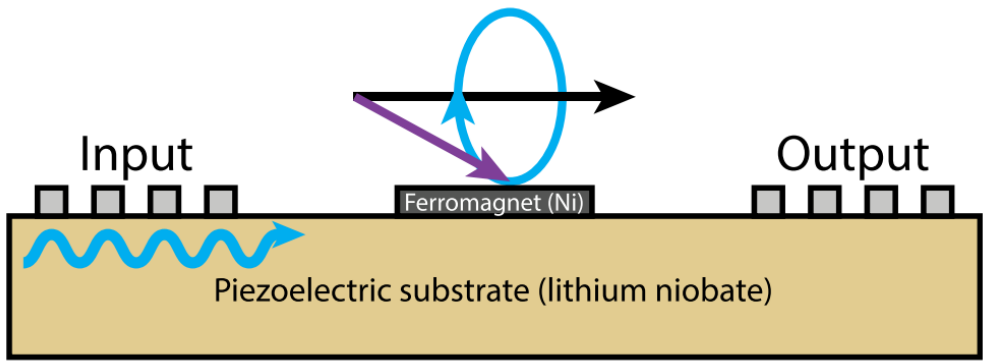
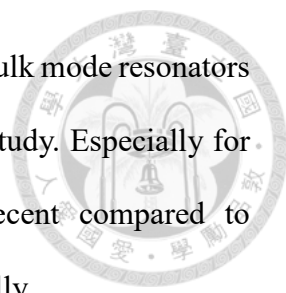


Fig. 2.12. SAWs are generated in a piezoelectric substrate by applying an AC voltage to the Input IDT [74].

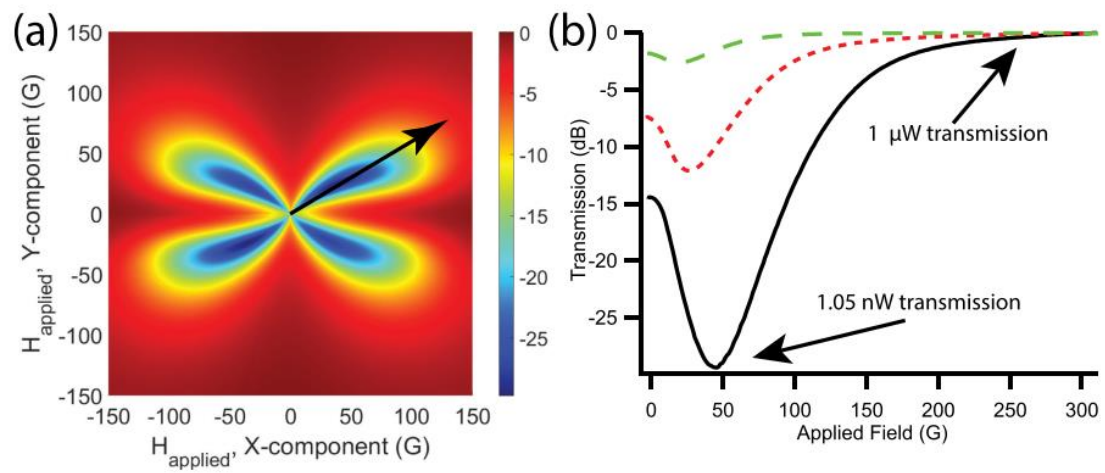
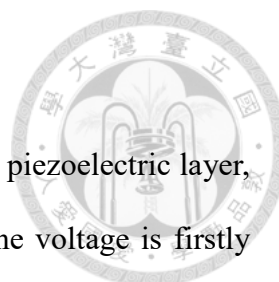


Fig. 2.13. (a) Plot of the absorption of SAW power by the magnetic element (in dB) as a function of applied x and y magnetic field at a SAW frequency of 1992 MHz (b) Line cut along the direction indicated by the black line in (a) at a number of different SAW frequencies (green, 857 MHz; red, 1424 MHz; and black, 1992 MHz). [74]



## 2.4 Device Operation Principle

The device is a three layer multiferroic laminate consisting of a piezoelectric layer, magneto-elastic layer, and a mechanical buffer layer (Fig. 2.14). The voltage is firstly applied to the piezoelectric layer which generates a strain wave. The strain wave will form the standing wave resonance. Hence at the suitable frequencies, these reflected waves interfere constructively and bulk acoustic wave resonance (BAWR) occurs. This is essentially the same mechanism behind thin-film bulk acoustic wave resonators (FBARs) used in cellular duplexers. What's difference is that there's one more mechanical buffer layer on top in order to shift highest amplitude of the strain wave into the center of the magneto-elastic layer to maximize coupling. As the wave passes through the magneto-elastic layer, the magnetization begins to oscillate. This dynamic magnetization will act to serve as the equivalent magnetic current source for the radiation.

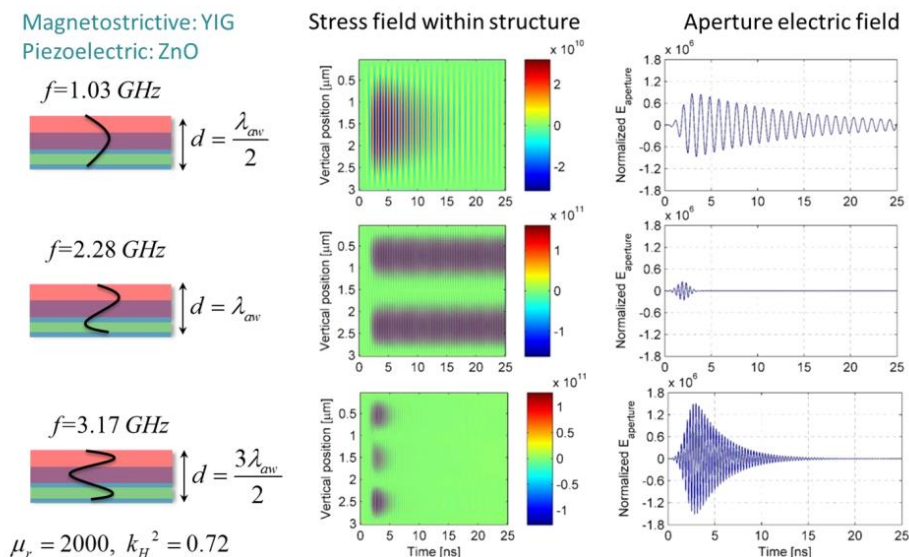


Fig. 2.14. FDTD modelling of proposed antenna structure by Zhi Yao et al. First column is the excited acoustic resonance mode. Middle column is the stress profile as a function of time. Last column is the radiated electric field [37].

In Zhi Yao's work, the structure was numerically modelled by 1D and 3D Finite-Difference Time Domain (FDTD) methods [35]-[40], providing preliminary validation to the concept. For this kind of multiphysics problem involved in multiferroic antennas, dynamic Maxwell's equations, Newton's law and Landau-Lifshitz-Gilbert (LLG) equation are required to be solved simultaneously:

$$\text{Dynamic Maxwell's equation} \quad \vec{\nabla} \times \vec{H} = \frac{\partial \vec{D}}{\partial t} + \sigma \vec{E}, \vec{\nabla} \times \vec{E} = -\frac{\partial \vec{B}}{\partial t} \quad 2.3.1$$

$$\text{Newton's law} \quad \nabla \cdot \vec{T} = \rho \frac{\partial \vec{v}}{\partial t}, \nabla_S \vec{v} = \frac{\partial \vec{S}}{\partial t} \quad 2.3.2$$

$$\text{Landau-Lifshitz-Gilbert (LLG)} \quad \frac{d\vec{M}}{dt} = -\mu_0 \gamma \vec{M} \times \vec{H}_0 + \frac{\alpha}{|\vec{M}|} \vec{M} \times \frac{d\vec{M}}{dt} \quad 2.3.3$$

Fig. 2.15 summarizes the results of these simulations. For the first and third modes, it is seen that the acoustic wave damps with time due to the energy loss to the electromagnetic radiation. One important observation is that the second one exhibits no damping of the acoustic wave and radiation. This is mainly because the node at the center of the structure giving a net zero strain across the magneto-elastic layer. Further analysis has been done incorporating the dynamics of the LLG equation in [39]. The model mentioned above essentially shows that FMR driven acoustically can lead to radiation in addition to BAWR. We can also observe that the location of the BAWR is seen to also be

bias dependent as the FMR frequency approaches it.

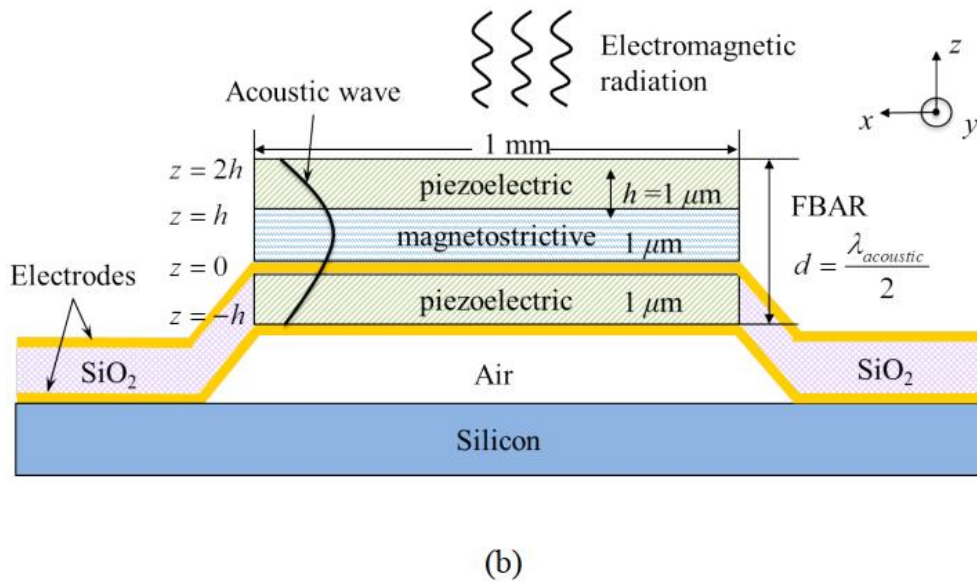
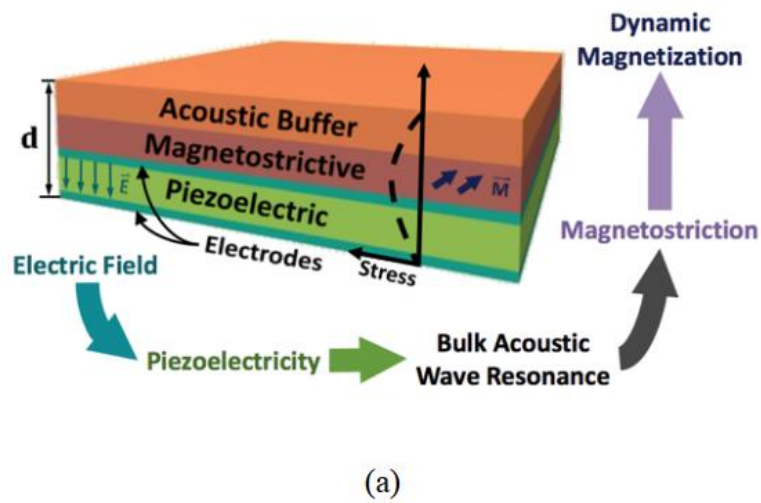


Fig. 2.15. BAW resonance based antenna. (a) Structure and physical coupling mechanism. (b) Cross section of the antenna. Electric current excitation is applied to the electrodes to drive bottom piezoelectric layer, and the standing wave resonance further triggers the magnetostrictive layer as the equivalent magnetic current source of radiation [37].



# Chapter 3    **Circularly-polarized    BAW    Multiferroic**

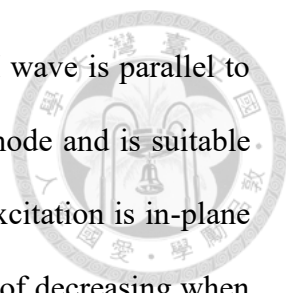
## **Antenna**



### **3.1    Circular Polarization Control of Bulk-Acoustic Wave Mediated Antenna Using Lateral Field Excitation**

As mentioned before, the fundamental principle behind BAW multiferroic antenna is the coupling between elastodynamics and electrodynamic. External AC voltage is applied upon piezoelectric material, thus creating a resonant longitudinal stress field across the device. The core part of in this work is that we come up with a new idea to achieve polarization control of BAW-mediated multiferroic antennas. Polarization is a fundamental characteristic of antenna design. There are many researches regarding design of circular polarized antennas. The benefits of circular polarization system include enhancement of signal quality and communication system channel capacity as well as easy installation of systems (Fig. 3.1) [77].

In the past ten years, FBARs have been applied widely in high frequency filters and sensors. The device is operated in the longitudinal mode typically. However, for the application of mass-loading sensors in liquids, thickness-shear-modes (TSM) have better quality factor than longitudinal modes. Hence, there have been increasing researches studying thickness-shear-modes of FBARs (Fig. 3.2 and Fig. 3.4) [78]. In [37], longitudinal bulk acoustic wave is excited in order to induce magnetic current. However, there is only one dimension of longitudinal bulk acoustic wave, which means that it cannot be used to create circular polarization. According to [79], “the thickness shear mode (TSM) acoustic wave is another possible propagating mode in the piezoelectric film



along the thickness direction. The particle displacement of the TSM wave is parallel to the film surface.” Hence, TSM wave has two orthogonal in-plane mode and is suitable for generating circular polarization. In addition, since shear mode excitation is in-plane structure, it can be further expected to increase the radiation instead of decreasing when placed above the electric conductor due to the unidirectional image magnetic current (see Fig. 3.3). This is an additional improvement compare to the longitudinal one used before. There are a couple of ways to excite TSM. For example, interdigitated electrodes (IDE) and lateral electrodes are both studied before [78], [79] and [80]. Due to the practical consideration, lateral excitation is favorable for its design simplicity [79]. With the lateral field excitation of TSM mode in BAW-mediated multiferroic antennas, one can switch to different polarization modes straightforwardly with the adjustment of applied control voltage. In this work, the simulated axial ratio and radiation pattern of far-field radiation is obtained with the numerical model constructed by COMSOL and MATLAB, which

validates the possibility for practical fabrication.

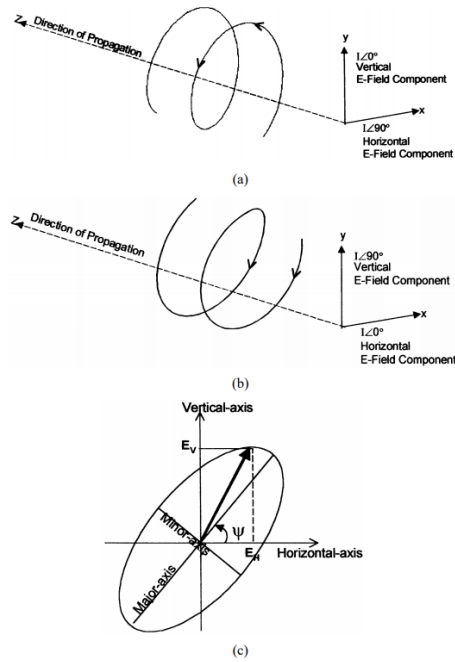


Fig. 3.1. (a) Left-hand circular polarization. (b) Right-hand circular polarization. (c) Polarization ellipse [77].

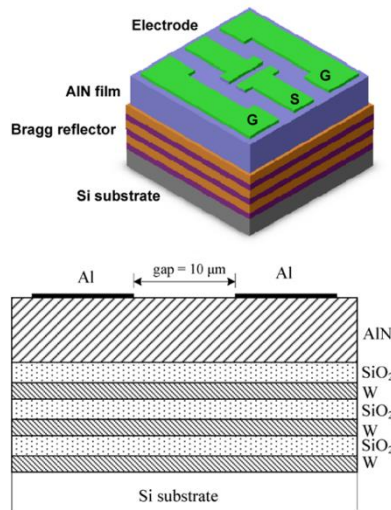


Fig. 3.2. The sketch of the AlN-based solidly mounted resonator operated in thickness shear mode waves [79]

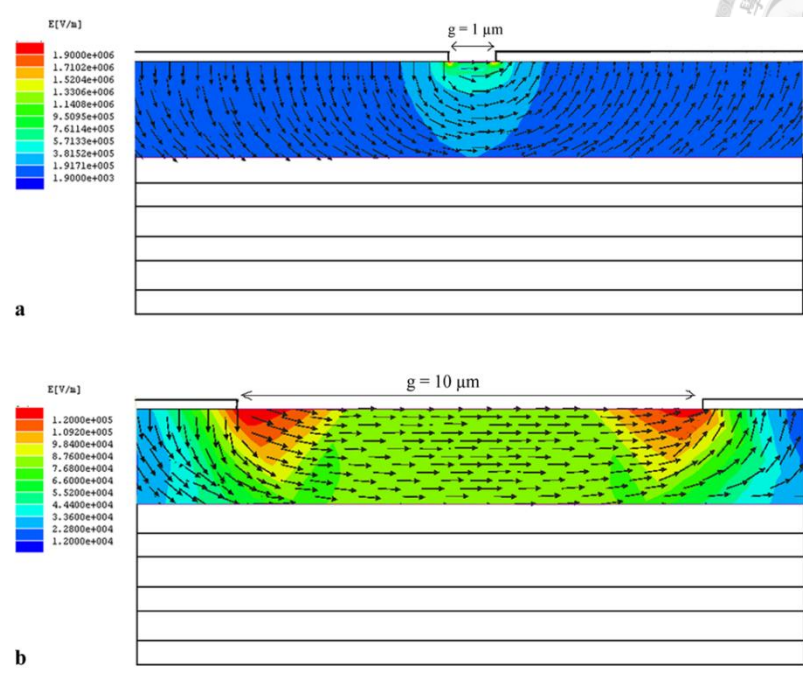
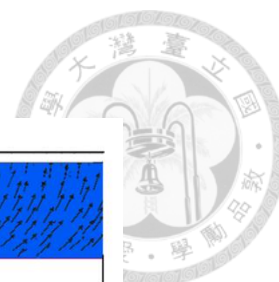


Fig. 3.4. The finite element simulation of the electric field generated by the simple electrode geometries with the gaps of (a) 1 and (b) 10  $\mu\text{m}$  [79]

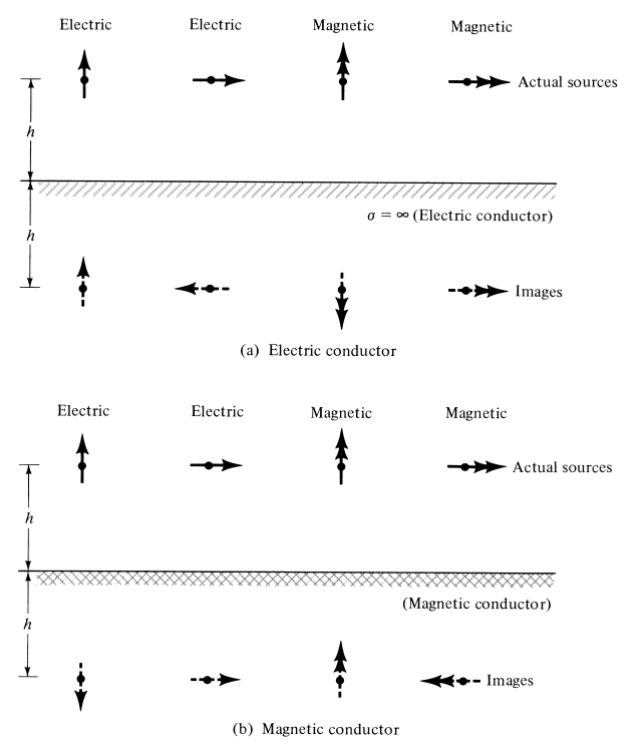
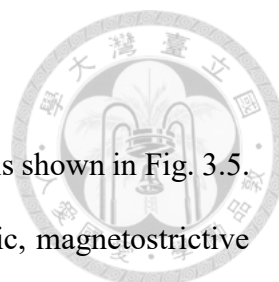


Fig. 3.3. Electric and magnetic sources and their images near electric (PEC) and magnetic (PMC) conductors [25].



## 3.2 Numerical modelling

The simulated structure of BAW-mediated multiferroic antenna is shown in Fig. 3.5. There are three layers of laminated materials, which are piezoelectric, magnetostrictive and acoustic buffer materials respectively. Piezoelectric materials transform AC voltage signal into resonant mechanical stress fields. Then, mechanical stress fields cause oscillating magnetization inside magnetostrictive material, creating electromagnetic radiation. In our work, stress field is induced through lateral electrodes. As shown in Fig. 3.6, two set of electrodes are placed at the bottom instead of top and bottom sides of the device. If we apply AC voltage with 90-degree phase differences on these two sets of electrodes, they will create circular polarized shear wave propagating along z-axis, forcing circular polarized magnetization inside magnetostrictive materials. Circular polarized magnetization acts as circular polarized magnetic current, which is the source of circular polarized radiation.

According to the analysis of [79], the existence of TSM wave from lateral field

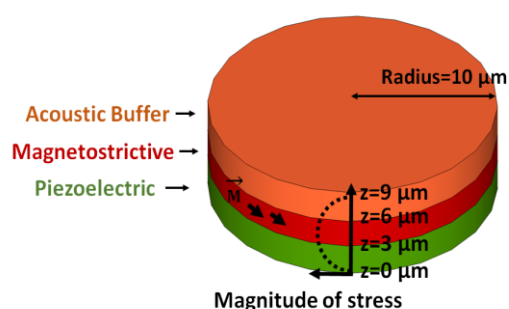


Fig. 3.5. Simulated structure of BAW-mediated multiferroic antenna.  $\bar{M}$  represents magnetization inside magnetostrictive layer.

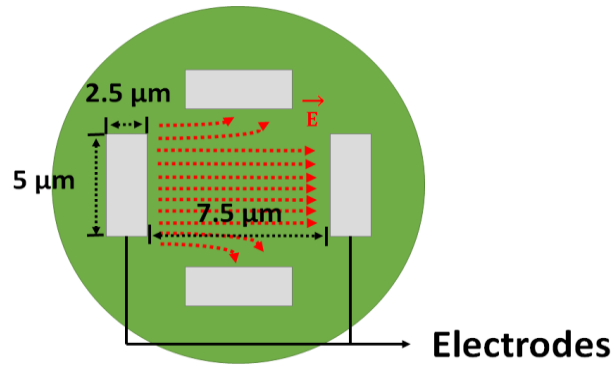


Fig. 3.6. Two sets of lateral electrodes are placed at the bottom of BAW-mediated multiferroic antenna. Each set of electrode includes a terminal connected to ground and a terminal connected to voltage source. The spacing between two terminals of one set of electrodes is 10 ( $\mu\text{m}$ ). The thickness of electrodes is 0.1 ( $\mu\text{m}$ ). External voltage sources with 90-degree phase differences are applied upon each set of electrodes and thus creates circular polarized electric field at the bottom.

excitation can be verified by solving the Christoffel equation. The acoustic velocity for the lateral field excitation of thickness shear mode of aluminum nitride is given by

$$v_s = \sqrt{\frac{c_{44} + e_{15}^2/\epsilon_{11}}{\rho}} \quad 3.2.1$$

, where  $c_{44}$  is component of the stiffness tensor,  $e_{15}$  is component of the piezoelectric coupling tensor,  $\epsilon_{11}$  is component of the permittivity tensor and  $\rho$  is volume density. According to [79], the theoretical wave speed is 6333 m/s. For the resonant frequency 2.5 GHz at fundamental mode, the thickness of piezoelectric is around 1 ( $\mu\text{m}$ ), which is much thinner than patch antenna.

Furthermore, as shown in [80], if the TSM wave is propagating in the direction 3, we can know that stress tensor component  $T_{xz}$  is generated directly from excitation of direction 1, while  $T_{yz}$  is from excitation of direction 2. When 90-degree phase differences

are imposed upon  $T_{xz}$  and  $T_{yz}$ , two orthogonal TSM wave will thus form circular polarized shear stress field. Since Ni and buffer material are both isotropic materials, this circular polarized shear acoustic wave will form standing wave in the z-axis with sinusoidal distribution. From the previous part, we know that there exist a circular polarized stress field across the device. Here dynamic stress is assumed to be linearly proportional to dynamic magnetization, which represents a thin layer of effective magnetic current. Although magnetostriction is mainly a non-linear effect [81], as long as the oscillating magnetization caused by the stress field is much smaller than saturation magnetostriction, it's reasonable to adopt the assumption.

In order to simplify the cases, we assume that the magnetic current is in free space for the far-field calculation. Using the far-field mapping based on magnetic source, we know that

$$\bar{F} = \frac{\varepsilon}{4\pi} \iiint_V \bar{M}(x', y', z') \frac{e^{-jkR}}{R} dv' \quad 3.2.2$$

$$\bar{E}_F = -\frac{1}{\varepsilon} \nabla \times \bar{F} \quad 3.2.3$$

$$\bar{H}_F = -j\omega \bar{F} - j \frac{1}{\omega\mu\varepsilon} \nabla(\nabla \cdot \bar{F}) \quad 3.2.4$$

, where  $\bar{F}$  represents electric potential and  $\bar{M}$  represents magnetic sources.  $\bar{E}_F$  and  $\bar{H}_F$  represent far-field electric and magnetic field respectively. Transforming the above relations into spherical coordinate, we have

$$\bar{E}_F = jk(\hat{r} \times \bar{F}_T) = jk(\hat{\theta}F_\phi + \hat{\phi}F_\theta) \quad 3.2.5$$

$$\bar{H}_F = -j\omega\varepsilon_0 \bar{F}_T = -j\omega\varepsilon_0(\hat{\theta}F_\theta + \hat{\phi}F_\phi) \quad 3.2.6$$

, where  $\bar{F}_T$  is defined by  $\hat{\theta}F_\theta + \hat{\phi}F_\phi$ . As for the calculation of axial ratio, the electric field of major and minor axis can be defined by 3.2.7 and 3.2.7 respectively according to

[25]

$$\text{Major axis: } \left[ \frac{1}{2} \left\{ E_{\theta}^2 + E_{\phi}^2 + [E_{\theta}^4 + E_{\phi}^4 + 2E_{\theta}^2 E_{\phi}^2 \cos(2\Delta\phi)]^{\frac{1}{2}} \right\} \right]^{\frac{1}{2}} \quad 3.2.7$$

$$\text{Minor axis: } \left[ \frac{1}{2} \left\{ E_{\theta}^2 + E_{\phi}^2 - [E_{\theta}^4 + E_{\phi}^4 + 2E_{\theta}^2 E_{\phi}^2 \cos(2\Delta\phi)]^{\frac{1}{2}} \right\} \right]^{\frac{1}{2}} \quad 3.2.8$$

, where  $\Delta\phi = \phi_{\phi} - \phi_{\theta}$ . Using the formula 3.2.7 and 3.2.8, the desired axial ratio is defined as

$$\text{AR} = \frac{\text{major axis}}{\text{minor axis}}, 1 \leq \text{AR} \leq \infty. \quad 3.2.9$$





### 3.3 Results and Analysis

Flow chart of numerical modelling is shown in Fig. 3.7. In [37], 1D FDTD numerical modelling is built to verify the feasibility of BAW-mediated multiferroic antennas. However, if we want to simulate 3D full coupling between electrodynamics and elastodynamics, it will take too much time and is likely to run out of memory. Hence, our model is based on weak-coupling assumption, which separates the coupling relation between magnetization and stress. The model is separated into three stages. First stage is piezoelectric stage, which transforms AC voltage into resonant stress field. Second stage is the magnetostrictive stage, which transforms resonant stress field into oscillating magnetic current. Third stage is radiating stage, which transforms oscillating magnetic current into far-field radiation. The following sections will specify simulation procedure and show the calculated results.

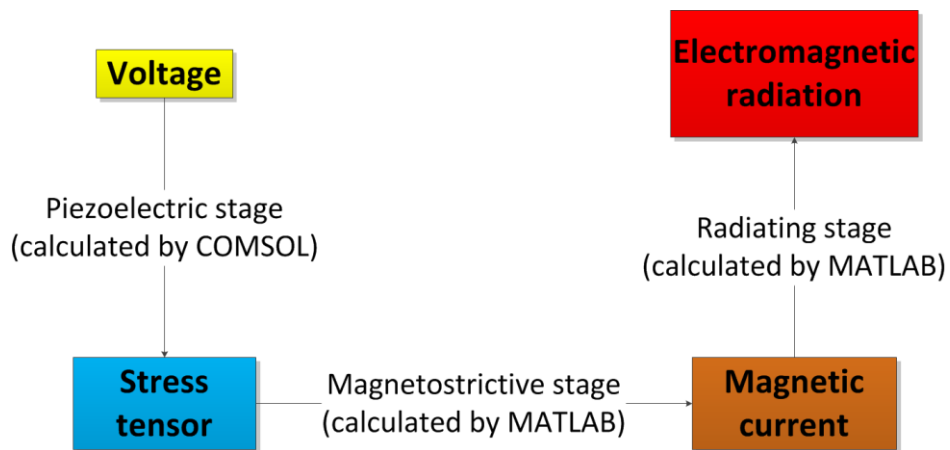


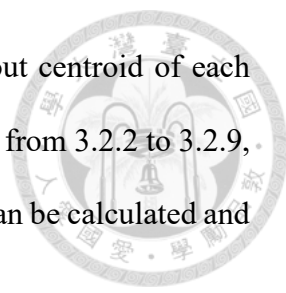
Fig. 3.7. Flow chart of numerical modelling.

COMSOL is a finite element solver and multi-physics software. It provides convenient workflows for users to simulate electrical, mechanical, fluid and chemical phenomenon. We choose COMSOL to simulate acoustic mechanical resonance across BAW-mediated multiferroic antenna. The coupling between stress and electric field is calculated simultaneously. Using COMSOL, we can identify Eigen-modes of TSM first. Table 2. specifies basic information about simulation environment setup. In Fig. 3.3.2, circular motion of BAW-mediated multiferroic device is demonstrated. In order to demonstrate the circular motion more clearly, height of each layer in Fig. 3.3.2 is assigned to be 3  $\mu\text{m}$  instead of 0.3  $\mu\text{m}$ . The characteristic of far-field axial ratio between them is very similar. As shown in Fig. 3.8, the circular displacement induced by bottom electrodes act effectively at frequency of 250 MHz.

Stress tensor  $T_{xz}$  and  $T_{yz}$  from first stage of each simulated frequency are extracted into MATLAB. Magnetic current is assumed to be linearly proportional to stress. Because

Layer	Materials	Study	Applied voltage	Boundary condition (all side faces are free boundaries)
Electrodes	Platinum	Electrostatics	Set 1: 1 (volt) 、 Set 2: 1i (volt)	Top: attached Bottom: free
Piezoelectric	Aluminum Nitride	Piezoelectric Effect	N/A	Top: attached Bottom: free
Magnetotrophic	Nickel	Solid mechanics	N/A	Top: attached Bottom: attached
Acoustic buffer	Silicon Nitride	Solid mechanics	N/A	Top: free Bottom: attached

Table 3. Basic parameters of COMSOL simulation



COMSOL calculation is based on mesh analysis, we need to find out centroid of each tetrahedral element and its value of magnetic current. Using relations from 3.2.2 to 3.2.9, far-field radiated pattern and axial ratio versus different frequencies can be calculated and plotted.

Stress tensor of  $T_{xz}$  and  $T_{yz}$  is shown in Fig. 3.9. We can observe that magnitude of  $T_{xz}$  and  $T_{yz}$  is close to sinusoidal distribution. Due to the free boundary condition of at  $Z=0$  ( $\mu\text{m}$ ) and  $Z=0.9$  ( $\mu\text{m}$ ), it's reasonable to see the sinusoidal distribution of stress. Besides, magnitude of  $T_{xz}$  and  $T_{yz}$  between  $Z=0.3$  ( $\mu\text{m}$ ) and  $Z=0.6$  ( $\mu\text{m}$ ) is pretty close, while phase differences are close to  $\pi/2$ . This is the main source of circular polarization radiation. As for broadside axial ratio versus frequency, it is plotted in Fig. 3.11. The 3dB

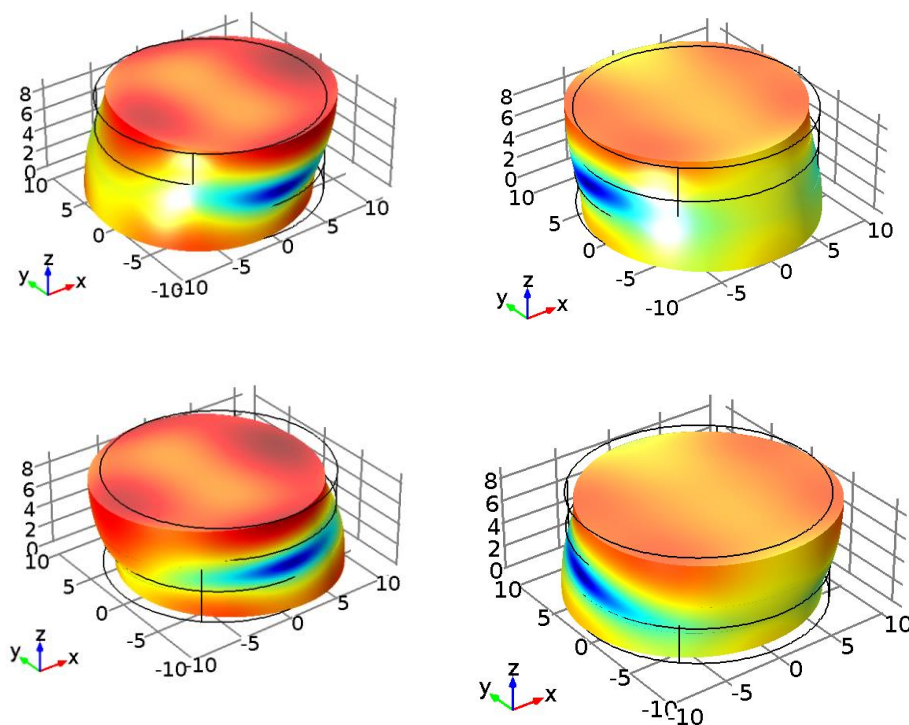
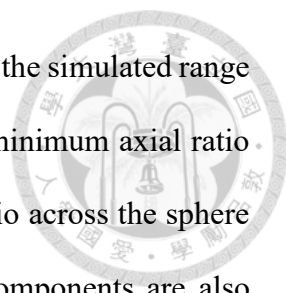


Fig. 3.8. Snapshots of displacement animation operated at 250 MHz (length units in  $\mu\text{m}$ ). (Left-top)  $t=T/4$ ; (Right-top)  $t=T/2$ ; (Left-bottom)  $t=3T/4$ ; (Right-bottom)  $t=T$ . Counter-clockwise circular polarized (from top's view) displacement can be observed clearly.



bandwidth of axial ratio is exceptionally broad. It almost covers all of the simulated range except some of the ranges of high band. Using the frequency with minimum axial ratio within the simulated frequency range, radiation pattern and axial ratio across the sphere can also be obtained. X-Z and Y-Z plane cut of two orthogonal components are also plotted in Fig. 3.10. For the spikes with high axial ratio, each eigen-modes are examined separately from Fig. 3.12 to Fig. 3.21. It's shown that indeed at these frequencies there are unwanted modes excited instead of the 2 in-plane orthogonal thickness shear modes designed originally. However due to fabrication limits, the thickness of the device can only be stacked to  $1.1\mu\text{m}$  with the radius of  $200/500/1000\mu\text{m}$ , instead of thickness of  $9\mu\text{m}$  and radius of  $10\mu\text{m}$  simulated before. Hence, two cases are simulated here. We can expect that if the thickness is comparable to the radius, the displacement of thickness shear mode will be easier to observed in the simulation. The radius of  $1\mu\text{m}$  and  $10\mu\text{m}$  are simulated and the result is shown in Fig. 3.23 to Fig. 3.24. It's found that the axial ratio still possess broadband response under around 2GHz, which is related to the thickness. However, in the case of  $1\mu\text{m}$ , the mesh is more dense and the phase distribution is clear while in the case of  $10\mu\text{m}$  the mesh is not enough. For the case of  $200/500/1000\mu\text{m}$ , they are all simulated and face the similar problem in the case of  $10\mu\text{m}$ . The other difficulty is that the frequency of most ideal response is by looking at the displacement characteristic. However, for the larger radius one the mode itself is often complicated and hard to recognize. Hence, even if the axial ratio still possess the same characteristics, the stress distribution itself is relatively random and cannot be used to explain well compared to the originally simulated case. The better systematic way of selecting the most ideal one is needed rather than directly looking at the mode shape itself.

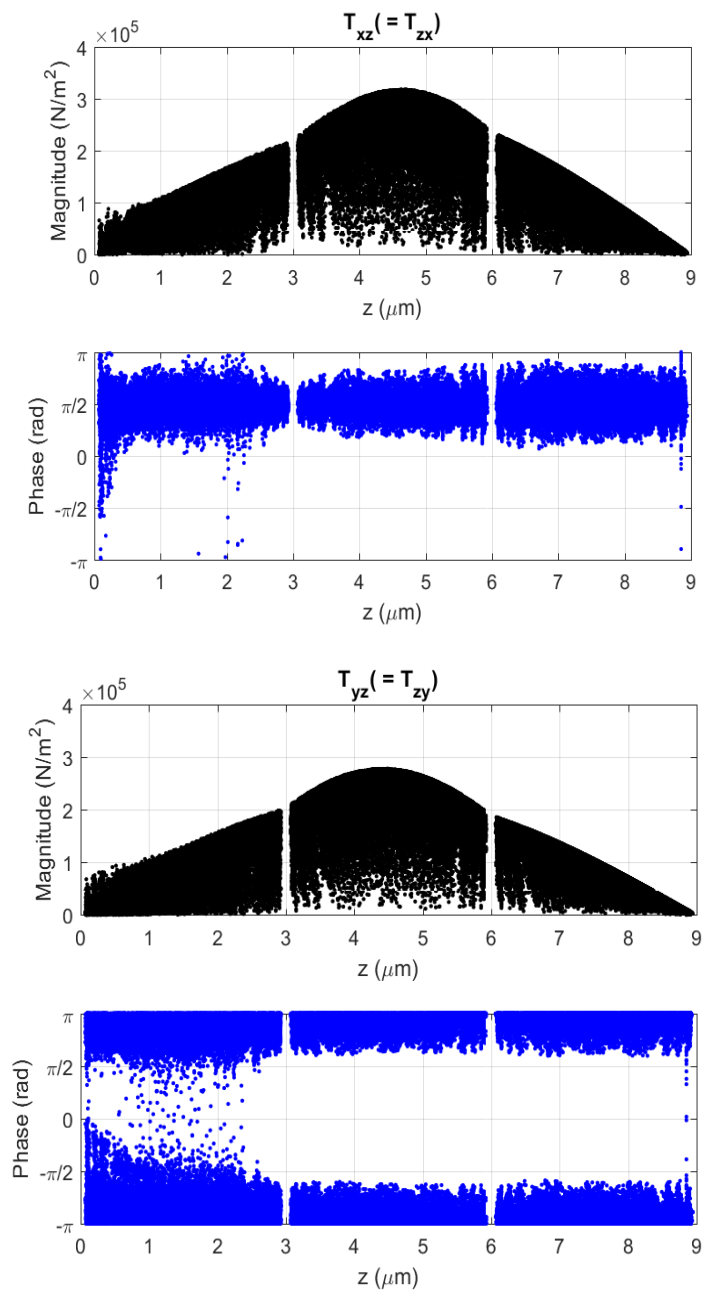


Fig. 3.9. Magnitude and phase distribution across  $z$  axis of stress tensor (a) Left:  $T_{xz}$  and (b) Right:  $T_{yz}$  inside the device.

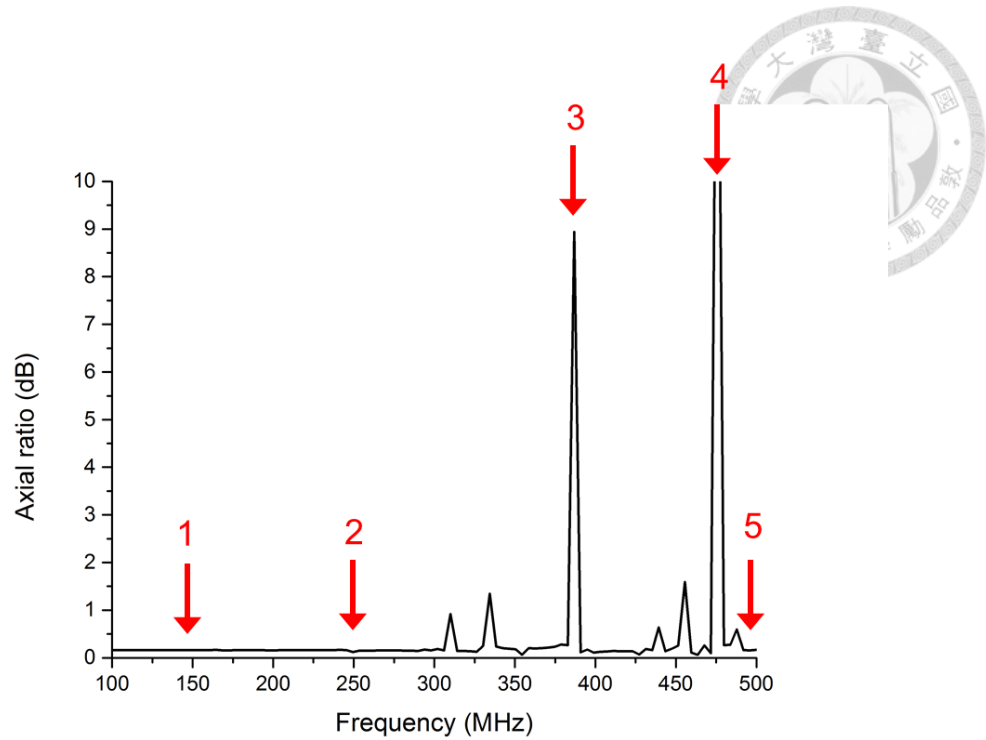


Fig. 3.11. Broadside axial ratio versus frequency between 100MHz and 500MHz.

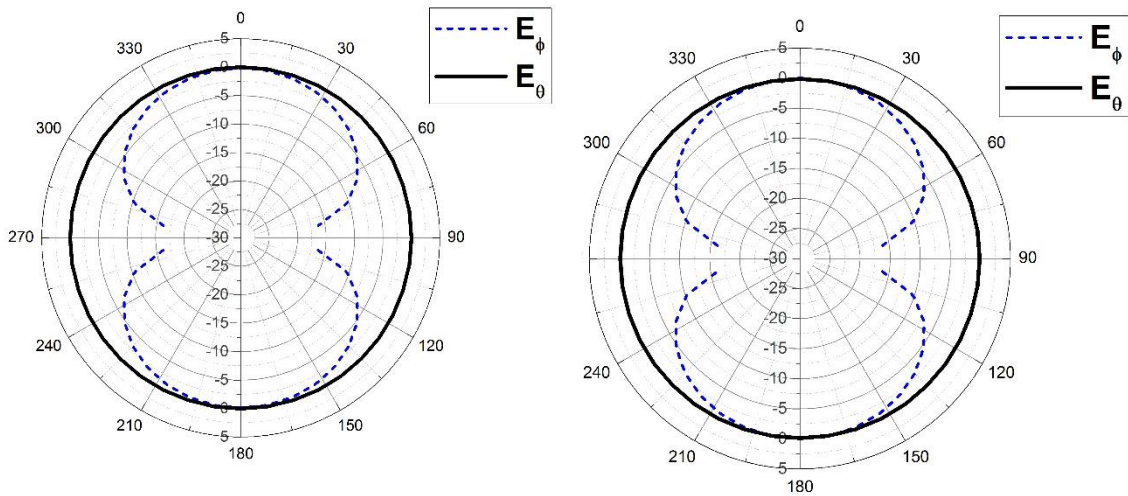


Fig. 3.10. (a) X-Z cut radiation pattern; (b) Y-Z cut radiation pattern. Radiation pattern of circular polarized BAW-mediated multiferroic antennas. This calculated radiation pattern is selected to be the frequency with lowest axial ratio within simulated frequency range.

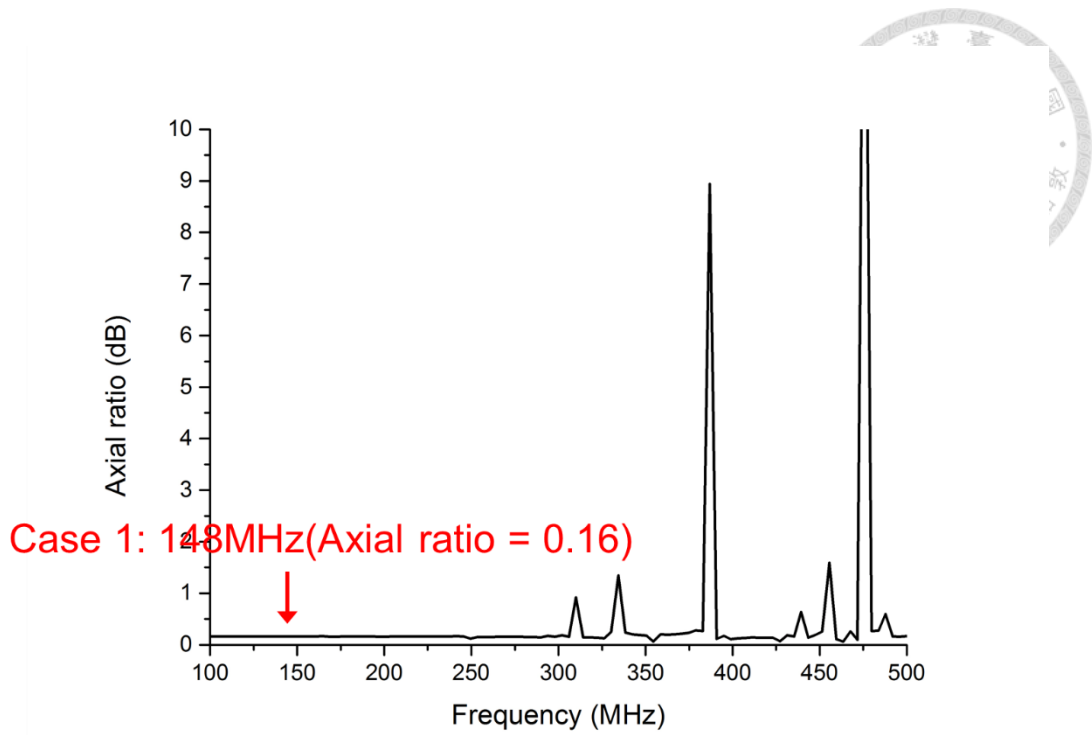


Fig. 3.13. Resonant mode 1 at 148MHz with axial ratio = 0.16.

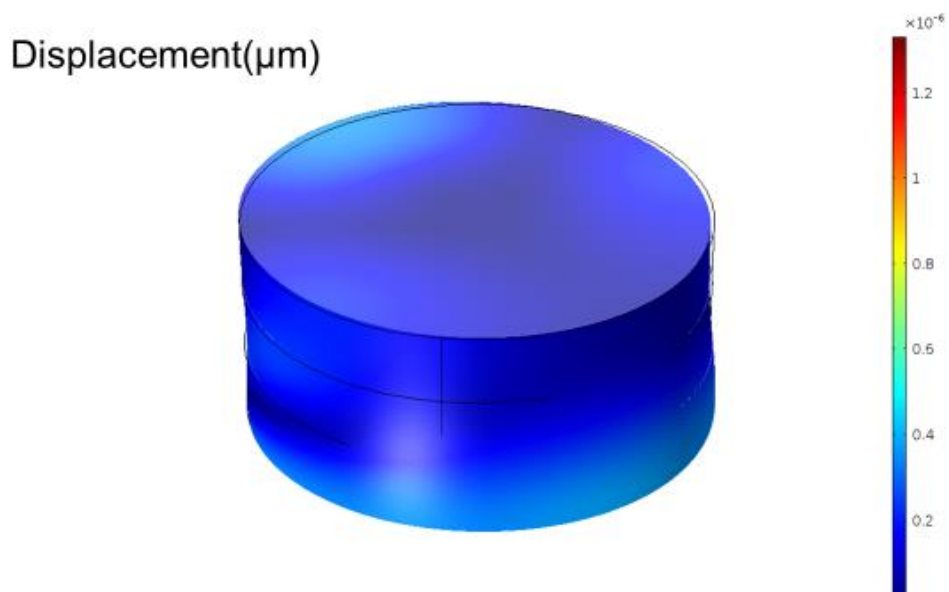


Fig. 3.12. Resonant mode 1 at 148MHz with axial ratio = 0.16. It is identified as weak fundamental thickness modes.

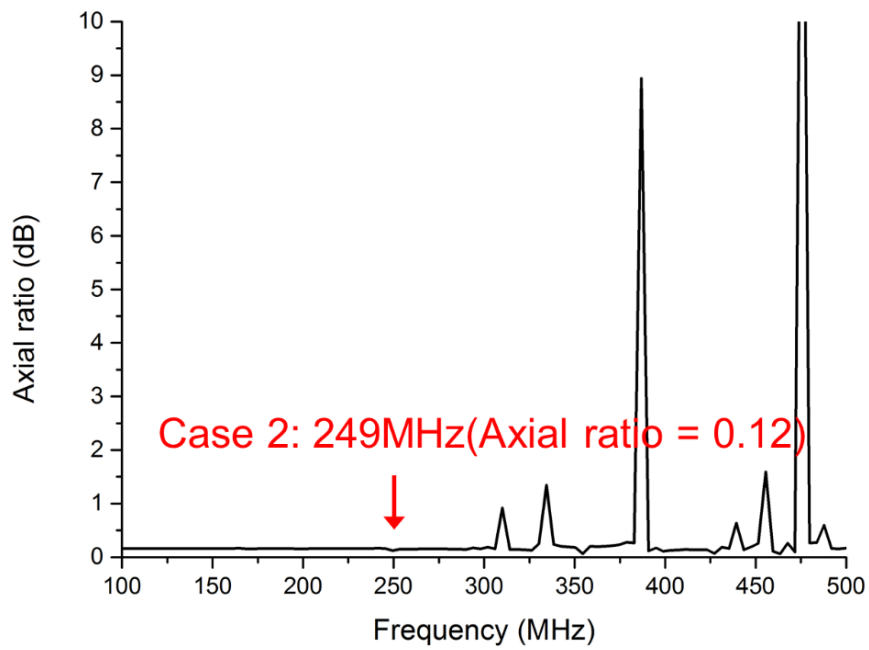


Fig. 3.14. resonant mode 2 at 249MHz with axial ratio = 0.12.

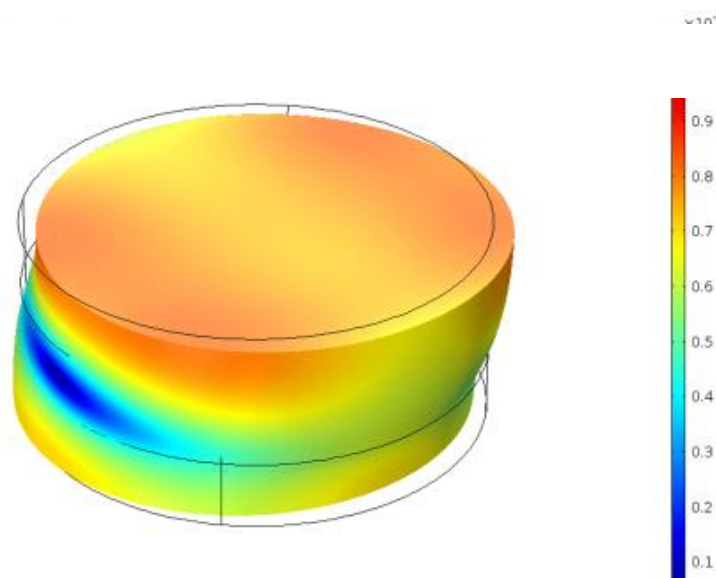


Fig. 3.15. Resonant mode 2 at 249MHz with axial ratio = 0.12. It is identified as main desired fundamental thickness shear modes.



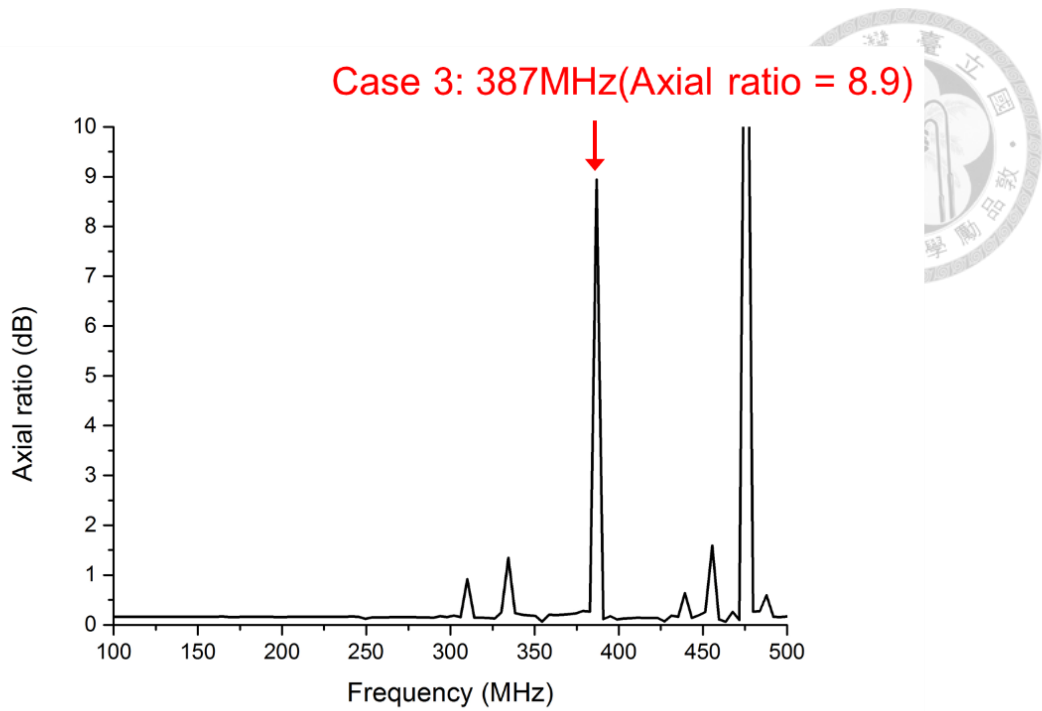


Fig. 3.16. Resonant mode 3 at 387MHz with axial ratio = 8.9.

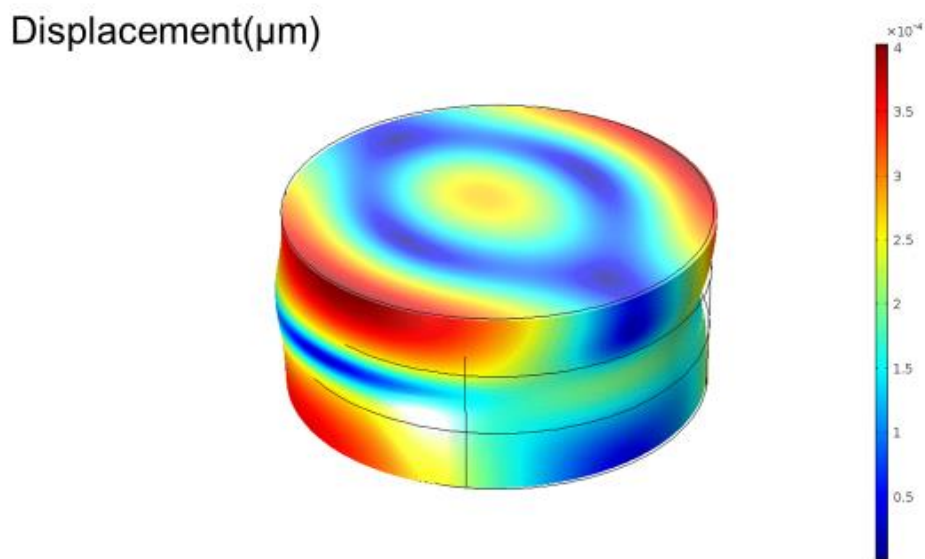


Fig. 3.17. Resonant mode 3 at 387MHz with axial ratio = 8.9. It is identified as the excitation of undesired mode.

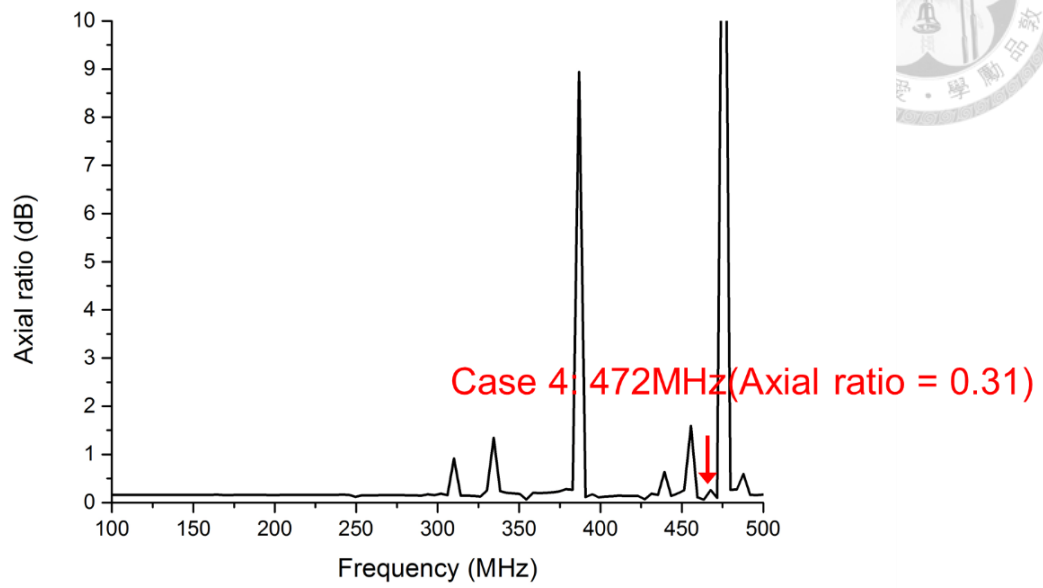


Fig. 3.18. Resonant mode 4 at 472MHz with axial ratio = 0.31.

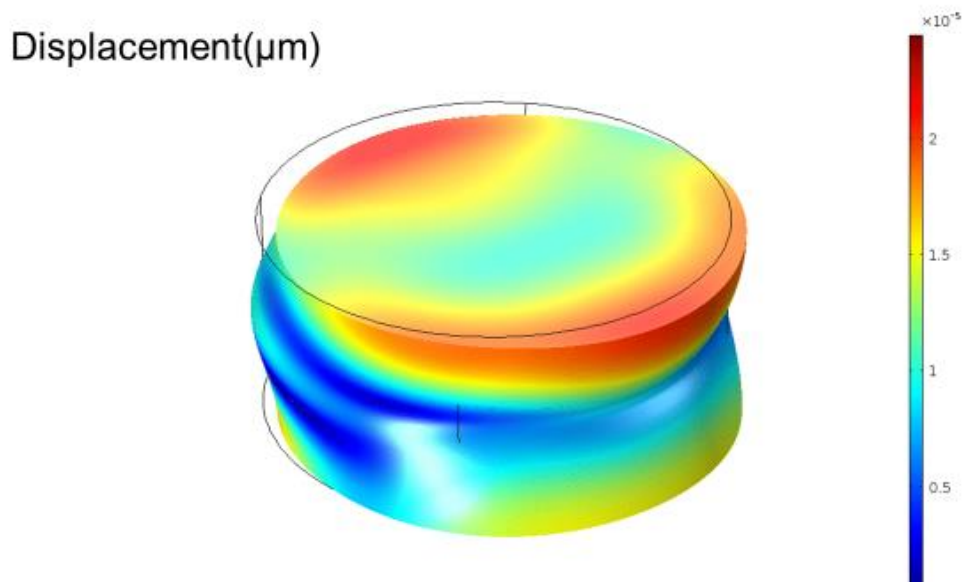


Fig. 3.19. Resonant mode 4 at 472MHz with axial ratio = 0.31. It is identified as the second order of thickness shear mode.

Displacement( $\mu\text{m}$ )

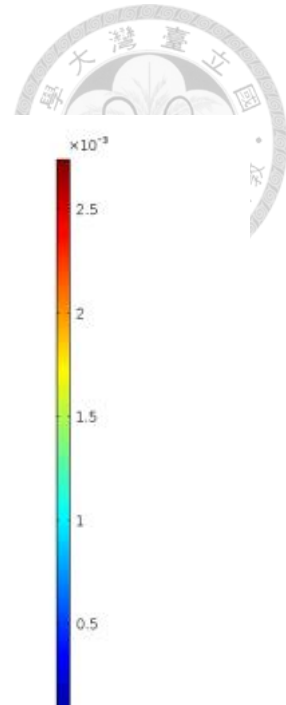
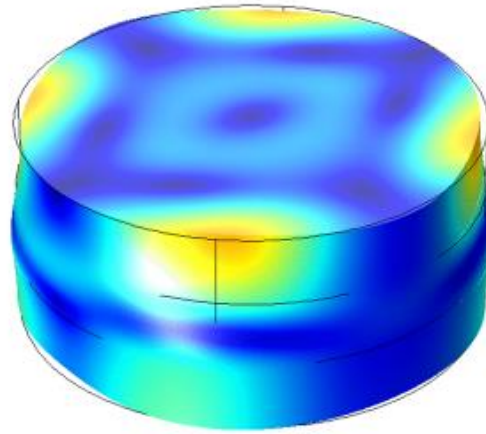


Fig. 3.21. Resonant mode 5 at 476MHz with axial ratio = 10.6. It is identified as the excitation of undesired mode.

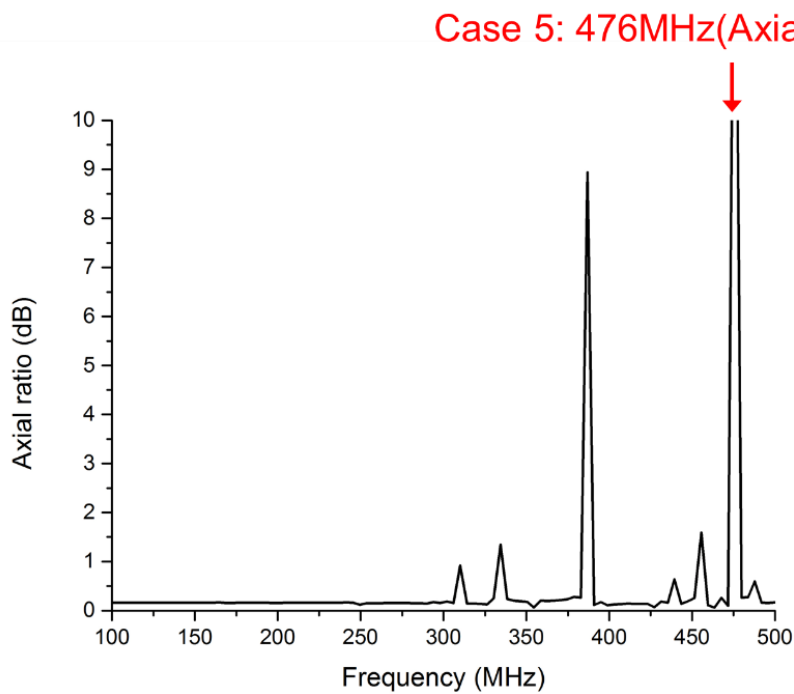


Fig. 3.20. Resonant mode 5 at 476MHz with axial ratio = 10.6.

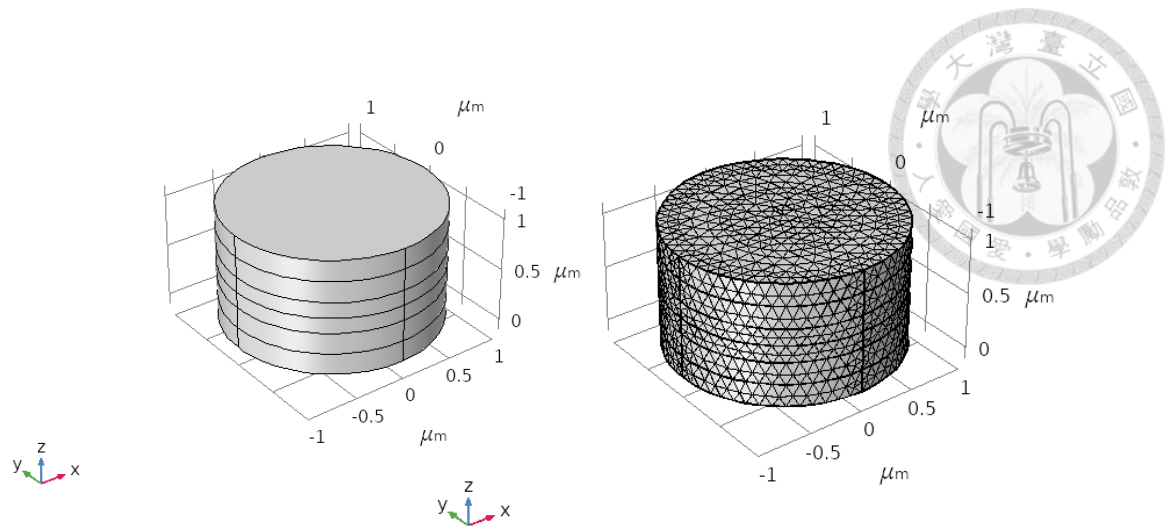


Fig. 3.23. Simulated structure of thickness of  $1.1\ \mu\text{m}$  and radius of  $1\ \mu\text{m}$ .

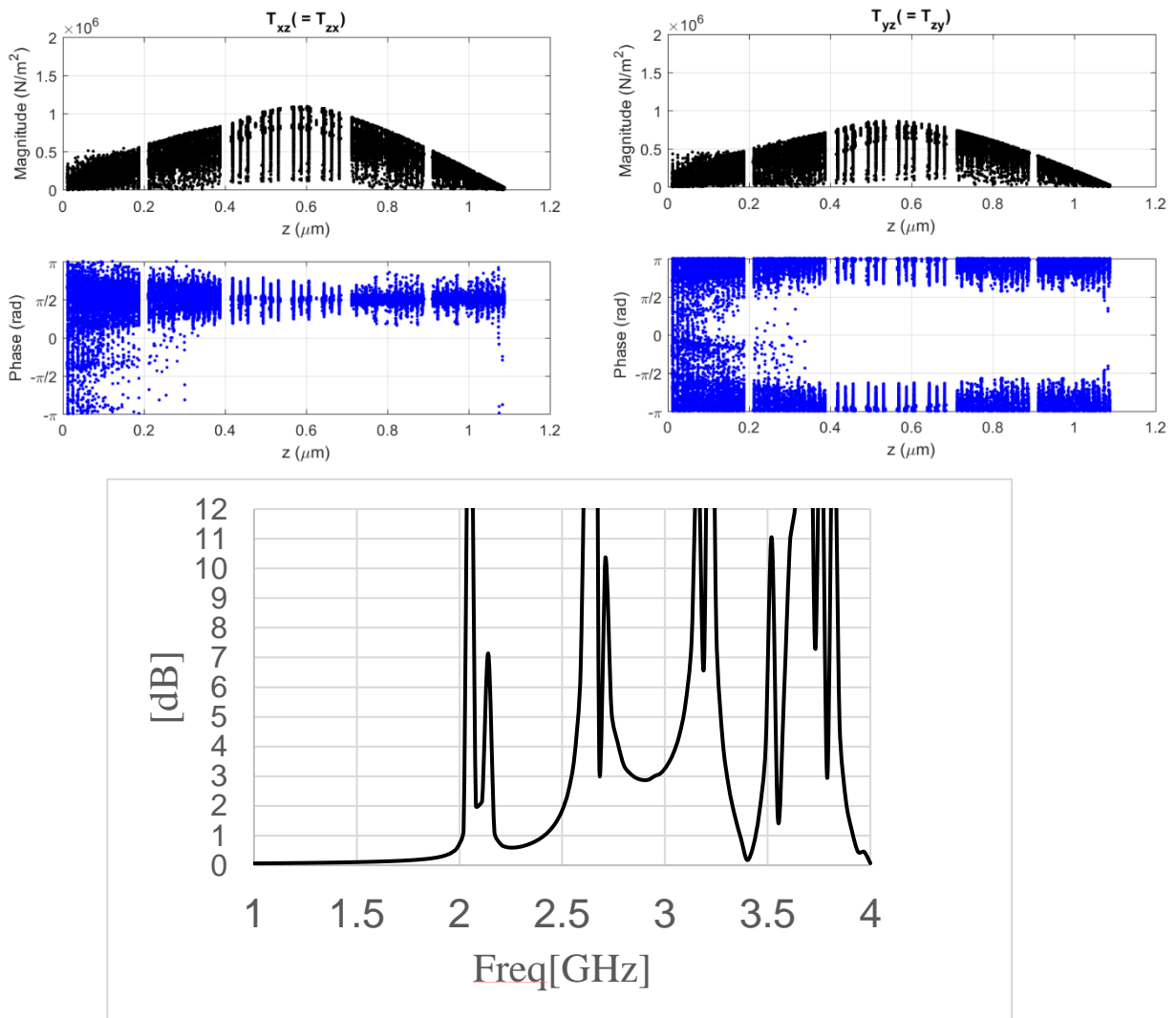


Fig. 3.22. The magnitude and phase distribution along  $z$  axis of radius of  $1\ \mu\text{m}$ . The axial ratio of frequency responses is also shown.

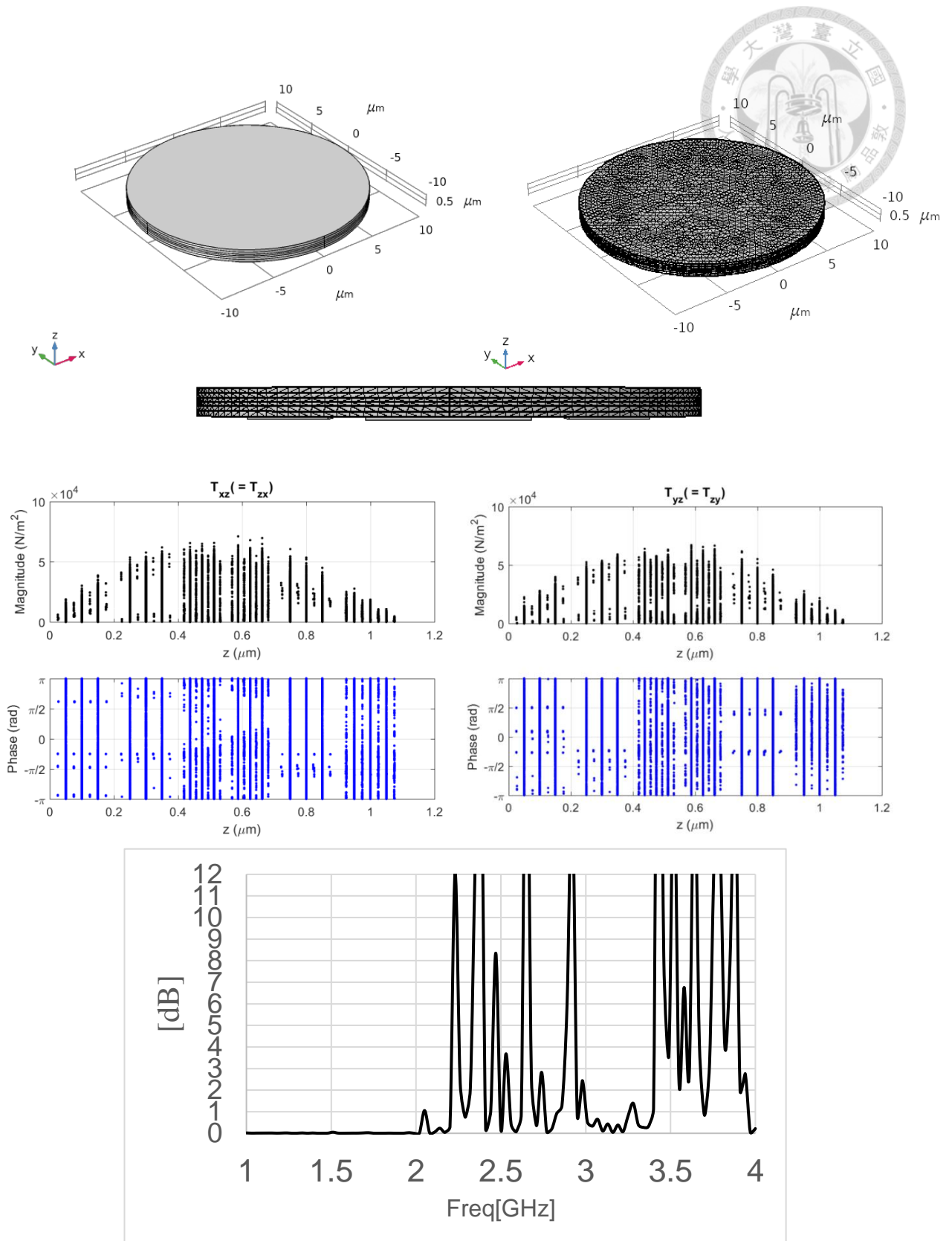


Fig. 3.24. The magnitude and phase distribution along  $z$  axis of radius of  $10\ \mu\text{m}$ . The axial ratio of frequency responses is also shown.

# Chapter 4 Measurement results



## 4.1 Device fabrication and design

The device fabrication is done by Sidant Tiwari at Sensors and Technology Laboratory of UCLA. The fabrication process is showed in Fig. 4.1 and its corresponding layer details are listed in Table 4. Fabrication process of BAW antenna for each layer and action.. Due to practical fabrication consideration, the radius changes into 200/500/1000  $\mu\text{m}$  instead of 9  $\mu\text{m}$  simulated in chapter 3. In addition to three versions of radius fabricated, there's also a version of NiFe in replacement of Ni. NiFe has very well-known properties and it possess no magneto-elastic properties. Hence it is used for reference measurements in order to compare whether there's radiation or not.

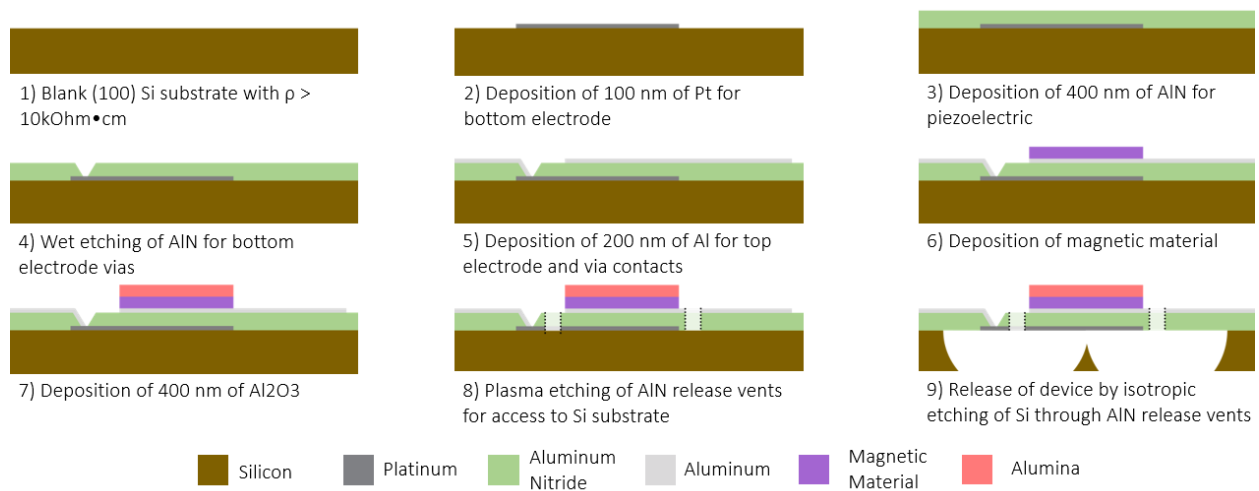


Fig. 4.1. Fabrication process of BAW antenna [72].

Table 4. Fabrication process of BAW antenna for each layer and action.

Layer number	Name	Corresponding step	Action in fab
0	Si substrate	1	Blank Si substrate
1	Pt bottom electrode	2	100 nm Pt for bottom electrode
2	AlN piezoelectric	3	400 nm AlN piezoelectric
3	Al via	4	Wet etching of AlN for bottom electrode vias
4	Ni magnetic material/NiFe non-magnetic testing material	6	300 nm Ni magnetic material/200 nm NiFe non-magnetic testing material
5	Alumina buffer material	7	400 nm Al <sub>2</sub> O <sub>3</sub>
6	Al top electrode	5	200 nm Al top electrode
7	Release vents inside resonator	8, 9	1300 nm(thickness of bottom electrode, piezoelectric, magnetic material and alumina) plasma etching + isotropic etching for release vents
8	Release vents outside resonator	8, 9	700 nm(thickness of bottom electrode, piezoelectric, and alumina) plasma etching + isotropic etching for release vents

The layouts of three fabricated versions of CP BAW antennas are shown in Fig. 4.2, Fig. 4.3 and Fig. 4.4. The holes onto the BAW disk are preserved to be release vents so that the device can do the isotropic etching. The release vents need to keep in certain distance with each other according to the design rule provided by Sidhant. Hence, there are more holes on the device for the larger radius one. In order to achieve and validate the concept polarization control, a CPW-Slot-CPW wideband branch-line coupler is designed based on [93]. Theoretical resonant frequency of fundamental thickness shear mode is around 2GHz. Wideband characteristics mean to validate the broadband feature of axial

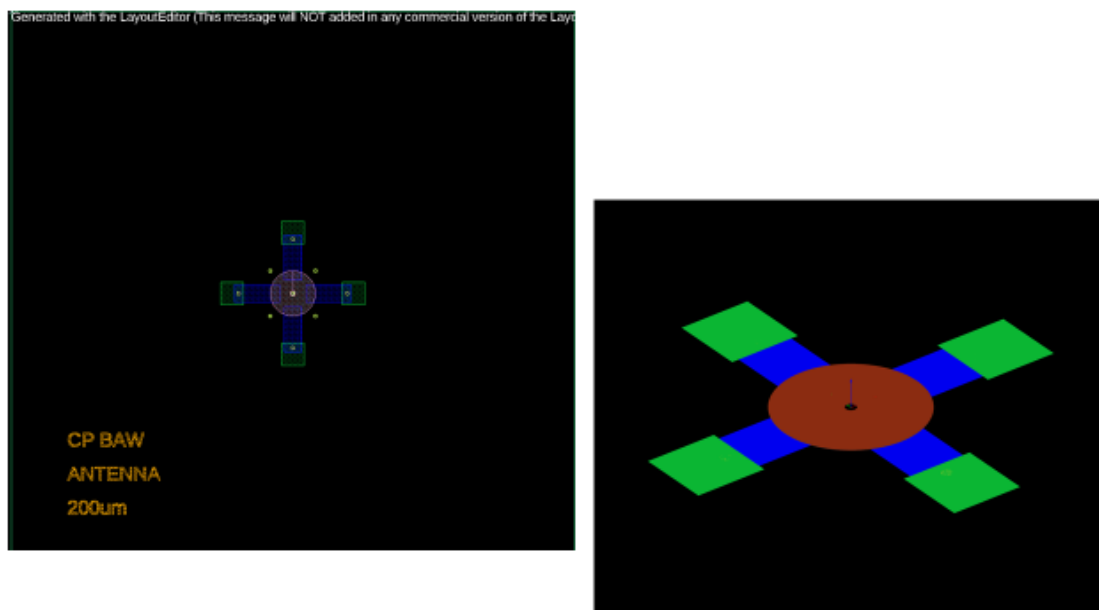


Fig. 4.2. Layout of 200  $\mu\text{m}$  CP BAW antenna. The green pads represent electrodes. The blue lines represent electric trace to provide shear excitation. The red disk represents the fabricated BAW antenna.



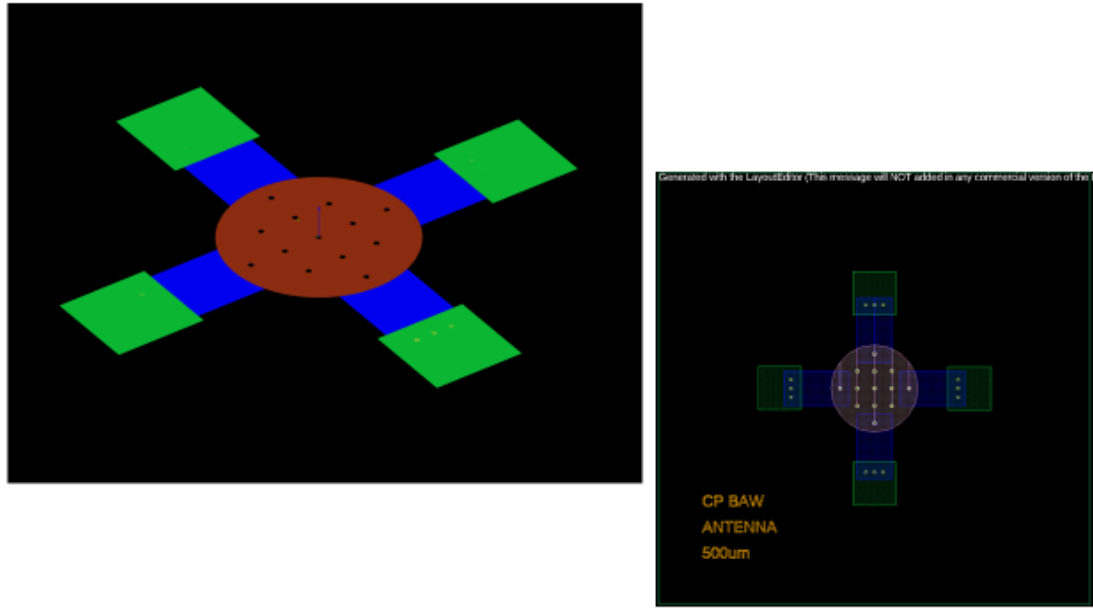


Fig. 4.3. Layout of 500  $\mu\text{m}$  CP BAW antenna. The green pads represent electrodes. The blue lines represent electric trace to provide shear excitation. The red disk represents the fabricated BAW antenna.

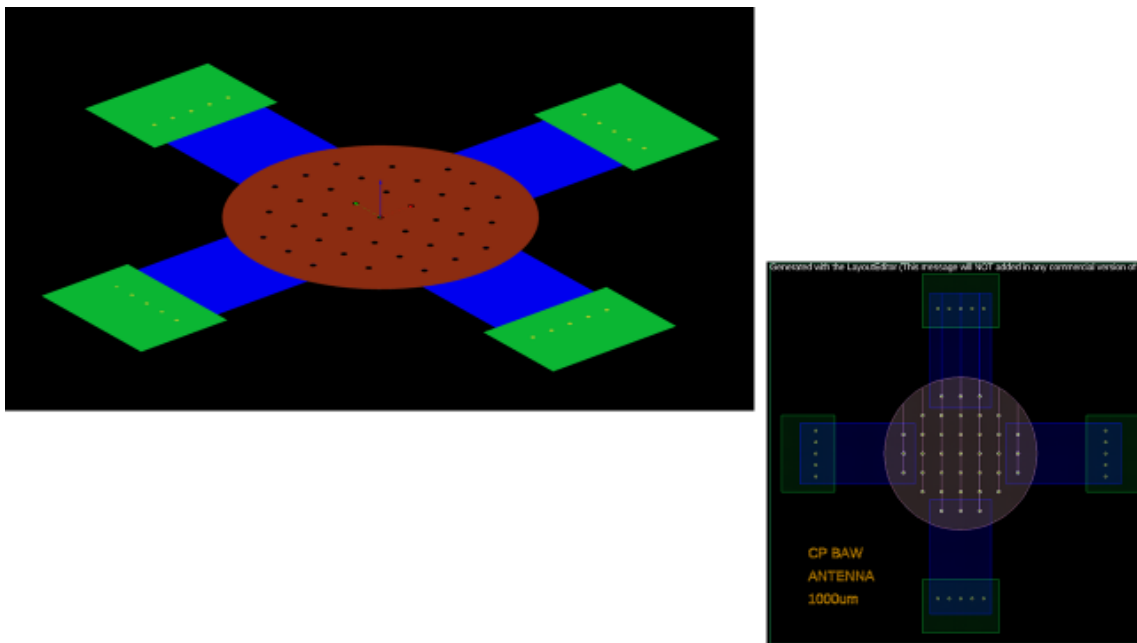


Fig. 4.4. Layout of 1000  $\mu\text{m}$  CP BAW antenna. The green pads represent electrodes. The blue lines represent electric trace to provide shear excitation. The red disk represents the fabricated BAW antenna.

ratio. Hence, the operation band is around 1.6GHz to 2.7GHz for  $\pm 1\text{dB}$  amplitude

imbalance and  $3^\circ$  phase imbalance. The design is illustrated in Fig. 4.5 and the photo is shown in Fig. 4.6. Metal Via holes are placed at both sides of CPW in order to preserve correct mode. Combining slot branch-line coupler combined with high permittivity substrate Rogers 6010/LM and radial slot stub for CPW-Slot conversion can achieve wideband response. CPW output is for the purpose of feeding the CP BAW antenna. Simulated and measured performance of 4 ports CPW-Slot-CPW with SMA connectors are shown in Fig. 4.7. The simulation agrees well with measurement result. Due to the needs of feeding BAW antenna and connecting with later electrodes with port 2 and 3, bond wires are further used to connect the CPW output signal line with the electrode pad which will be short to BAW antenna. The photos of the finished on are shown in Fig. 4.6. It should be noted that the linewidth of feeding trace is kept that same as the pad on BAW antenna. The connection is illustrated in Fig. 4.8 and the finished one is shown in Fig. 4.9. The photos of fabricated BAW antenna of 200/500/1000  $\mu\text{m}$  is taken from optical microscope, as shown in Fig. 4.10, Fig. 4.11 and Fig. 4.12.

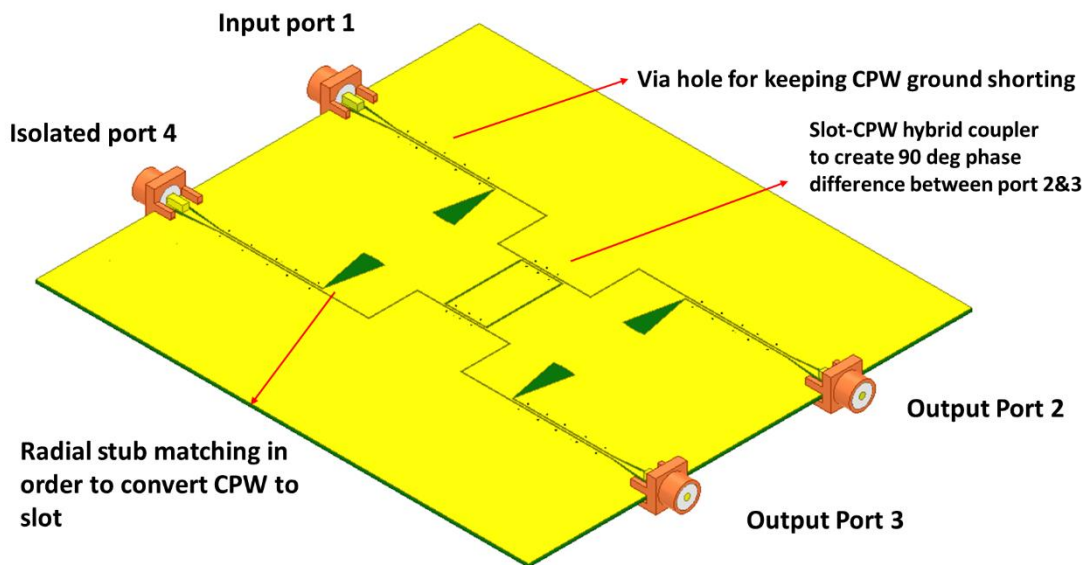


Fig. 4.5. Four ports CPW-Slot-CPW wideband branch-line coupler

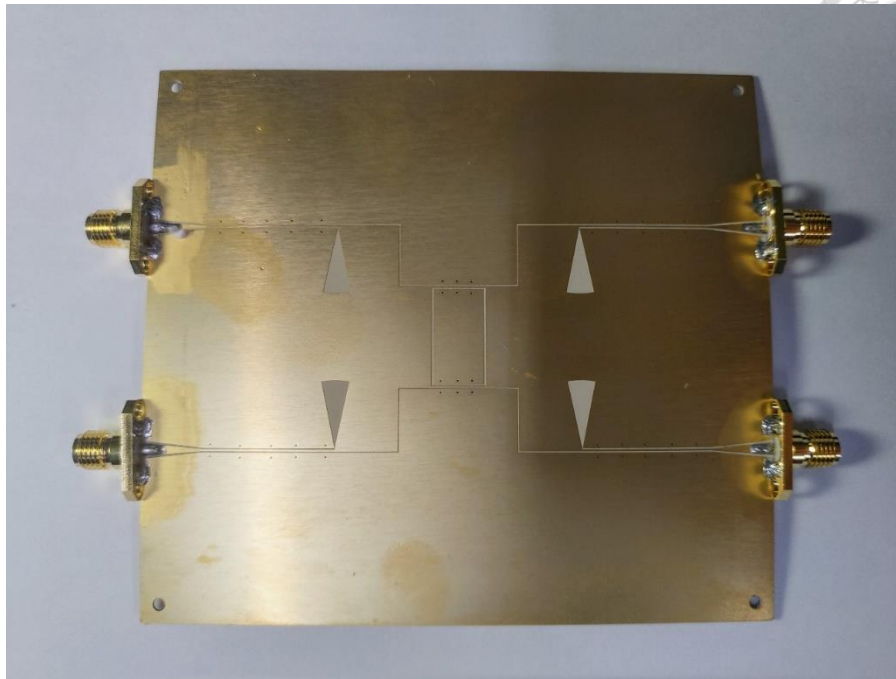


Fig. 4.7. Photo of the finished four ports wideband CPW-Slot-CPW branch-line coupler.

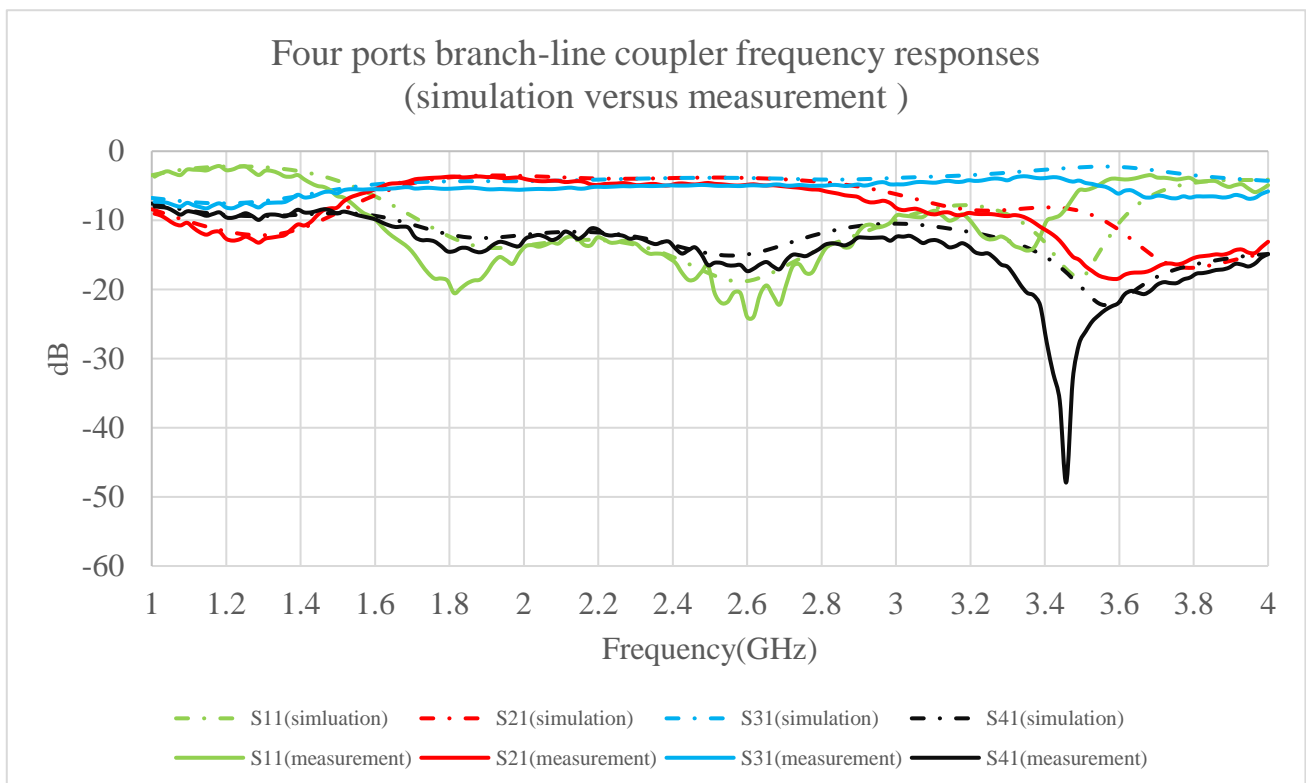


Fig. 4.6. Simulated S parameters of four ports CPW-Slot-CPW wideband branch-line coupler connected with SMA connectors.

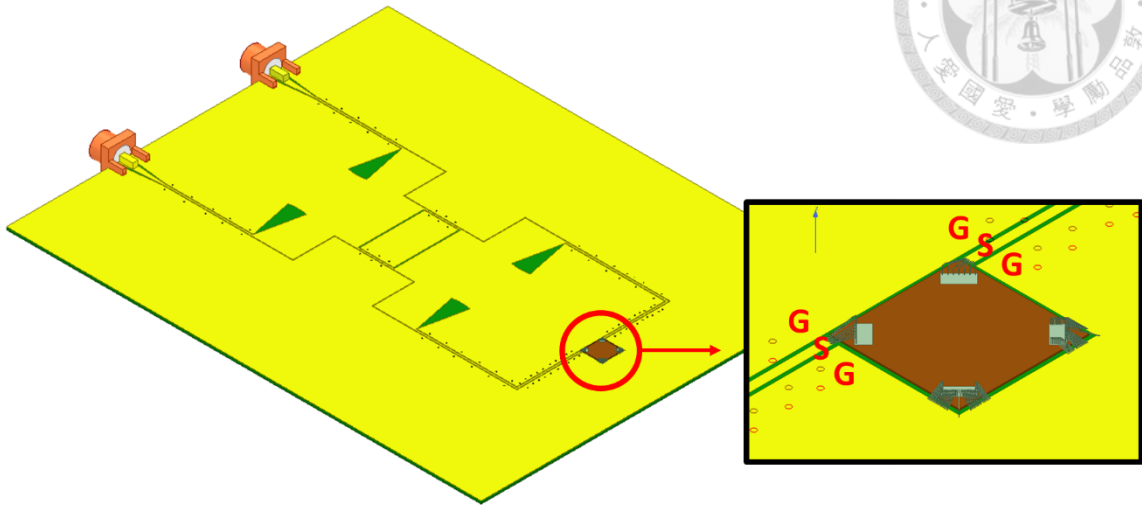


Fig. 4.9. Feeding BAW antenna and connecting with later electrodes with port 2 and 3

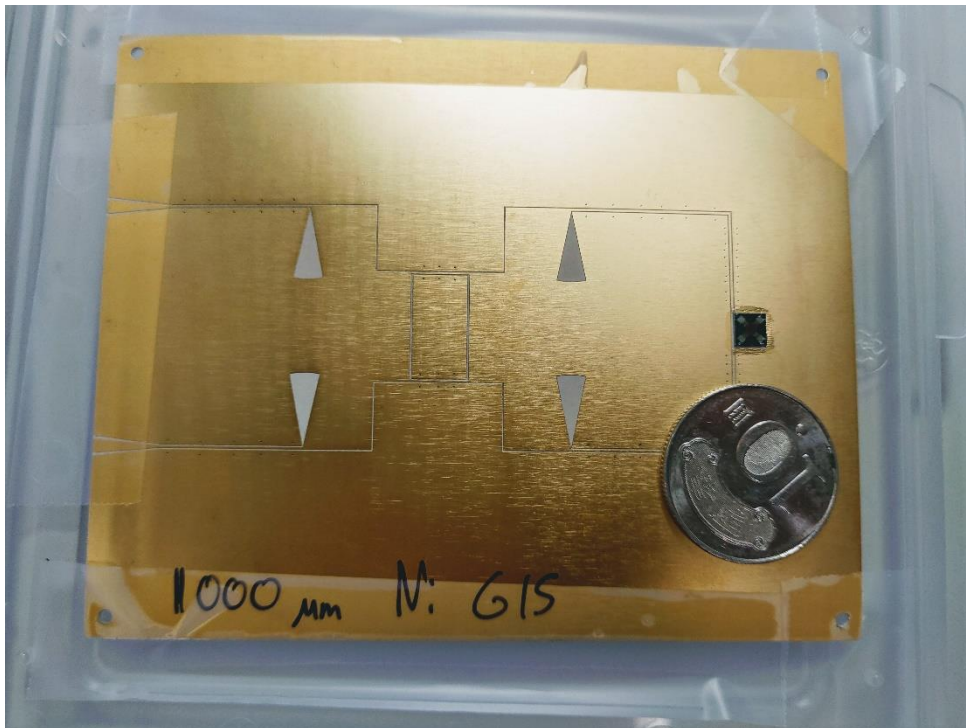


Fig. 4.8. Finished CP BAW antenna soldered onto branch-line coupler.

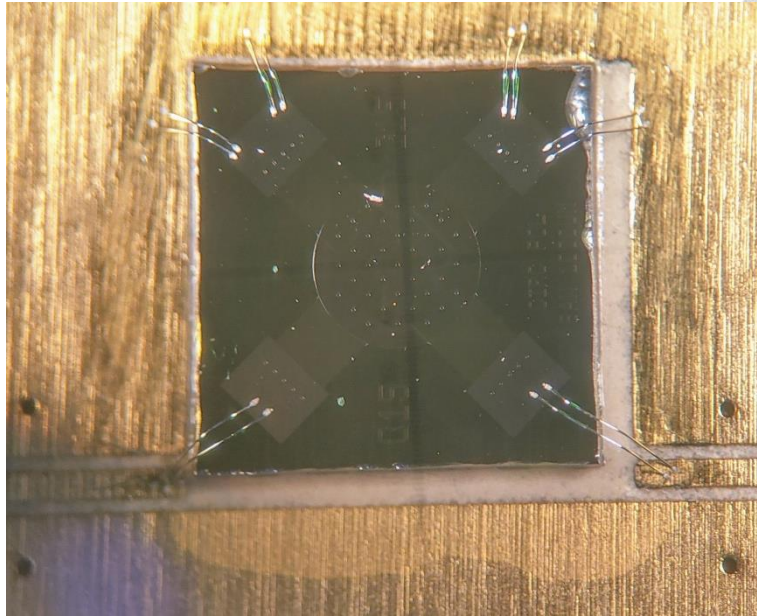


Fig. 4.11. Photo of the fabricated BAW antenna of  $1000\mu\text{m}$  one under optical microscope. The bond wires are used to connect with CPW signal and ground. The device is in the center of the chip.

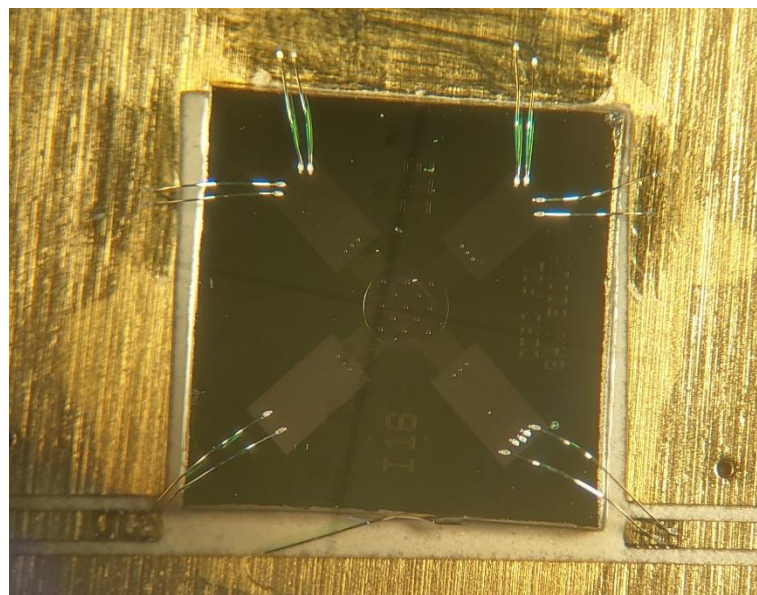


Fig. 4.10. Photo of the fabricated BAW antenna of  $500\mu\text{m}$ .

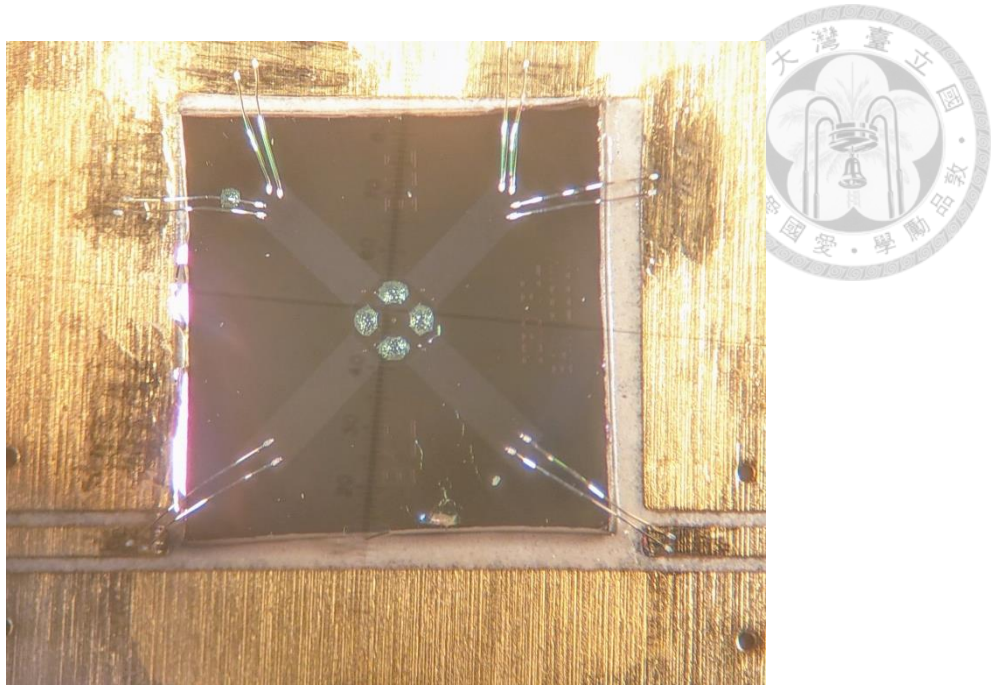


Fig. 4.12. Photo of the fabricated BAW antenna of 200 $\mu$ m.

## 4.2 Setup and measurements

The block diagram of experiment setup is shown in Fig. 4.13 and the photo is shown in Fig. 4.14. Agilent 2 port network analyzer N5232A analyzer at the right position is connected to horn antenna DRH-0118, which can operate from 1GHz to 18GHz. The magnitude of S21 can be seen as the relative basis to compare. The adjustable permanent magnet is meant to provide necessary out-of-plane magnetic field to saturate the device. One tesla is measured near the surface of the chip using a DC magnetic meter MG-3003SD as shown in Fig. 4.15. The measurement is essentially done through a series of comparisons. First, a patch antenna resonating at near 1.85GHz is designed and fabricated to test the setup. Also, the two orthogonal radiating components are used as comparison reference. The gain of this patch antenna is around 4dBi. The photo of the fabricated patch antenna and its measured S parameters is shown in Fig. 4.16 and Fig. 4.17. The antenna is well matched at 1.85GHz. Since the square patch antenna is mainly linearly polarized, the co-pol and cross-pol of radiated element can be seen as the reference magnitude. Co-pol and cross-pol are measured by rotating the coupler with keeping the same position of BAW antenna at the center of adjustable magnet. Co-pol represents 4dBi radiation and cross-pol represents environmental noise floor. In addition to the patch antenna, the coupler soldered to SMD Yageo 0201 1/20W 49.9 Ohm resistors (see Fig. 4.18) and radiation from four ports coupler (see Fig. 4.19) is also measured.



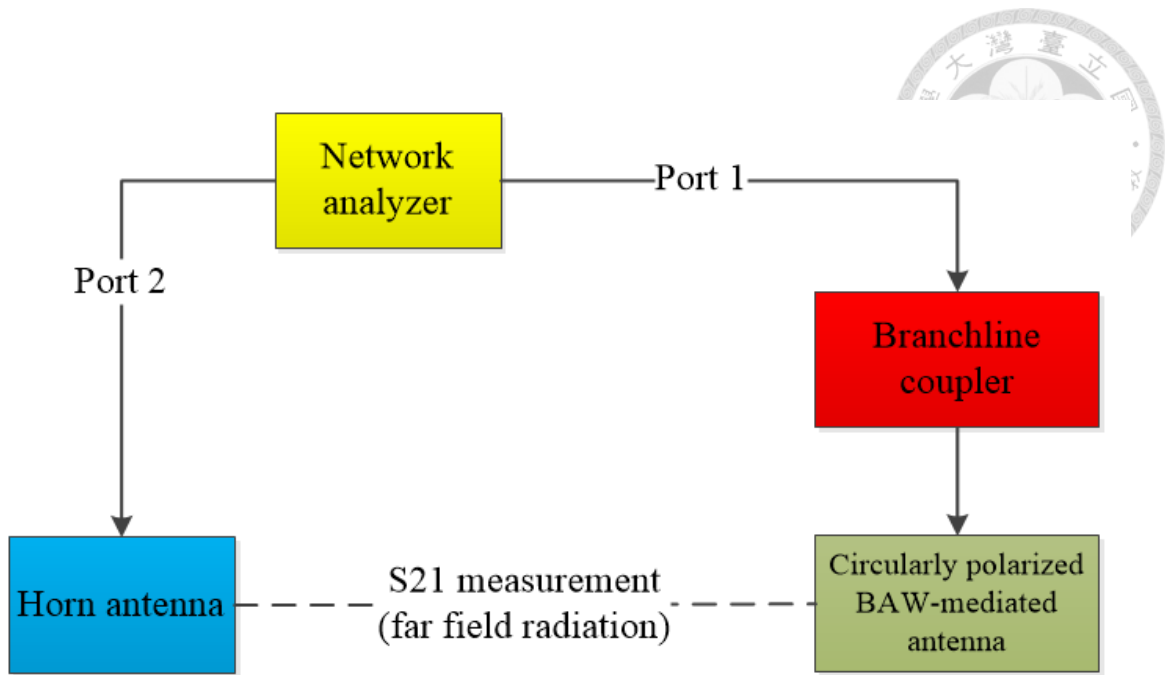


Fig. 4.13. Block diagram of measurement setup

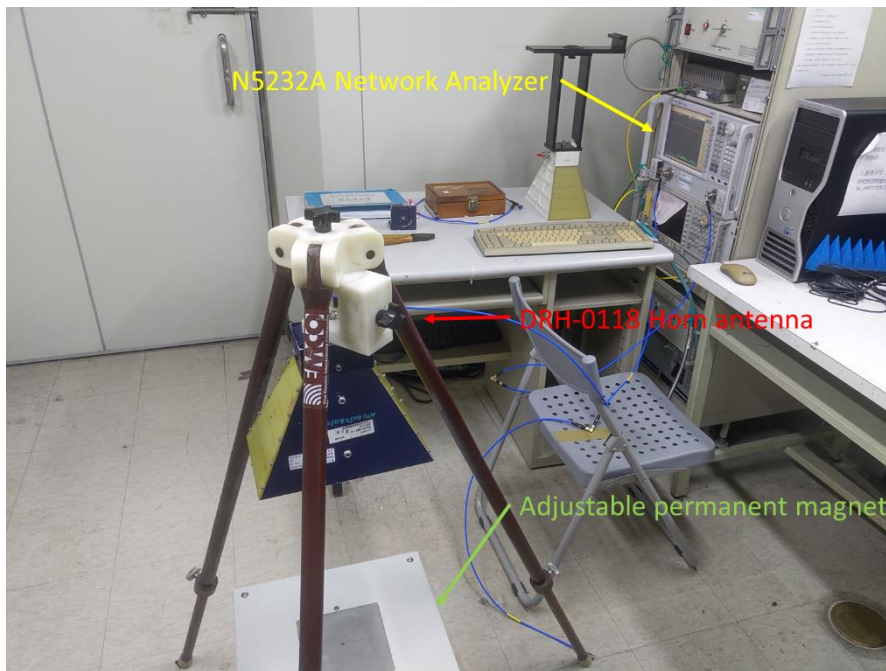


Fig. 4.14. Measurement setup. Network analyzer at the right position is connected to horn antenna. A tunable permanent magnet is placed at the bottom to provide external biased magnetic field to saturate the device.





Fig. 4.15. The adjustable permanent magnet is meant to provide necessary out-of-plane magnetic field to saturate the device. One tesla is measured near the surface of the chip using a DC magnetic meter MG-3003SD.

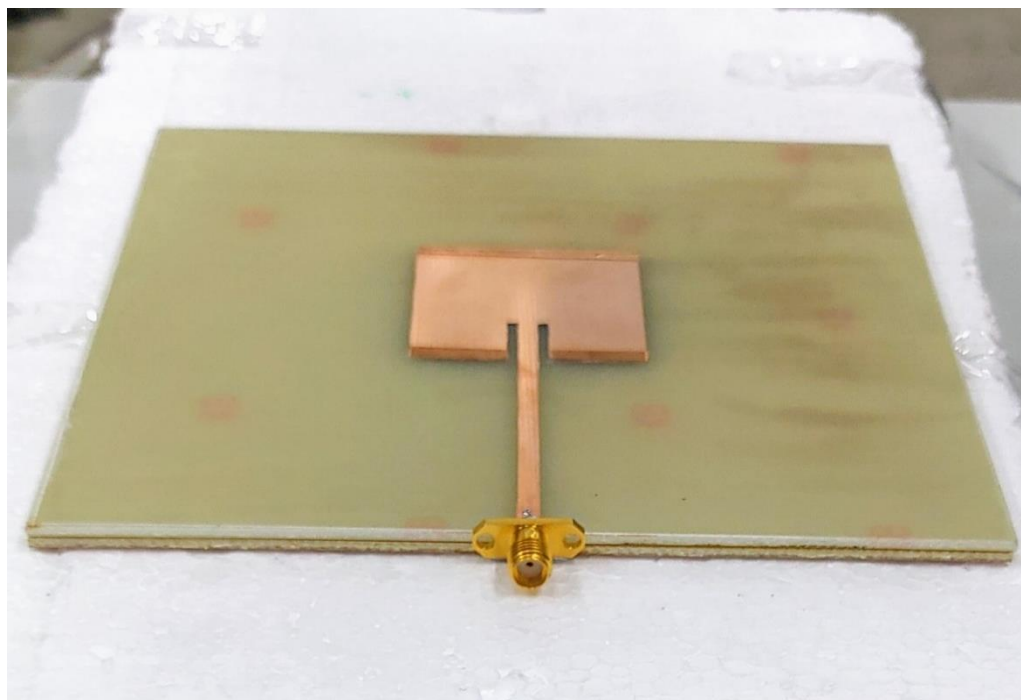


Fig. 4.16. The photo of fabricated patch antenna.

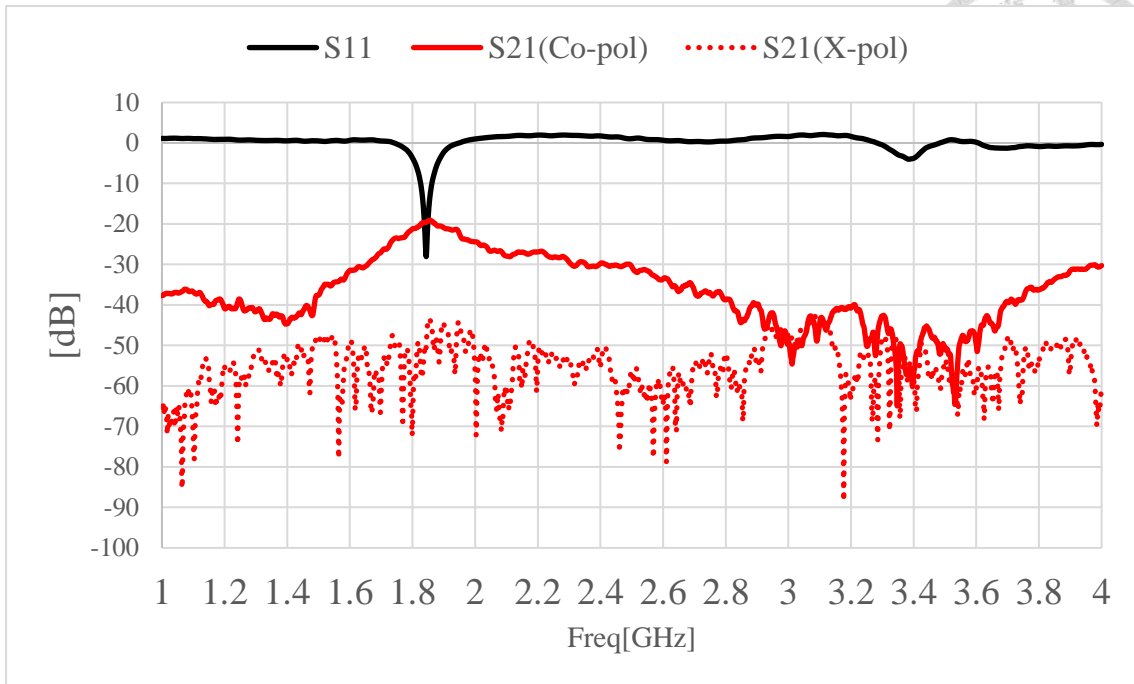


Fig. 4.17. The measured S parameters of patch antenna.

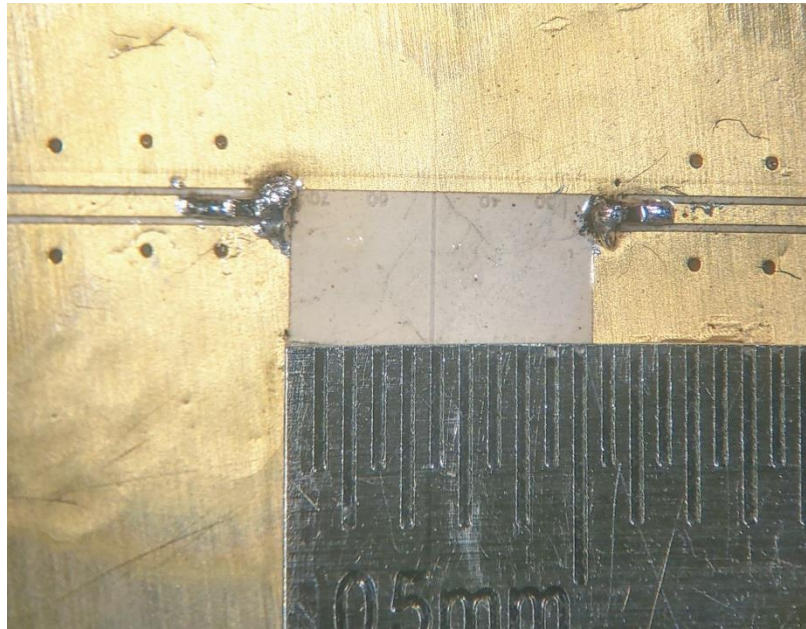


Fig. 4.18. Microscope view of the output CPW terminated with SMD resistor 0201.

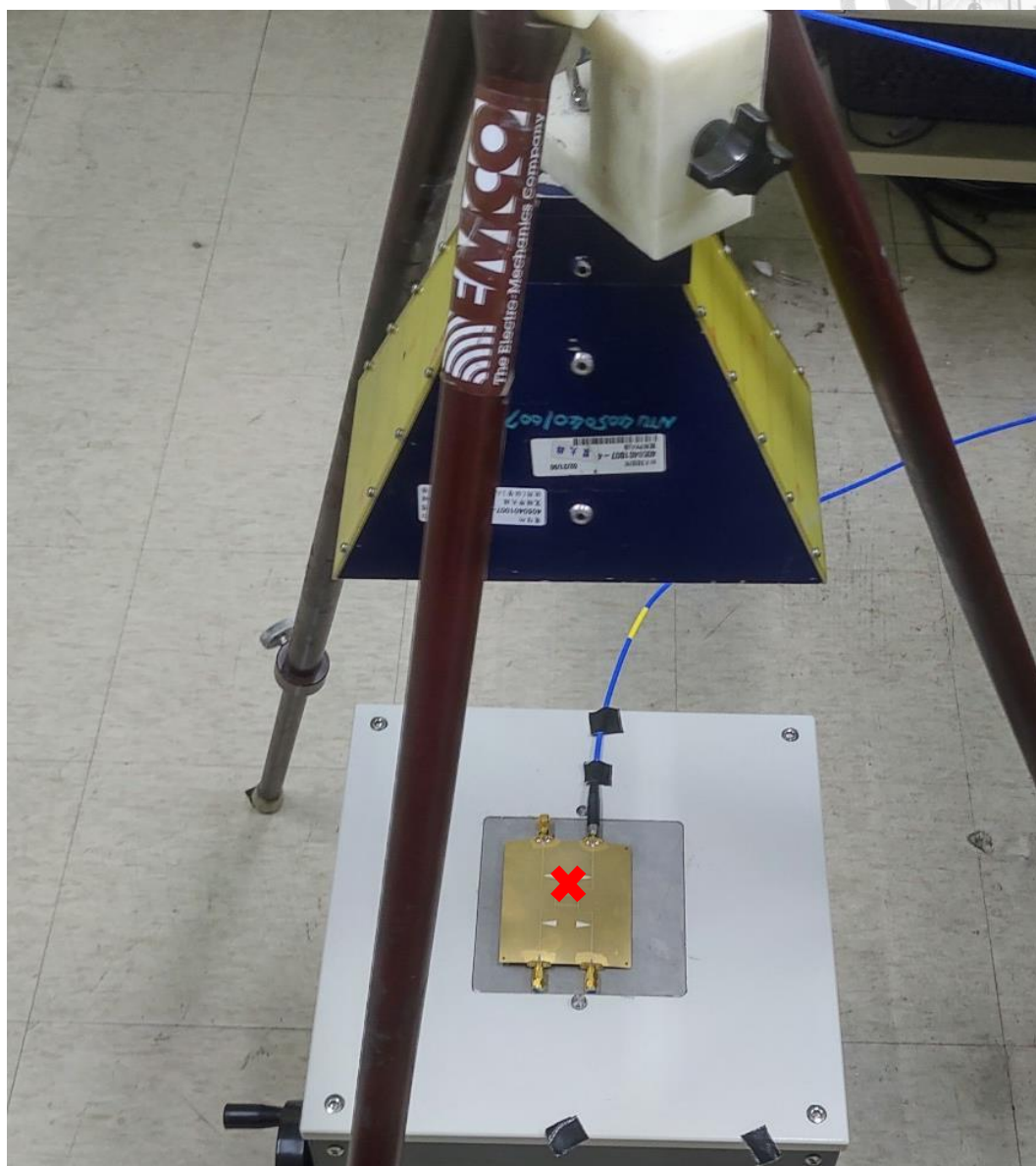


Fig. 4.19. Measuring radiation from four ports coupler itself. The coupler is placed at the same direction with the col-pol of patch antenna. By rotating the coupler by 90 degrees relative to the center of the magnet (red cross in the figure), the orthogonal component which is the same as cross-pol of patch antenna can be measured.

### 4.3 Results and Discussions



In Fig. 4.21, we can observed that there are unwanted radiation from the coupler itself near 1.15GHz and 1.7GHz. At 1.15GHz, radiation from both cross-pol of four ports coupler and coupler with load can be observed, while the four ports one is stronger. There is only radiation from coupler with load of cross-pol at 1.7GHz can be observed.

Three different versions of radius of BAW antenna with Ni and NiFe are fabricated. There shall be no radiation from magnetostrictive effect for NiFe in theory. Hence, NiFe is used as comparison reference to Ni. Six cases with 200/500/1000  $\mu\text{m}$  and corresponding Ni/NiFe are measured. Integrating the results from the coupler as well as NiFe, the radiation is examined in Fig. 4.20, Fig. 4.23 and Fig. 4.22. Bottom one is added with limit line to show the effective zone with the 90 degrees phase differences provided by coupler. If there's radiation generated, the S21 of Ni case(blue line) should be greater than NiFe case(black line) and not overlapped with 50ohm test board. However, near the effective zone shown by limit line, we can find that the only one which the radiation of Ni case is bigger than NiFe case is at 1.7GHz. This radiation will be very likely coming from the coupler itself when compared with coupler of four ports case compared. It's very likely that no radiation is successfully detected.

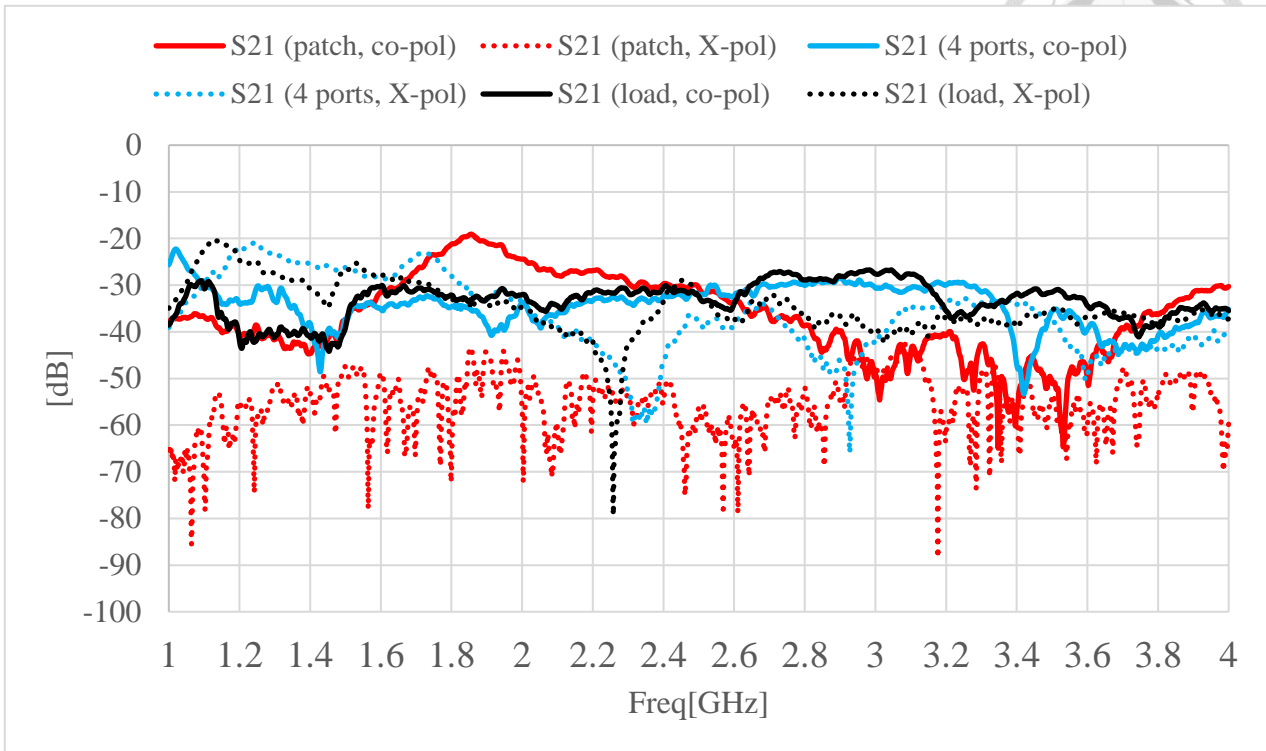


Fig. 4.21. The measured S parameters of patch antenna/branch-line coupler/coupler connected with load.

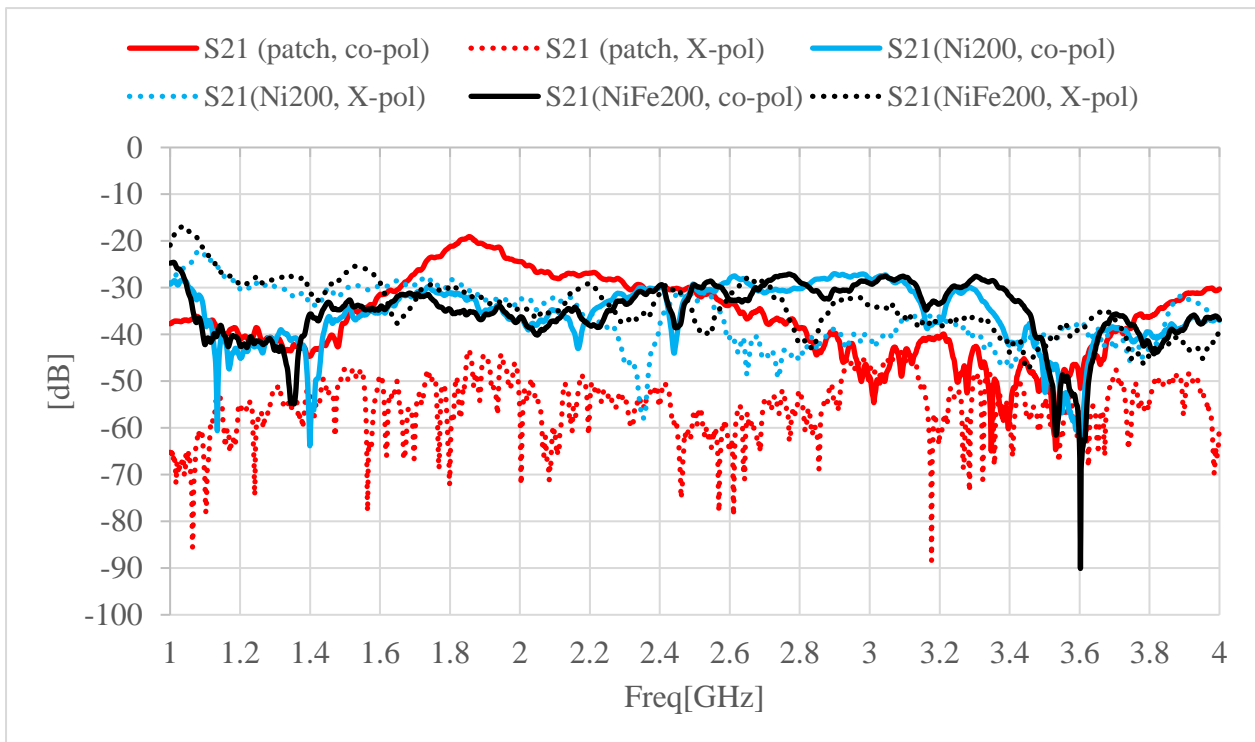


Fig. 4.20. The measured S parameters of CP BAW antenna of Ni/NiFe with radius of 200µm.

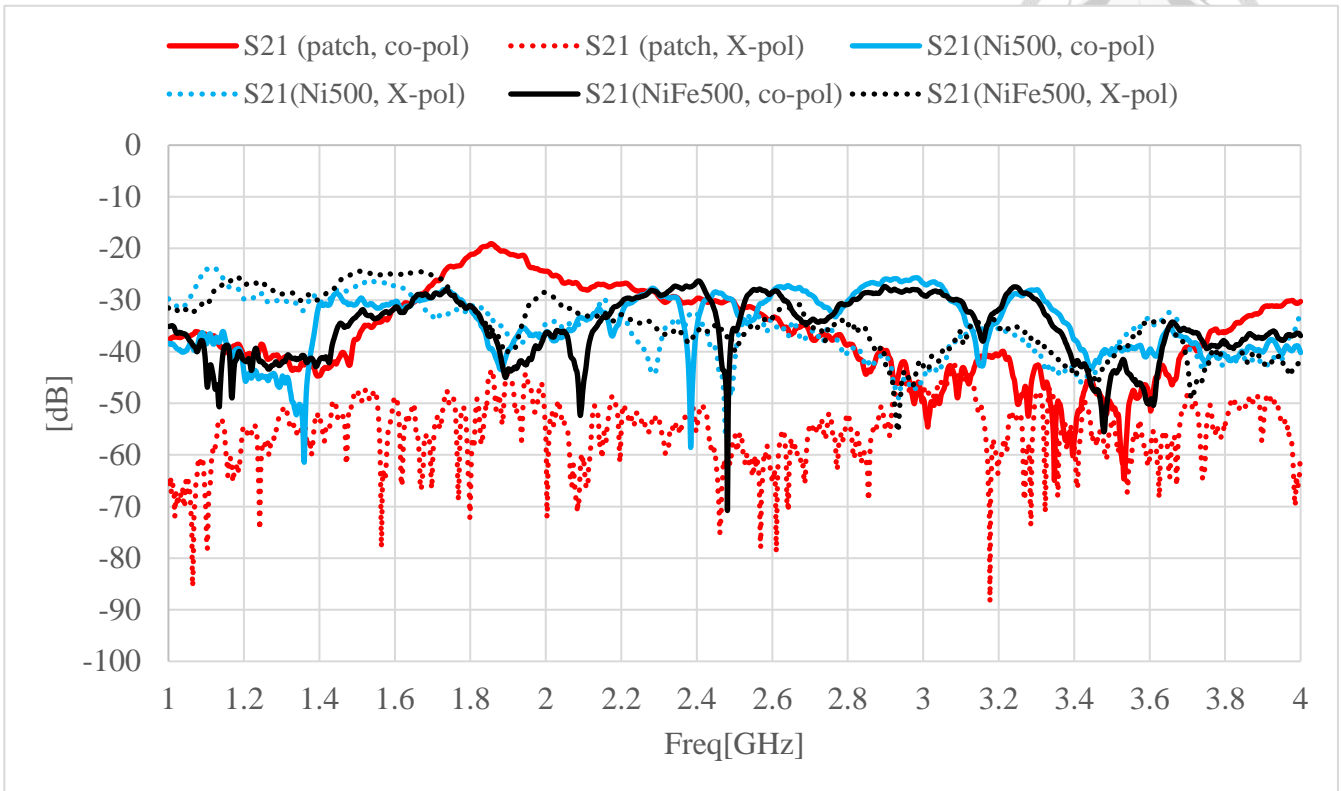


Fig. 4.23. The measured S parameters of CP BAW antenna of Ni/NiFe with radius of 500 $\mu$ m.

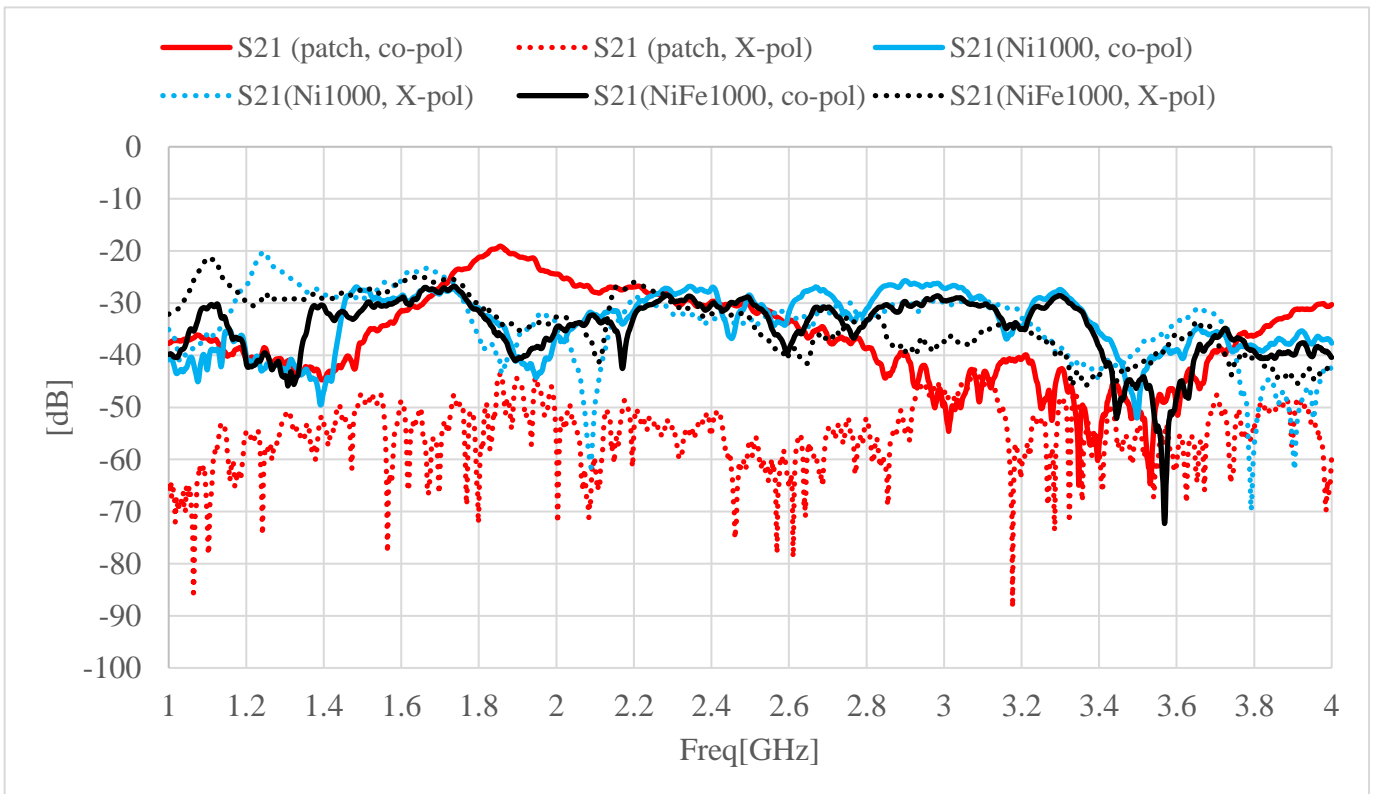


Fig. 4.22. The measured S parameters of CP BAW antenna of Ni/NiFe with radius of 1000 $\mu$ m.

## Chapter 5 Conclusions

### 5.1 Summary

BAW-mediated multiferroic antennas provide a viable pathway for antenna miniaturization. CP radiation of BAW mediated multiferroic antenna is proposed and investigated in this work. By combining COMSOL simulation with a series of post-processing under the assumption of weak coupling and linear magnetization, the radiation pattern and axial ratio of the proposed antenna can be obtained. It is shown that under the ideal input RF signal pair of equal magnitude and with  $90^\circ$  phase difference, the proposed design can achieve broadband CP with satisfactorily low axial ratio. The design concept is proved through FEM software by COMSOL and post processed by MATLAB. It is shown that under the ideal input RF signal pair of equal magnitude and with  $90^\circ$  phase difference, the proposed design can achieve broadband CP with satisfactorily low axial ratio. The design is fabricated by Sidhant Tiwari from Sensors and Technology Laboratory of University of California, Los Angeles. The design is also measured and results are discussed through a couple of comparisons. However, no clear radiation is detected.





## 5.2 Future Works

First, further work will definitely be eliminating unwanted radiation source. If we want to study the polarization concept, the better way is to study only one set of thickness shear wave. Hence, instead of using branch-line coupler, we should firstly feed the antenna directly by connecting the electrodes. Second, if we can know what exactly is the resonant frequency of the device, the magnetostrictive properties need to be combined together in the simulation. But it's often time-consuming to do the full coupling simulation, sometimes 2 to 3 days for simple cases only for decoupled simulation. Hence, if we want to develop and optimize such device, there's a lot of room for improvement of simulation. Also, the meshing mechanism require improvement for the balance between time and accuracy. What is the best trade-off strategies for the meshing?

Last but not the least, the study on material of magnetostrictive properties requires further clarification. How good is the radiation characteristics of Ni? Is it the most suitable material for GHz band application? What's the frequency response of Ni? Is it suitable for high or low frequency band? Why is the team from Northeastern University use GaFeB instead of Ni? What is the radiation efficiency calculation by using piezoelectric and magnetostrictive material? Since the efficiency is the most important question of electrically small antenna, this problem needs to be defined and studies clearly in the future.

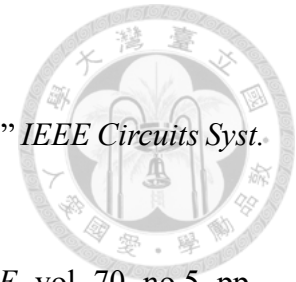


## References




- [1] J. Iannacci, *RF-MEMS Technology for High-Performance Passives*. Bristol, UK: IOP Publishing, 2017, ch.3, p.5.
- [2] J. Iannacci, *RF-MEMS Technology for High-Performance Passives*. Bristol, UK: IOP Publishing, 2017, ch.3, pp.7–9.
- [3] J. Iannacci, *RF-MEMS Technology for High-Performance Passives*. Bristol, UK: IOP Publishing, 2017, ch.2, p.17.
- [4] J. Iannacci, *RF-MEMS Technology for High-Performance Passives*. Bristol, UK: IOP Publishing, 2017, ch.3, pp.10–15.
- [5] J. Iannacci, *RF-MEMS Technology for High-Performance Passives*. Bristol, UK: IOP Publishing, 2017, ch.3, p.17.
- [6] J. Iannacci, *RF-MEMS Technology for High-Performance Passives*. Bristol, UK: IOP Publishing, 2017, ch.3, p.10.
- [7] J. Iannacci, *RF-MEMS Technology for High-Performance Passives*. Bristol, UK: IOP Publishing, 2017, ch.3, p.11.
- [8] J. Iannacci, *RF-MEMS Technology for High-Performance Passives*. Bristol, UK: IOP Publishing, 2017, ch.2, p.18.
- [9] J. Iannacci, *RF-MEMS Technology for High-Performance Passives*. Bristol, UK: IOP Publishing, 2017, ch.4, p.3.
- [10] J. Iannacci, *RF-MEMS Technology for High-Performance Passives*. Bristol, UK: IOP Publishing, 2017, ch.3, p.19.
- [11] Moore, Gordon E, “Cramming more components onto integrated circuits,” *IEEE Solid-State Circuits Society Newsletter*, vol. 11, no. 3, pp. 33-35, Sept., 2006.
- [12] Mack, Chris A, “Fifty years of Moore's law,” *IEEE Trans. Semicond. Manuf.*, vol.24,


- no. 2, pp. 202-207, May, 2011.
- [13] W.-M. Dai, "Historical Perspective of System in Package (SiP)," *IEEE Circuits Syst. Mag.*, vol. 16, no. 2, pp. 50-61, May, 2016.
- [14] K. E. Petersen, "Silicon as a mechanical material," *Proc. IEEE*, vol. 70, no.5, pp. 420-457, May, 1982.
- [15] R. Bogue, "MEMS sensors: past, present and future," *Sensor Rev.*, vol. 27, no. 1, pp.7-13, 2007.
- [16] H. A. C. Tilmans, W. D. Raedt, and E. Beyne, "MEMS for wireless communications: 'from RF-MEMS components to RF-MEMS-SiP'," *J. Micromech. Microeng.*, vol. 13, pp.S139-S163, Jun, 2003.
- [17] J. Iannacci, *RF-MEMS Technology for High-Performance Passives*. Bristol, UK: IOP Publishing, 2017, ch.1, pp.9–11.
- [18] J. Iannacci, *RF-MEMS Technology for High-Performance Passives*. Bristol, UK: IOP Publishing, 2017, ch.4, p.2.
- [19] J. Iannacci, *RF-MEMS Technology for High-Performance Passives*. Bristol, UK: IOP Publishing, 2017, ch.2.
- [20] J. Iannacci, *RF-MEMS Technology for High-Performance Passives*. Bristol, UK: IOP Publishing, 2017, ch.2, p.2.
- [21] J. Iannacci, *RF-MEMS Technology for High-Performance Passives*. Bristol, UK: IOP Publishing, 2017, ch.2, p.7.
- [22] L. J. Chu, "Physical Limitations of Omnidirectional Antennas," *J. Appl. Phys.*, vol. 19, pp. 1163–1175, Dec., 1948.
- [23] R. F. Harrington, "Effect of Antenna Size on Gain, Bandwidth, and Efficiency," *J. Res. Nat. Bur. Stand.-D, Radio Propagat.*, vol. 64D, pp. 1–12, Jan., 1960.
- [24] H. A. Wheeler, "Fundamental Limitations of Small Antennas," *Proc. IRE*, pp.



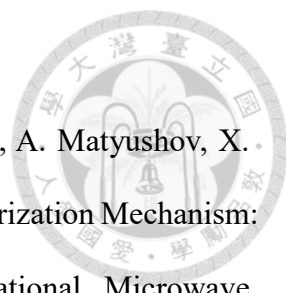
1479–1488, Dec., 1947.

- 
- [25] C. A. Balanis, *Antenna Theory: Analysis and Design*. New Jersey, USA: John Wiley & Sons, 2005.
- [26] D. F. Sievenpiper, D. C. Dawson, M. M. Jacob, T. Kanar, S. Kim, J. Long, and R. G. Quarfoth, “Experimental Validation of Performance Limits and Design Guidelines for Small Antennas,” *IEEE Trans. Antennas Propag.*, vol. 60, no. 1, pp. 8-19, Jan., 2012.
- [27] R. C. Hansen, “Fundamental Limitations in Antennas,” *Proc. IEEE*, vol. 69, no. 2, Feb., 1981.
- [28] J. S. McLean, “A Re-examination of the Fundamental Limits on the Radiation Q of Electrically Small Antennas,” *IEEE Trans. Antennas Propag.*, vol. 44, no. 5, pp. 672-676, May., 1996.
- [29] R. Collin and S. Rothschild, “Evaluation of antenna Q,” *IEEE Trans. Antennas Propag.*, vol. 12, pp. 23-27, 1964.
- [30] R. L. Fante, “Maximum possible gain for an arbitrary ideal antenna with specified quality factor,” *IEEE Trans. Antennas Propag.*, vol. 40, pp. 1586-1588, 1992.
- [31] A. D. Yaghjian and S. R. Best, “Impedance, bandwidth, and Q of antennas,” *IEEE Trans. Antennas Propag.*, vol. 53, pp. 1298-1324, 2005.
- [32] C. Friedman, “Wide-band matching of a small disk-loaded monopole,” *IEEE Trans. Antennas Propag.*, vol. 33, pp. 1142-1148, 1985.
- [33] J. A. Bickford, A. E. Duwel, M. S. Weinberg, R. S. McNabb, D. K. Freeman, and P. A. Ward, “Performance of Electrically Small Conventional and Mechanical Antennas,” *IEEE Trans. Antennas Propag.*, vol. 67, no. 4, pp. 2209-2223, Jan., 2019.
- [34] M. Nagaraja and S. Prasad, “Going Beyond Chu's Limit: ULF Radiation with Directly Modulated Spinning Magnet Arrays,” M.S. thesis, Dept. Elect. Eng., Univ.

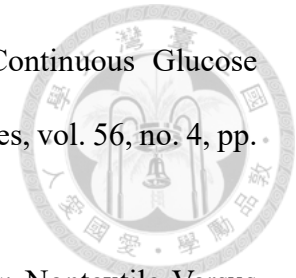
of California, Los Angeles, CA, USA, 2017.

- 
- [35] Z. Yao, Y. E. Wang, S. Keller and G. P. Carman, "Bulk Acoustic Wave-Mediated Multiferroic Antennas: Architecture and Performance Bound," *IEEE Trans. Antennas Propag.*, vol. 63, no. 8, pp. 3335-3344, Aug., 2015.
- [36] T. Nan, H. Lin, Y. Gao, A. Matyushov, G. Yu, H. Chen, N. Sun, S. Wei, Z. Wang, M. Li, X. Wang, A. Belkessam, R. Guo, B. Chen, J. Zhou, Z. Qian, Y. Hui, M. Rinaldi, M. E. Mcconney, B. M. Howe, Z. Hu, J. G. Jones, G. J. Brown, and N. X. Sun, "Acoustically Actuated Ultra-Compact NEMS Magnetoelectric Antennas," *Nature Comm.*, vol. 8, no. 296, 2017.
- [37] Z. Yao, and Y. E. Wang, "Bulk acoustic wave mediated multiferroic antennas near ferromagnetic resonance," In *Proc. IEEE International Symposium on Antennas and Propagation & USNC/URSI National Radio Science Meeting*, Jul., 2015.
- [38] Z. Yao, "Dynamic Analysis of Thin Film Multiferroic Radiation via FDTD Methods," M.S. thesis, Dept. Elect. Eng., Univ. of California, Los Angeles, CA, USA, 2014.
- [39] Z. Yao, "A Multiscale, Unconditionally Stable Multiphysics Time-Domain (MUST) Solver Unifying Electrodynamics, Elastodynamics and Spin Dynamics," Ph.D. dissertation, Dept. Elect. Eng., Univ. of California, Los Angeles, CA, USA, 2017.
- [40] Z. Yao, and Y. E. Wang, "3D modeling of BAW-based multiferroic antennas," *IEEE International Symposium on Antennas and Propagation & USNC/URSI National Radio Science Meeting*, 2017.
- [41] R.-F. Xu, S. Tiwari, R. N. Candler, S.-Y. Chen, "Polarization Control of Bulk Acoustic Wave-Mediated Multiferroic Antennas Based on Thickness Shear Modes," In *Proc. European Conference on Antennas and Propagation(EuCAP)*, Apr., 2018.
- [42] J.P. Domann, and G.P. Carman, "Strain powered antennas," *J. of Appl. Phys.*, vol.

121, no.4, 2017.

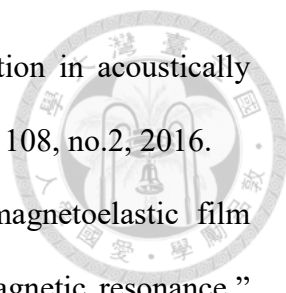
- 
- [43] H. Lin, M. Zaeimbashi, N. Sun, X. Liang, H. Chen, C. Dong, A. Matyushov, X. Wang, Y. Guo, Y. Gao, and N.-X. Sun, "Future Antenna Miniaturization Mechanism: Magnetolectric Antennas," In Proc. IEEE/MTT-S International Microwave Symposium, pp. 10-15, 2018.
- [44] J. Xiaolin, et al. "RFID technology and its applications in Internet of Things (IoT)." In Proc. IEEE International Conference on Consumer Electronics, Communications and Networks (CECNet), 2012.
- [45] K. Finkenzeller, RFID Handbook: Fundamentals and Applications in Contactless Smart Cards, Radio Frequency Identification and Near-Field Communication, New York: Wiley, 2010.
- [46] L. Jeremy, "The history of RFID," *IEEE potentials*, vol. 24, no.4, pp.8-11, 2015.
- [47] A. K. Skrivervik, "Implantable antennas: The challenge of efficiency," In Proc. European Conference on Antennas and Propagation (EuCAP), 2013.
- [48] R. S. Mackay, "Radio telemetering from within the body: inside information is revealed by tiny transmitters that can be swallowed or implanted in man or animal," *Science*, vol. 134, pp. 1196-1202, 1961.
- [49] A. Rosen, "Microwave application in cancer therapy, cardiology and measurement techniques: A short overview," *IEEE MTT Newsletter*, pp. 17-20, 1990.
- [50] A. W. Guy, J. F. Lehmann, and J. B. Stonebridge, "Therapeutic Applications of Electromagnetic Power," *Proceedings of the IEEE*, vol. 62, no. 1, pp. 52-75, 1974.
- [51] M. F. Furse, C. M. Iskander, "Three-Dimensional Electromagnetic Power Deposition in Tumors Using Interstitial Antenna Arrays," *IEEE Trans. on Biomedical Engineering*, vol. 36, no. 10, pp. 977-986, Oct., 1989.
- [52] T. Karacolak, A. Z. Hood, and E. Topsakal, "Design of a Dual-Band Implantable

Antenna and Development of Skin Mimicking Gels for Continuous Glucose Monitoring,” IEEE Trans. on Microwave Theory and Techniques, vol. 56, no. 4, pp. 1001-1008, 2008.



- [53] L. Corchia, G. Monti, and L. Tarricone, “Wearable Antennas: Nontextile Versus Fully Textile Solutions,” IEEE Antennas and Propag. Mag., vol. 61, no. 2 pp.71-83, 2019.
- [54] D. Ferreira, P. Pires, R. Rodrigues, and R. F. S. Caldeirinha, “Wearable textile antennas: Examining the effect of bending on their performance,” IEEE Antennas Propag. Mag., vol. 59, no. 3, pp. 54–59, 2017.
- [55] H. Khaleel, *Innovation in Wearable and Flexible Antennas*. Southampton, U.K.: WIT Press, 2015.
- [56] D. Roddy and J. Coolen, *Electronic Communications (4th Ed.)*. Upper Saddle River, NJ, USA: Prentice-Hall, Inc., 1995.
- [57] A. D. Watt, *VLF Radio Engineering*. Pergamon Press, 1967.
- [58] Sappati K.K. and Bhadra S., “Piezoelectric Polymer and Paper Substrates: A Review.,” Sensors (Basel)., vol. 18, no. 11, 2018.
- [59] A. Safari, E. K. Akdogan, *Piezoelectric and Acoustic Materials for Transducer Applications*. Springer Science & Business Media: New York, NY, USA, 2008.
- [60] K. Uchino, *Introduction to Piezoelectric Actuators and Transducers*; Technical Report; Pennsylvania State University: University Park, PA, USA, 2003.
- [61] W. Heywang, K. Lubitz and W. Wersing, *Piezoelectricity: Evolution and Future of a Technology*. Springer: Berlin, Germany, 2008.
- [62] C. Ruppel, “Acoustic Wave Filter Technology - A Review,” IEEE Trans. on Ultrasonics, Ferroelectrics and Frequency Control, 2017.
- [63] R. Aigner, “Filter technologies for converged RF-frontend architectures: SAW,

- BAW and beyond,” in Proc. IEEE SiRF, pp. 136-139, Jun., 2010.
- [64] R. Aigner, “SAW and BAW Technologies for RF Filter applications: A Review of the Relative Strengths and Weaknesses,” Proc. of IEEE Ultrasonics Symposium, Beijing/China, pp. 2-5, Nov., 2008.
- [65] F. Z. Bi and B. P. Barber, “Bulk acoustic wave RF technology,” IEEE Microwave Magazine, vol. 9, no. 5, pp. 65-80, Oct., 2008.
- [66] H. Mosallaei and K. Sarabandi, “Magneto-dielectrics in electromagnetics: concept and applications,” IEEE Trans. on Antennas and Propag., vol. 52, pp. 1558-1567, 2004.
- [67] P. M. T. Ikonen, K. N. Rozanov, A. V. Osipov, P. Alitalo, and S. A. Tretyakov, “Magnetodielectric Substrates in Antenna Miniaturization: Potential and Limitations,” IEEE Trans. on Antennas and Propag., vol. 54, pp. 3391-3399, 2006.
- [68] R. C. Hansen and M. Burke, “Antennas with magneto-dielectrics,” Microwave and Optical Technology Letters, vol. 26, pp. 75-78, 2000.
- [69] D. M. Pozar, *Microwave Engineering*. New Jersey, USA: John Wiley & Sons, 2012.
- [70] H. Schmid, “Multi-ferroic magnetoelectrics,” Ferroelectrics, vol. 162, pp. 317-338, Jan., 1994.
- [71] L. Martin, S. Crane, Y. Chu, M. Holcomb, M. Gajek, M. Huijben, et al., “Multiferroics and magnetoelectrics: thin films and nanostructures,” J. of Phys.: Condensed Matter, vol. 20, Oct., 2008.
- [72] S. Tiwari, “Multiferroic Bulk Acoustic Wave (BAW) Transducers as Electrically-Small Antennas,” Ph.D. dissertation prospectus, Dept. Elect. Eng., Univ. of California, Los Angeles, CA, USA.
- [73] L. Dreher, et al. “Surface acoustic wave driven ferromagnetic resonance in nickel thin films: Theory and experiment.” Physical Review B, vol. 86, no.13, 2012.

- 
- [74] D. Labanowski, A. Jung, and S. Salahuddin, "Power absorption in acoustically driven ferromagnetic resonance," *Applied Physics Letters*, vol. 108, no.2, 2016.
- [75] D. Labanowski, A. Jung, and S. Salahuddin, "Effect of magnetoelastic film thickness on power absorption in acoustically driven ferromagnetic resonance," *Applied Physics Letters*, vol. 111, 2017.
- [76] A. Sergey, et al. "Tunable HBAR based on magnetoelectric YIG/ZnO structure." *IEEE International Ultrasonics Symposium*, 2012.
- [77] B.-Y. Toh, R. Cahill, V.F. Fusco, "Understanding and Measuring Circular Polarization," *IEEE Trans. Edu.*, vol. 46, no. 3, pp. 313-318, Aug., 2003.
- [78] D. Milyutin, S. Gentil, and P. Muralt, "Shear mode bulk acoustic wave resonators based on c-axis oriented AlN thin film," *J. Appl. Phys.*, vol. 104, Oct., 2008.
- [79] D. Chen, J. Wang, D. Li, L. Zhang and X. Wang, "The c-axis oriented AlN solidly mounted resonator operated in thickness shear mode using lateral electric field excitation," *Appl. Phys. A*, vol. 100, pp. 239-244, Mar., 2010.
- [80] M. Ghidini, R. Mansell, F. Maccherozzi, X. Moya, L. C. Phillips, W. Yan, D. Pesquera, C. H. W. Barnes, R. P. Cowburn, J.-M. Hu, S. S. Dhesi and N. D. Mathur, "Shear-strain-mediated magnetoelectric effects revealed by imaging," *Nature Materials*, vol. 18, pp.840-845, May, 2019.
- [81] R. C. O'Handley, *Modern Magnetic Materials: Principles and Applications*. New York, USA: John Wiley & Sons, pp. 229-234, 2000.
- [82] C.-H. Ho, L. Fan, and K. Chang, "Broadband uniplanar hybrid-ring and branch-line couplers," *IEEE Trans. Microwave Theory Tech.*, vol. 41, no. 12, pp. 2116-2122, 1993.